Investigation of long-lived photo-induced processes in photorefractive crystals of the sillenite group and their application

Dissertation
zur Erlangung des akademischen Grades

doctor rerum naturalium (Dr. rer. nat.)

vorgelegt dem Rat der Physikalisch-Astronomischen Fakultät
der Friedrich-Schiller-Universität Jena

von Diplom-Physiker Andrew Matusevich

geboren am 24. Juli 1984 in Minsk (Weißrussland)

Gutachter:

1. **Prof. Dr. Richard Kowarschik**
2. **Prof. Dr. Hartmut Bartelt**
3. **Prof. Vasilij Shepelevich**

Tag der öffentlichen Verteidigung : 05. 04. 2011

Contents

Chapter 1

Introduction and Aims

1.1 Introduction

Photorefractive crystals are promising candidates for various applications with cw and pulse lasers as media for optical information processing, phase conjugation, interferometry and others. The interaction of pulse laser radiation with photorefractive crystals provides new possible applications for measurements of processes with short lifetimes and processing of materials. One of the most important questions for application is the corresponding response time. Sillenites can reach low response times if pulse laser systems are applied. The high peak intensity of pulse laser radiation generates strong long-lived photo-induced absorption, which influences on the whole system. In this case the spectral and dynamical behaviors of the induced absorption are of great importance. This work is devoted to the investigation of the photo-induced processes as reason of the long-lived induced absorption. On the base of the experimental results we try to understand the nature of the photo-induced effects and theoretically describe the long-lived influence of the light on the photorefractive crystals. We suggest that such effects with long life-times can find wide application in future.

The photorefractive effect has been observed in numerous materials:

- Oxygen-octahedra ferroelectrics: $LiNbO_3$, $LiTaO_3$ [1,2], $BaTiO_3$ [3], $KNbO_3$ [4], $K(TaNb)O_3$ [4, 5], $Ba_2NaNb_5O_{15}$ [6], $Ba_{1-x}Sr_xNb_2O_6$ [7],
- Sillenites: $Bi_{12}SiO_{20}$, $Bi_{12}GeO_{20}$ [8], $Bi_{12}TiO_{20}$[9],
- III-IV Semiconductors: GaAs [10], CdS[11], InP[12],
- Electro-optic ceramics $(Pb_{1-x}La_x)(Zr_yTi_z)O_3$[13].

The most advantages of the photorefractive properties are realized in crystals of the sillenite group. Crystal growing technology has been improved during the years. One is able to get easily large boules and elements with high optically quality. Sillenites can be doped by several types of impurities. Due to the different impurities (Ce, Fe, Rh, Cu, Co, Al, Cr, Mo…) one can change the characteristics of crystals [6, 14, 15]. On the other hand doped sillenites show high chemical, mechanical and optical stabilities during long periods of time in comparison with other crystals (like doped BCT). The crystals $Bi_{12}GeO_{20}$(BGO), $Bi_{12}SiO_{20}$(BSO) and $Bi_{12}TiO_{20}$(BTO) possess cubic symmetry which makes them isotropic and suitable for optical applications. It will be shown in chapter 3 that BTO has a maximal electrooptic coefficient. That's why it shows the best nonlinear electrooptical properties in its group.

The photo-induced absorption is the change of the absorption of light as the result of irradiation. Any influence of the light on the internal structure of the photorefractive crystals, which is connected with the energy redistribution of charge carriers, can change the absorption. The temporal and amplitude behavior of this effect depend strongly on the energy levels and the relaxation characteristics of the materials. Most of the characteristic effects are often disregarded in the quasi-stationary processes because of their short lifetime in the range of 1-100 ps or weak exposure intensities [16]. Sometimes the induced absorption can have lifetimes between seconds and even days.

The crystals of the sillenite group show long-lived strong photo-induced changes which were studied since the 90's and described as the reason for absorption gratings [17, 18]. During 1991-1993 Martin et al. reported about experimental investigations and the comparison of the photochromic effects in pure and doped (with Al and Fe) $Bi_{12}SiO_{20}$ and $Bi_{12}GeO_{20}$ crystals [19,20]. In 1999 Kobozev et al. investigated the light-induced absorption in $Bi_{12}TiO_{20}$ (BTO) [21]. In 2003 Marinova et al. studied the light-induced properties of $Bi_{12}TiO_{20}$:Ru and $Bi_{12}TiO_{20}$:Ca and showed the influence of impurity concentrations on the absorption and the photo-induced absorption with lifetimes of several hours [22-24]. In 2005 they reported the photo-induced absorption in planar waveguides based on thin films of $Bi_{12}TiO_{20}/Bi_{12}SiO_{20}$ and $Bi_{12}TiO_{20}$:Cu/ $Bi_{12}SiO_{20}$ crystals [25]. All crystals of the sillenite group $Bi_{12}MO_{20}$ (where M = Si, Ti, Ge) show long-lived induced absorption due to external irradiation. The induced response is caused by the redistribution of charge carriers on the traps in the valence band. The structure of the traps depends on the impurities. Substantially the impurities and temperature have decisive influence on the spectrum of the photo-induced

absorption, which was shown by Martin et al. and Briat et al. [19, 20, 26-33]. An induced absorption in pure sillenite crystals like $Bi_{12}SiO_{20}$ and $Bi_{12}GeO_{20}$ could be detected at low temperatures. For temperatures higher than 100-150 K the photo-induced absorption was neglected. In spite of the long ago first observation of the photo-induced absorption in sillenites most of the works is devoted to doped crystals of the sillenite groups at low temperature. The general aim of this work is the investigation of the long-lived photo-induced processes in the pure crystal $Bi_{12}TiO_{20}$ as reason of strong long-lived absorption at room temperature. The understanding of the induced properties of the pure crystals clears up the effects in the doted crystals. The developed models can be used as a base for describing of more complex systems. The investigation at room temperature gives more information about possibilities for the application and control of the effects.

1.2 Aims

Our aim is to present an almost complete and experimentally proved theory of the long-lived photo-induced absorption in the crystals of the sillenite group. We are focused on BTO as the sillenite crystal with the highest non-linear properties. Main tasks of our work are:

I. Experimental and theoretical investigation of the photo-induced and dynamical properties of long-lived processes in BTO crystals.

II. Comparison of the photo-induced properties of the BTO crystal with other sillenite crystals

III. Development of control methods of the induced absorption

IV. Investigation of possible applications of the long-lived induced properties in photorefractive BTO crystals.

In chapter 2 a review of the main publications connected with the photo-induced properties is given. Main conceptions of the light absorption in semiconductors are shown. The process of charge carriers redistribution in photorefractive crystals is discussed. The influence of the photo-induced changes on the optical properties is shown. In chapter 3 a short overview of the properties of sillenite photorefractive crystals and methods of their growing is given. Attention is focused on the crystal $Bi_{12}TiO_{20}$ (BTO), which properties are compared with the crystals $Bi_{12}SiO_{20}$ (BSO) and $Bi_{12}GeO_{20}$ (BGO). Chapter 4 is devoted to the study of long-lived photo-induced temporal and spectral properties of BTO which are compared with

the spectral properties of BSO. The results are analyzed and used for the manipulation of the photo-induced long-lived effects in sillenite crystals. On the base of the induced absorption new control methods for optical storage and processing of information are proposed in chapter 5. In chapter 6 the main theoretical and experimental results of the investigations are summarized.

Ehrenwörtliche Erklärung

Ich erkläre hiermit ehrenwörtlich, dass ich die vorliegende Arbeit selbständig, ohne unzulässige Hilfe Dritter und ohne Benutzung anderer als der angegebenen Hilfsmittel und Literatur angefertigt habe. Die aus anderen Quellen direkt oder indirekt übernommen Daten und Konzepten sind unter Angaben der Quelle gekennzeichnet.

Niemand hat mir bei der Auswahl and Auswertung des Materials geholfen. Niemand hat von mir unmittelbar oder mittelbar geldwerte Leistung für Arbeiten erhalten, die im Zusammenhang mit dem Inhalt der vorgelegten Dissertation stehen.

Die Arbeit wurde bisher weder im In- noch im Ausland in gleicher oder ähnlicher Form einer anderen Prüfungsbehörde vorgelegt.

Die geltende Promotionsordnung der Physikalisch-Astronomischen Fakultät ist mir bekannt.

Ich versichere ehrenwörtlich, dass ich nach bestem Wissen die reine Wahrheit gesagt und nichts verschwiegen habe.

Jena, den 24.06.2010 Andrew Matusevich

Danksagung

Ich möchte Prof. R. Kowarschik für die Möglichkeit danken, diese Arbeit am Institut für Angewandte Optik anzufertigen.

Besonders danke ich ihm, Dr. A. Kießling und Dr. V. Matusevich für die interessante und aufschlussreiche Aufgabenstellung, die freundliche Betreuung und die hilfreichen Diskussionen, Hinweise und Ratschläge.

Ich bedanke mich bei allen Mitarbeitern des Institutes für die nette Arbeitsatmosphäre und die stete Hilfsbereitschaft.

Ich danke auch Prof. S. Shandarov und Prof. A. Tolstik für die hilfreichen Hinweise zu meinen Experimenten.

Lebenslauf

Name:	Andrew Matusevich
Geburtsdatum:	24.07.1984
Geburtsort:	Minsk (Weißrussland)

1991 – 1999	Schule in Minsk
1999 – 2001	Gymnasium in Minsk
2001 – 2005	Weißrussische Staatliche Universität Minsk, Abschluß Bakkalaureat
2005 – 2006	Weißrussiche Staatlische Universität Minsk, Abschluß Diplom
2006 – 2007	Weißrussiche Staatlische Universität Minsk, Abschluß Magister
seit 2006	Friedrich-Schiller-Universität Jena, Promotionsstudium

Jena, 24.06.2010 Andrew Matusevich

Chapter 2

Nature of photo-induced processes in photorefractive crystals

Most of the photo-induced processes in photorefractive semiconductors are based on the following properties of materials:

- photoexcitation of the charge carriers,
- photoconductivity,
- localization of the charge carriers at donor and acceptor levels (relaxation),
- response of the media on the charge redistribution (light absorption, electro-optical, pyroelectric, piezoelectric and other effects).

These microscopic properties govern such macroscopic phenomena in materials like light absorption, conductivity, holographic sensitivity etc. The most significant responses for the photorefractive crystals are linear electro-optical and induced light absorption effects. The photorefractive phenomenon is based on the local refractive index variations of a medium under spatially inhomogeneous illumination.

Different theoretical models are available for describing of charge carriers redistribution between energy levels:

- single-level model [10, 8] with separate electron [12] and hole conductivity [8] or combined electron-hole conductivity [11, 12, 34],
- two-level model [35-38],
- multiple level model [39-41].

Knowing the characteristics of these models, one can combine them to describe more complex effects, e.g., to derive a multilevel model with a combined electron-hole conductivity. Moreover, the problem may be more complicated if we include a possible ionization order of each of the sublevels.

We study the induced processes in photorefractive sillenite $Bi_{12}TiO_{20}$ crystals. It will be experimentally shown later in chapter 4 that the main photo-induced phenomena of the crystal are the photorefractive effect and the photochromic effect. Only they can effectively influence on the optical properties of the material during long time and have possible applications. Both of them are the result of the space redistribution of the charge carriers between the traps with different spectral (energy) characteristics. In the case of the photorefraction the electro-optical effect plays the main role. In the case of the photochromic effect the photo-induced absorption is the main effect.

In this chapter we present a review of the main basic physical principals of the photo-induced processes in semiconductor optical solid materials. Chapter 2.1 describes the absorption of the light as the case of the excitation of the charge carriers. Spatial attention is paid for spectral characteristics of the absorption which mainly takes place in the case of the stationary absorption of the non-irradiated crystal and with already excited charge carriers. Chapters 2.2 and 2.3 are devoted to models which are commonly used for the energy redistribution of the excited charge carriers between levels and in the space. The induced changes due to inhomogeneous irradiation and the electro-optical effect are shown too. Chapter 2.4 describes phenomena which cause the spatial redistribution of excited free charges. Chapter 2.5 is a summary of basic physical principles of the photo-induced processes in sillenite crystals.

2.1 Impurity light absorption of semiconductor compounds

Processes of optical absorption due to impurity centers have various reasons. They can be caused by transfers of the charge carriers from localized impurity states to one of the allowed levels or another localized state. In the first case the absorption is attended by the generation of free charge carriers with the same charge. The integral spectrum of absorption looks like a wide band. In the second case free charge carriers are not generated. The absorption spectrum has narrow lines. There is also optical absorption with initiation of the

excitons connected with impurity centers (bound excitons), and absorption caused by the stimulation of localized vibrations of the impurity atoms.

Thus, following processes cause the doped absorption in crystals [42]:

1) photoionization of impurities,
2) photoexcitation of impurities,
3) photoneutralization of impurities,
4) photogeneration of bound excitons,
5) photoexcitation of localized vibrations of impurity atoms.

The electron transitions connected with the impurity absorption (processes 1-5) are illustrated in Fig. 2.1

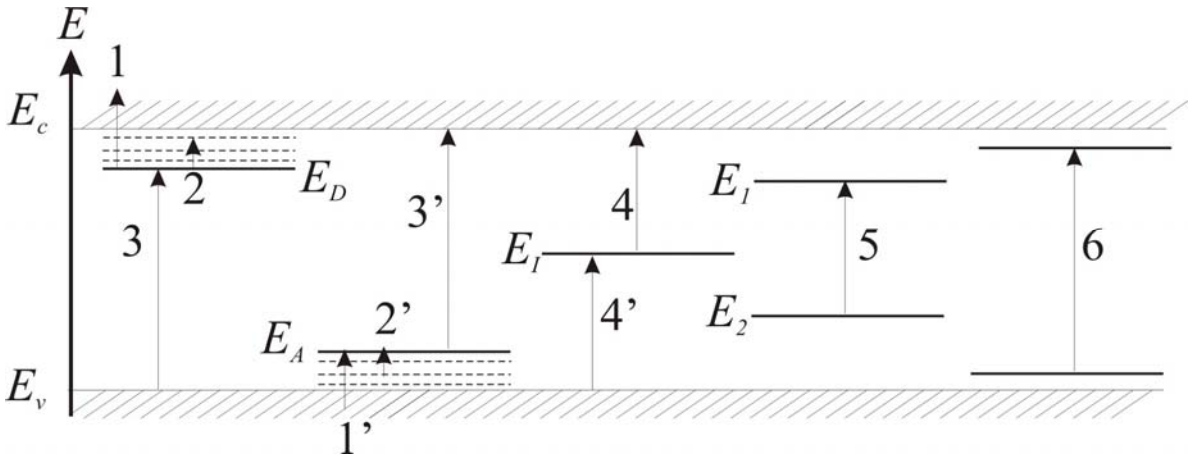

Fig. 2.1. Electron transitions that are responsible for the impurity absorption:
1, 1' – photoionization, 2, 2' – photoexcitation, 3, 3' – photoneutralization of shallow hydrogen-like impurities, 4, 4' – photoionization and photoneutralization of deep impurities, 5 - intracenter transition, 6 – photogeneration of the bound exciton. E_c – energy edge of the conducting band, E_v –energy edge of the valence band, E_D – donor's energy level, E_A – acceptor's energy level, E_I – energy of the ionization.

2.1.1 Photoinonization of shallow impurities

This process is connected with the transition of a electron (hole) from the bound state to the free state after absorption of the photon $\hbar\omega$ (transition 1 to 1' in Fig. 2.1). The energy of the photon has to be greater than the binding energy between electron (hole) and donor (acceptor), i.e. E_D (E_A). Before the interaction with the photon the charge carrier was localized at the impurity center, and the impurity atom was neutral. The interaction is accompanied with the transition of the charge carrier to the free zone, i.e. ionization of the

impurity. The spectra of the absorption for such processes will be defined by the electronic structure of the impurity state and the structure of the free state to which the transition takes place.

Shallow impurity states can be described as an approximation of the effective mass with help of a hydrogen like model. The minimal energy necessary for photoionization (boundary energy) is equal to E_D. When the energy of the photon $\hbar\omega$ is equal to E_D, the electron transition takes place to the level of the minimal free energy. The density of the allowed states in the conductivity band is proportional to the square root of the energy. Thus for growing of $\hbar\omega$ there is a rapid increase of the absorption (Fig. 2.2). For $\hbar\omega > E_d$ the density of the end states in the allowed band increases but the density of the initial states decreases. That's why there is a typical maximum and fall in the spectrum of the absorption $k_\omega(\hbar\omega)$ (Fig. 2.2).

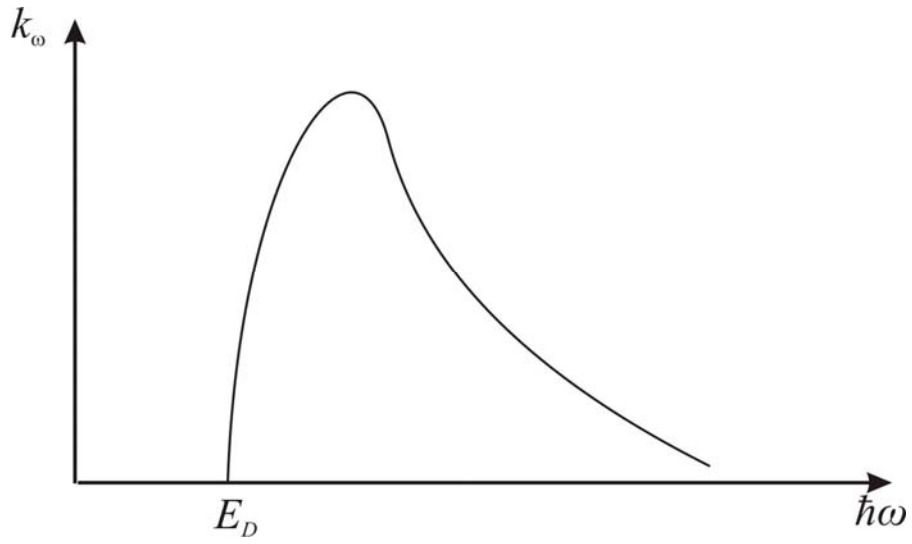

Fig. 2.2. Scheme of the optical absorption spectrum, caused by photoionization of the hydrogen-like donor. k_ω- coefficient of the light absorption.

For the common hydrogen like impurities the spectrum of absorption caused by the photoionization is described by [43]

$$k_\omega = A\frac{(\hbar\omega / E_D - 1)^{3/2}}{(\hbar\omega / E_D)^5}, \tag{2.1}$$

where A is the proportionality factor connected with the density of donors N_D, E_D is the energy of ionization, m_n is the effective mass of electrons

$$A = \frac{128\pi e^2 \hbar}{3cnm_n E_D} N_D . \tag{2.2}$$

where c is the velocity of light, n is the number of the bound states level, e is the elementary charge.

The maximum of the function (2.1), i.e. the maximum of the photoionization spectrum, is found for

$$\hbar\omega = \frac{10}{7} E_D . \tag{2.3}$$

The photoionization processes of acceptors have the similar mechanism.

2.1.2 Photoexcitation of shallow impurities

Photoexcitation is caused by electron (hole) transition from the bound state with n = 1 (fundamental state) to another state (excited state) with n = 2, 3, 4, … after the photon absorption (transitions 2 and 2' in Fig. 2.1). Such transitions take place between discrete energy levels. The absorption spectrum consists of a series of discrete narrow absorption lines when the energy of the photon is less then the energy of ionization (Fig. 2.3).

The processes of photoexcitation and photoionization of shallow impurities take place in semiconductors at low temperatures when $kT << E_D(E_A)$ and the impurities are not thermally ionized. The ionization energies of the shallow traps in semiconductors are 5-100 meV. That's why the spectra of ionization are localized in the deep IR range (λ = 10…200 μm) [42].

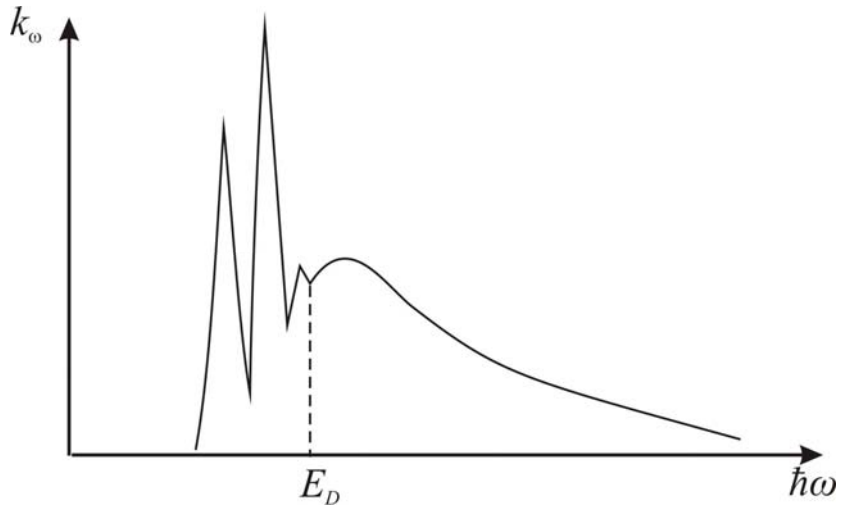

Fig. 2.3. Scheme of an optical impurity absorption spectrum (E_D - donor ionization energy)

2.1.3 Photoneutralization of shallow impurities

Photoneutralization is caused by transitions of electrons from the valence band to levels of the ionized donors nearby to the bottom of the conducting band or from the levels of ionized acceptors to the conducting band (transitions 3 and 3' in Fig. 2.1 p. 8). Such transitions are possible only when the impurity centers are ionized e. g. due to simultaneous doping by acceptors and donors (as the result of compensation). Photoneutralization of the acceptors and the donors in the semiconductors is accompanied by additional absorption bands with an energy of photons $\hbar\omega \geq [E_g - E_D(E_A)]$. For shallow impurities $E_D(E_A) << E_g$ the absorption spectrum usually merges with the spectrum of the fundamental absorption and appears as an additional "step" of the fundamental absorption band. When the ionization energy of the impurity is small and the concentration of centers is high than an impurity band is formed. It merges with the band of allowed values of energies. The photoneutralization band of the impurity merges with fundamental absorption and is negligible. Such transitions are often named "quasiintraband" transitions.

2.1.4 Photoionization and photoneutralization of deep impurities

Like the photoionization and photoneutralization of shallow impurities photoionization and photoneutralization of deep impurities are based on the transition impurity-band or band-impurity (transition 4 and 4' in Fig. 2.1 p. 8). The impurity absorption based on deep non hydrogen-like impurities shows itself as a wide structureless absorption bands. These bands are in the range of photon energies between the energy of the ionization E_I (or neutralization E_g-E_I) and the edge of the fundamental absorption. The absorption spectra for photoionization of deep centers can be approximated by [43]

$$k_\omega = B\frac{(\hbar\omega / E_I - 1)^{1/2}}{(\hbar\omega / E_I)^3}, \tag{2.4}$$

where E_I – optical ionization energy of the center, B – coefficient is proportional to the centers density. Equation (2.4) corresponds to the non-Coulomb (short-range) potential, localized in boards of the central cell. Due to the space localization of the charge the deep impurities are accompanied by the interaction with vibrations of the lattice and with local vibrations of the center. That's why the electron-phonon interaction can influence on the absorption spectra at the long-wave part of the spectrum. The absorption spectrum calculated

with (2.4), i.e. without electron-phonon interaction, is shown in Fig 2.4. The dotted curve is for absorption with the electron-phonon interaction. The electron-phonon interaction gives an exponential decrease of the absorption at the long-wave spectrums part against a sharp boundary. The exponential decrease depends on the temperature and the characteristics of the electron-phonon interaction.

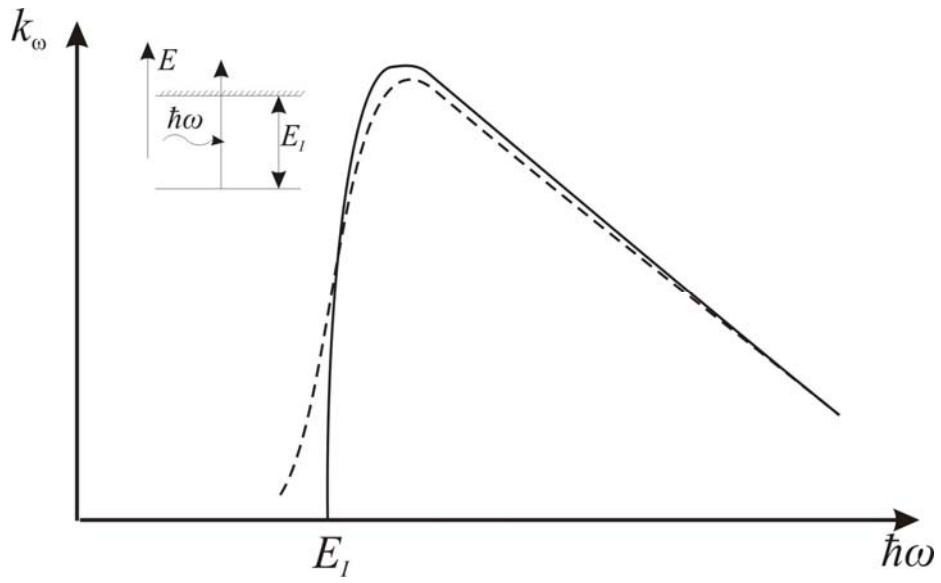

Fig. 2.4. Impurity absorption general spectra caused by photoionization of deep centers without (solid line) and with (dotted line) accounting of electron-phonon interaction

2.1.5 Intracenter transition

Intracenter transition is caused by the electron transition of the impurity center from one allowed state E_1 to another allowed state E_2 (transition 5 in Fig. 2.1 p. 8). The charge carriers remain bound with the center. The intracenter transition is similar to the photoexcitation of the shallow hydrogen-like impurities in semiconductors, but it takes place in transitions between the deep states and without hydrogen-like series of lines in the absorption spectrum [33, 42].

Typical examples of impurities with high optical absorption caused by intracenter transitions are elements with non occupied inner shells (3*d* – Fe-group, 4*f* – lanthanide – group, 5*f* – actinide group). These shells are well screened (especially 4*f* and 5*f*) by 4*s*-, 5*s*-, 5*p*- and 6*s*- electrons against an external action. That's why after allocation in crystalline or amorphous matrixes such atoms retain the properties of free ions. Electron transitions between

energy states of the inner 3*d*-, 4*f* – shallows are intracenter transition. The corresponding lines of the absorption can be widened due to splitting and widening of energy levels of impurity centers under the influence of the crystal lattices field.

2.1.6 Bond exciton absorption

Bond exciton absorption is caused by the generation of an exciton bond to the defect due to photon absorption (transition 6 in Fig. 2.1 p. 8).

The nonequilibrium electron and hole can generate an exciton localized at a defect "bond" as well as a moving "free" exciton. The binding energy of the bond exciton is counted from the energy of the free exciton, i.e. from exciton width of the energy gap. The energy of the bond exciton has to be less then the energy of the free exciton. Only than the bond exciton has a stable state. An exciton becomes bond in the potential well near to the defect. The bond exciton is localized, i.e. it is accompanied with narrow lines nearby a forbidden band in the absorption spectra [30, 42, 44].

In most cases excitons are at the neutral centers. But under special conditions they can appear at the charged centers. There is a most effective formation of bond excitons at the isoelectron impurities (traps). An isoelectron impurity is any impurity with isoelectron displacement of the main atom of the lattice. Not every isoelectron impuritiy of displacement can bond excitons. Bonding only takes place when impurity and displaced atom differ in electronegativity and in covalent atomic radius. Then an impurity center generates a potential well and the electron (hole) can be trapped by it. After the charge carrier of defined polarity being localized the isoelectron center obtains charge (in contrast to donors and acceptors). Then a carrier of another polarity can be easily trapped and an exciton is generated.

2.1.7 Absorption at local vibrations of impurities

The absorption can be caused by the impurity atom vibration too. The impurity atom is bounded with main atoms of lattice by elastic forces. The frequency of the impurity vibration differs from the ideal lattice vibration. That's why in the IR absorption spectra new resonance lines can appear as a result of local vibration excitation. These vibrations don't change the main electron-energy structure of the crystal. That's why it is impossible to present it at the general diagram (Fig. 2.1 p. 8) [42].

2.2 Single-level model

A single-level model has been developed at the beginning of the investigation of the photorefractive effect. The first equations were derived in 1971 [45]. A complete system of mathematical equations proposed in the works of Kukhtarev et al. (e.g., see [9]) gives the adequate explanation for the results obtained using the crystals *LiNbO₃:Fe* and *LiNbO₃:Cu*. Because of this, the model has been readily accepted and tested for other materials as well.

Fig. 2.5 presents a single-level model as a diagram of levels. Electrons are excited under the effect of illumination or thermally, leaving the filled traps (donors) D^- and entering the conduction band. Free electrons within the conduction band may recombine into the empty traps (donors) D^0. Equations (2.5) and (2.6) describe similar motion of charge carriers [9]

$$\frac{\partial N^-}{\partial t} = -(\beta + s \cdot I) \cdot N^- + r \cdot N^0 \cdot N_e , \tag{2.5}$$

$$N^D = N^- + N^0 , \tag{2.6}$$

where N^D − possible maximum charge concentration at the traps, N^- − concentration of trapped charges D^-, N^0 − concentration of the "empty" traps D^0 "ready" to accept the recombining charges, β − thermal excitation coefficient, s − excitation cross-section of a charge, I − light intensity measured in [photon/m^{2}s], r − recombination degree, N_e − electron concentration within the conduction band. The charges are excited in illuminated regions, migrating to darker regions to recombine there. A mechanism of charge motion within the conduction band will be analyzed in detail later, and first we discuss the charge redistribution between energy levels.

For homogeneous illumination of a material in the equilibrium state equation (2.5) gives the concentration of free carriers within the conduction band and hence the photoconductivity σ as a function of the light intensity as follows

$$\sigma = e \cdot \mu_e \cdot N_e , \tag{2.7}$$

$$N_e = \frac{\beta + s \cdot I}{r} \cdot \frac{N^-}{N^0} , \tag{2.8}$$

where e − elementary charge, μ_e –charge mobility (mobility tensor in the general case). At small thermal excitation coefficients ($\beta << s \cdot I$) the photoconductivity is linearly growing with the intensity as a ratio of filled and empty electron traps.

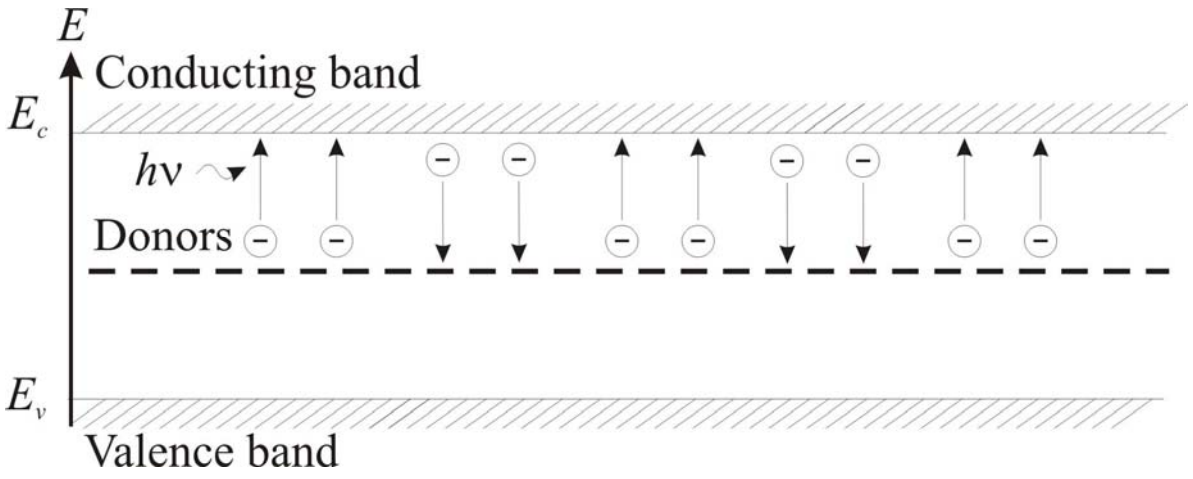

Fig. 2.5 Single-level model

The material absorption factor is nothing else but $k = s \cdot N^{-}$. In this way the charge excitation results in a decreased number of the photorefractive centers N^{-} in traps D^{-} and hence in lowering of the absorption factor $\Delta k = k(I) - k(I = 0)$.

At high coefficients of thermal excitation the concentration of photorefractive centers in the traps is dramatically decreased. The contribution made by the intensity of a light wave into the increased conductivity becomes lower, in the limit tending to the function $\sigma \propto I^{1/2}$ [46].

Inhomogeneous illumination of a crystal causes spatial redistribution of the charge. In the case of an arbitrary illumination the problem of determining the charge distribution density for the spatial light-intensity distribution is undecidable. That's why one uses sinusoidal light intensity distribution

$$I = I_0 \cdot \left[1 + m \cdot \cos(K \cdot x)\right], \tag{2.9}$$

where I_0 − background intensity, K − vector magnitude of a grating recorded within a crystal, m − intensity modulation depth, x − coordinate axis.

The process may be qualitatively described as follows. In regions of high illumination the charges are excited into the conduction band, where, due to diffusion and drift mechanisms, the charges migrate to the low-intensity regions to recombine in the traps. The charge density thus changed creates the internal electrical field E_{sc}. This field of redistributed charges is called the *space charge field*. The charge density as well as the created electrical field is characterized by the sine-formed spatial and intensity distribution (2.9). However, the

electrical field has a phase shift that is analytically determined in the stationary state by Kukhtarev equation [9]

$$E_{sc}(I) = -m \cdot \left[R_{OC}(I) \cdot E_0 + E_{phv} + i \cdot R_{OC}(I) \cdot E_D \right], \tag{2.10}$$

where

$$R_{OC} = \frac{1}{1 + \dfrac{\beta}{s \cdot I}} = 1 - \frac{\sigma(I=0)}{\sigma(I)}, \tag{2.11}$$

$$E_{phv} = \frac{\varpi \cdot N^{-} \cdot I}{e \cdot \mu_e \cdot N_e}, \tag{2.12}$$

and

$$E_D = \frac{k_B \cdot T}{e} \cdot K, \tag{2.13}$$

Here ϖ − bulk photovoltaic coefficient, k_B − Boltzmann constant, T − temperature. As seen from equations (2.10)-(2.13), a field of the spatially distributed charge consists of three components: external field E_0, bulk photovoltaic field E_{phv}, and diffusion field E_D. The external and photovoltaic fields are coincident in phase with the light intensity modulation, whereas diffusion is responsible for the phase shift $\frac{\pi}{2}$. At a relatively high light intensity the attenuation factor R_{oc} is equal "1". The physical meaning of this factor resides in the fact that a part of the carrier modulation distribution is lowered due to the dark conductivity $\sigma\ (I = 0)$.

Grating recording and deleting are monoexponential processes with characteristic time [6]

$$\tau = (1 + \frac{E_D - i \cdot E_0}{E_M}) \cdot \tau_M, \tag{2.14}$$

$$E_M = \frac{r \cdot N^{-}}{K \cdot \mu_e}, \tag{2.15}$$

$$\tau_M = \frac{\varepsilon \cdot \varepsilon_0}{e \cdot \mu_e \cdot N^0}, \tag{2.16}$$

ε − dielectric constant.

The works performed at the 1987-1989 demonstrate combined electron and hole conductivity in experiments with two-wave mixing in photorefractive crystals. A relative contribution of each of the charge types depends on the wavelength of light and the redox

state of the crystal [45]. Detailed descriptions of the charge transfer process were independently published in 1986 by Valley [12] and Strohkendl, Jonathan, Hellwarth [11].

For the electron-hole conductivity in photorefractive materials two different physical models are available [12]. The first model is based on a single-level model (Fig. 2.6). At the same time, the thermal and photo-induced electron transitions to the levels D^0 and the recombination from the level D^- with holes within the valence band are included supplementary. Obviously, equation (2.5) should involve two additional terms on the left side [11, 12]

$$\frac{\partial N^-}{\partial t} = -(\beta_e + s_e \cdot I) \cdot N^- + r_e \cdot N^0 \cdot N_e - (\beta_h + s_h \cdot I) \cdot N^- + r_h \cdot N^0 \cdot N_h , \qquad (2.17)$$

where the indices *e* and *h* identify the electron and hole conductivity, respectively.

The second model is concerned with levels of two types. At one level the predominant carriers are electrons, and at the second level − holes (Fig. 2.3 p 10.). In this case equation (2.5) for the electron redistribution remains the same but a similar equation is added for the hole conductivity.

Under homogeneous illumination the photoconductivities are determined by both models as

$$\sigma = \sigma_e + \sigma_h , \qquad (2.18)$$

$$\sigma_e = e \cdot \mu_e \cdot N_e , \qquad (2.19)$$

$$\sigma_h = e \cdot \mu_h \cdot N_h , \qquad (2.20)$$

where σ_e and σ_h − electron and hole conductivities, μ_e and μ_h − mobility of electrons and holes, respectively; N_e and N_h − density of electrons and holes within the conduction and valence bands, respectively. For negligible coefficients of thermal excitation this model predicts the light-intensity dependence of the photoconductivity as well.

Under inhomogeneous illumination, electrons and holes diffuse from more illuminated regions to darker ones. As a result of differing signs of the charges, the formed fluxes tend to compensate each other.

When we consider one center with the transition to the valence and to the conduction band (Fig. 2.6), the stationary field of the redistributed electric charge has the form [11 - 13]

$$E_{sc} = -m \cdot (E_0 + i \cdot R_{eh} \cdot E_D) , \qquad (2.21)$$

where

$$R_{eh} = \frac{\sigma_e - \sigma_h}{\sigma_e + \sigma_h} , \qquad (2.22)$$

and thermal excitation is neglected.

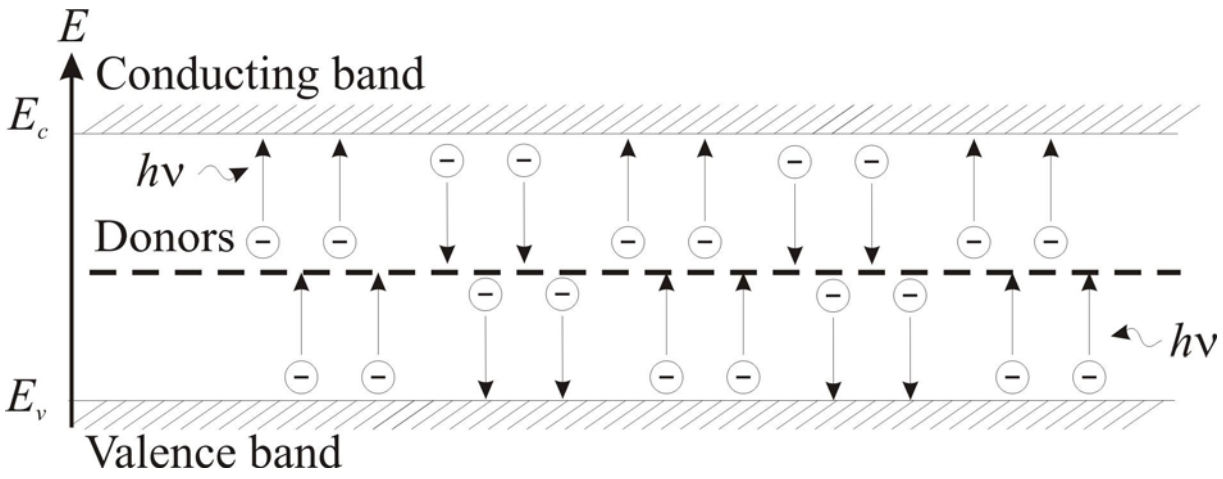

Fig. 2.6: Single-level model with electron-hole conductivity

The formation and decay of the photo-induced structure proceed exponentially with the characteristic time

$$\tau_{sc} = \frac{\varepsilon \cdot \varepsilon_0}{\sigma_e + \sigma_h}. \tag{2.23}$$

In this manner the existence of conductivity of both types causes the decrease of the electric field of the redistributed charge.

In case of different centers for electrons and holes (Fig. 2.7) the charges at these centers interact only due to the electrical field [12, 13].

$$E_{sc} = -\frac{\sigma_e(I) + \sigma_h(I)}{\sigma_e(I=0) + \sigma_h(I=0)} \cdot E_0 - i \cdot \frac{\sigma_e(I) - \sigma_h(I)}{\sigma_e(I=0) + \sigma_h(I=0)} \cdot E_D. \tag{2.24}$$

This field is quasi-stationary as σ_e and σ_h are decreasing in time.

The phase shift of the grating ($-\pi/2$ or $+\pi/2$) depends on the concentration of the centers. In the equilibrium state the center with the most effective carrier is dominant, creating a diffusion field. Experimentally, recording and decay of a structure takes much longer time than is given by the formula (2.23).

Besides, with the use of a single-level model for both charge types or with another model, where there is a separate level for each type of the carriers, a grating may be initially recorded with one characteristic time subsequently reaching a maximum, and then degenerates to a certain steady state with another characteristic time. Such an effect is exhibited because of the difference in electron and hole mobilities ($\mu_e > \mu_h$). Electrons are

distributed more rapidly creating the associated grating, and in some period of time the grating formed by electrons is compensated by holes.

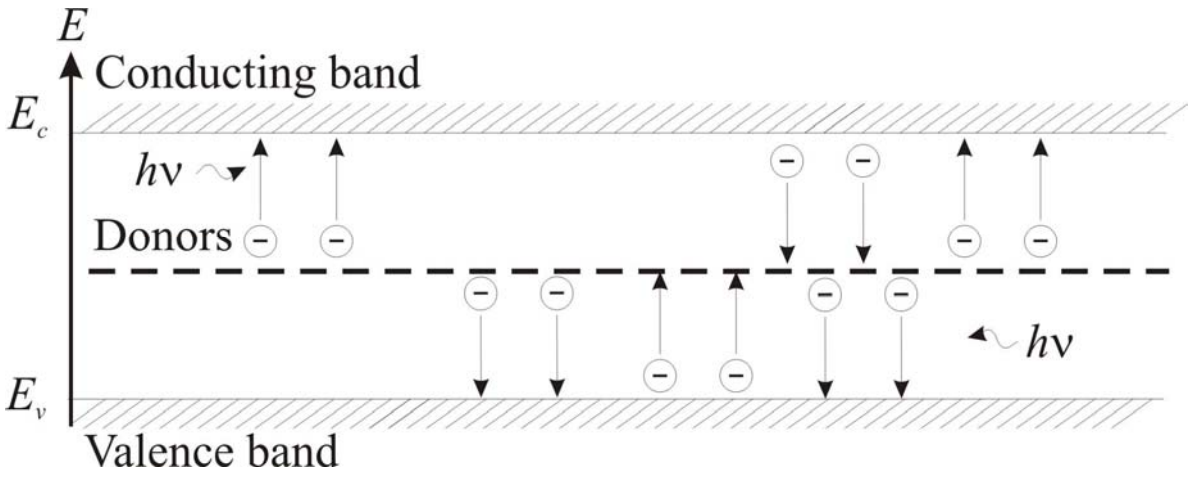

Fig. 2.7: Single-level model with electron-hole conductivity and levels of two types

2.3 Two-level model

A two-center model was proposed by Valley in 1983 to explain the erasure of a holographic grating in a photorefractive material with two distinct characteristic times [47]. Proceeding from their experimental results, in 1986 Leaux, Roosen, and Brun suggested the existence of so called shallow traps responsible for the charge transfer along with the deep ones [48]. The light-induced variations of the absorption factor were explained in 1988 by Brost, Motes, and Rotge with the well-known two-level model [38]. They have considered a high thermal excitation coefficient for charges from shallow traps which was a key moment for understanding of the energy and temperature dependences and also for the explanation of the time evolution of photorefractive properties in materials. Later this model has been used to treat the photoconductivity [35, 36].

Fig. 2.8 gives a schematic diagram of a two-level model, where traps of two types are involved (D_1 and D_2). Each type may be in two valence states: filled D^- and excited D^0. The traps D_1 are deep and traps D_2 are shallow with respect to the conduction band.

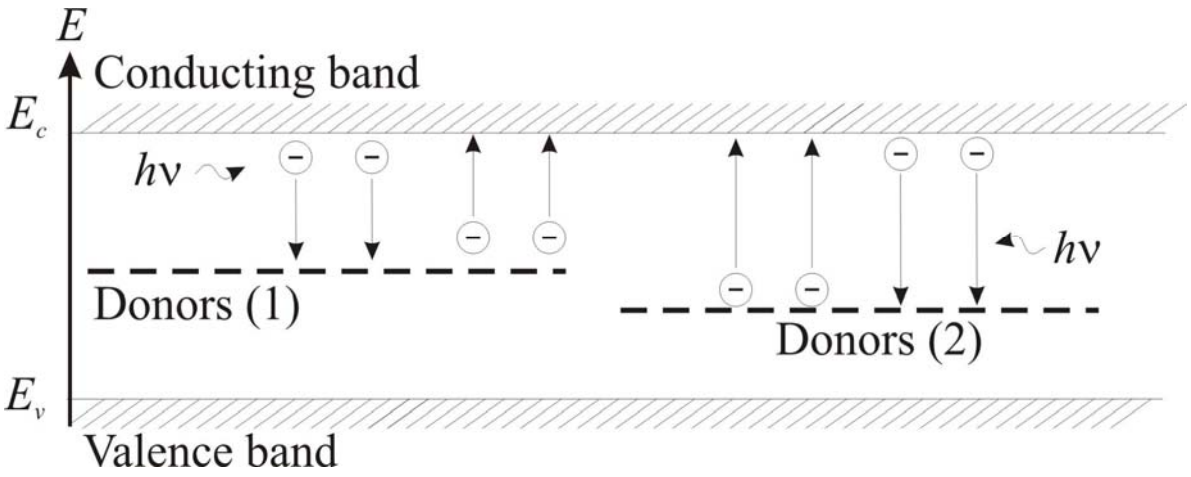

Fig. 2.8: Two-level model

The model is described with the system of equations [38]

$$\frac{\partial N_1^-}{\partial t} = -(\beta_1 + s_1 \cdot I) \cdot N_1^- + r_1 \cdot N_1^0 \cdot N_e , \tag{2.25}$$

$$\frac{\partial N_2^-}{\partial t} = -(\beta_2 + s_2 \cdot I) \cdot N_2^- + r_1 \cdot N_2^0 \cdot N_e , \tag{2.26}$$

$$N_1 = N_1^- + N_1^0 , \qquad N_2 = N_2^- + N_2^0 . \tag{2.27}$$

The variables have been already described for the single-level model.

Let us consider the case of homogeneous illumination. In the dark the population of the level D_1 is much greater than that of the level D_2 because the thermal excitation coefficient for shallow traps β_2 is much higher compared to β_1 for deep traps, i.e. a quantity of the traps in the state D_2^0 is negligible as compared to that of D_1^-, D_1^0, and D_2^-. Being illuminated, electrons are excited from the traps D_1^- and D_2^- to recombine in the traps D_1^0 and D_2^0. But due to thermal excitation from shallow traps, the charge density in D_2 is always lower than that in D_1. The photoconductivity in this case is theoretically described in [35, 36] as follows

$$\sigma_e = e \cdot \mu_e \cdot N_e , \tag{2.28}$$

where

$$N_e = -\frac{g_1}{2 \cdot r_1} \cdot \frac{N_2 - N_A}{N_1 + N_2 - N_A} - \frac{g_2}{2 \cdot r_2} \cdot \frac{N_1 - N_A}{N_1 + N_2 - N_A} + \\ + \left[\left(\frac{g_1}{2 \cdot r_1} \cdot \frac{N_2 - N_A}{N_1 + N_2 - N_A} + \frac{g_2}{2 \cdot r_2} \cdot \frac{N_1 - N_A}{N_1 + N_2 - N_A} \right)^2 + \frac{g_1 \cdot g_2}{r_1 \cdot r_2} \cdot \frac{N_A}{N_1 + N_2 - N_A} \right]^{\frac{1}{2}}, \tag{2.29}$$

$$g_1 = \beta_1 + s_1 \cdot I\,,\ g_2 = \beta_2 + s_2 \cdot I\,. \tag{2.30}$$

So, we have $\sigma \propto I^x$. N_A − concentration of immobile compensation charges supporting the medium electroneutrality (acceptors).

For low intensities ($I << \beta_2 s_2^{-1}$ but $I >> \beta_1 s_2^{-1}$) shallow traps are of little significance and hence $x \approx 1$. At $I \approx \beta_2 \cdot s_2^{-1}$ the presence of shallow traps becomes appreciable to result in an x below unity. As the density of electrons excited from deep traps becomes too high, they recombine to shallow traps. For very high intensities the theory predicts a linear dependence of the photoconductivity on the light intensity because recombination to shallow traps in this case is practically impossible.

Under inhomogeneous illumination the redistributed charge field has the form [37]

$$E_{sc}(I) = -i \cdot m \cdot E_D \cdot \frac{1}{1+\dfrac{E_D}{E_q}} \cdot \eta(I,K)\,, \tag{2.31}$$

$$E_q = \frac{e}{\varepsilon \cdot \varepsilon_0} \cdot \frac{1}{K} \cdot N_{eff}\,, \tag{2.32}$$

$$N_{eff} = \left(\frac{1}{N^-} + \frac{1}{N^0} \right)^{-1}. \tag{2.33}$$

However, equation 2.31 was derived for the case of the diffusion currents at the absence of drift currents. The function $\eta(I,K)$ is caused by an additional dependence for the internal field in a material on the light intensity and on the parameters of the recorded grating [37-41, 46-51]. In the particular case ($I << \beta_2 \cdot s_2^{-1}$) we have $\eta(I, K) = R_{oc}(I)$ (see equation 2.10). Experimentally, the value of the function η may be obtained by measurement of the photoconductuivity as $R_{oc}(I) = x(I)$, where $\sigma = I^{x(I)}$ [52].

An analysis of holographic recording within a model with two types of traps leads to very interesting conclusions. Two gratings are recorded at all times: one at deep and one at shallow traps, and the redistributed-charge field amplitude may be given by

$$E_{sc} = i \cdot \frac{e}{\varepsilon \cdot \varepsilon_0} \cdot \frac{1}{K} \cdot \left(N_1^- + N_2^- \right). \tag{2.34}$$

When we consider diffusion currents only, the distribution of N_1^- is always opposite in phase to the intensity distribution, whereas the distribution of N_2^- may be in phase or opposite in phase depending on the light intensity and spatial frequency of the grating [37]. At low

intensities and minor light modulation frequencies the gratings N_1^- and N_2^- compensate each other. In case of high intensities and high spatial frequencies both gratings are enhanced.
The basic effects involved in a two-level model as compared to the single-level one are as follows.

- *Holographic grating amplification after illumination of the photorefractive material is switched off*. Since the gratings in deep and shallow traps may compensate each other and there is a possibility of rapid thermal erasure of the grating at shallow traps as soon as the recording beams are switched off, one can usually observe amplification of the redistributed charge field E_{sc} [37, 53].
- *Increasing of the conductivity* after illumination switched off as a result of the appearance of rapidly excited electrons from shallow traps.

Thus, recording and erasure of a grating take place with two characteristic times, shorter times being associated with shallow traps and longer – with deep traps.

The two-level model may be extended for several trap types, though no principally new mechanisms have been found according to literature [54].

2.4 Charge spatial transport mechanisms in photorefractive semiconductor media

Redistribution of the photoinduced charges may occur by three different mechanisms: diffusion, drift, and photovoltaic effect. The corresponding currents are referred to in a similar way: diffusion $\vec{j}_{diff}$, drift $\vec{j}_{drift}$, and photovoltaic current $\vec{j}_{ph}$. The total current

$$\vec{j} = \vec{j}_{diff} + \vec{j}_{drift} + \overrightarrow{j_{ph}}, \tag{2.35}$$

is spatially inhomogeneous and time dependent in the general case.

In this chapter the attention is focused on the above-mentioned mechanisms of charge redistribution in photorefractive media.

2.4.1 Diffusion

Let us consider the case of electron conductivity. Being subjected to illumination, electrons are excited to the conduction band. On inhomogeneous illumination, the concentration of free carriers in the illuminated regions is higher than in the dark regions. The

difference of concentrations is responsible for the diffusion of the particles to more sparse regions. In these regions the particles may recombine, as a result creating a permanent charge density distribution. Fig. 2.9 shows a spatial charge distribution for the sine-shaped one-dimensional light-intensity modulation. The internal field E_{sc} is induced by redistributed charges. The field modulates the refractive index due to the Pockels effect or, in other words, generates a phase grating within the medium. To be precise, redistribution of the charge results in the formation of three charge-density gratings. The first grating associated with positively charged donors is determined by

$$\rho^{+}(x) = \rho \cdot \cos(K \cdot x) + \rho_0 , \tag{2.36}$$

where $\rho = \dfrac{e \cdot m \cdot I_0 \cdot t_{ex} \cdot s \cdot \alpha}{\hbar\omega,}$, ρ_0 average value of the positive charge density, t_{ex} exposure time, $\hbar \cdot \omega$ − photon energy.

The two other gratings are associated with negatively charged acceptors having the following charge densities

$$\rho_1^{-}(x) = -\frac{1}{2} \cdot \cos\left[K \cdot (x + L_d)\right] - \frac{1}{2} \cdot \rho_0 , \tag{2.37}$$

and

$$\rho_2^{-}(x) = -\frac{1}{2} \cdot \cos\left[K \cdot (x - L_d)\right] - \frac{1}{2} \cdot \rho_0 . \tag{2.38}$$

The formation of these gratings is due to electron diffusion in both directions from the excitation area. L_d is the diffusion length.

From the Poisson equation

$$div\vec{E}_{sc}(x) = \frac{\rho^{+}(x) + \rho_1^{-}(x) + \rho_2^{-}(x)}{\varepsilon \cdot \varepsilon_0} \tag{2.39}$$

it follows that the space-charge field may be determined as

$$E_{sc}(x) = \frac{\rho}{\varepsilon \cdot \varepsilon_0 \cdot K}\left[1 - \cos(K \cdot L_d)\right] \cdot \sin(K \cdot x), \tag{2.40}$$

where ε and ε_0 − dielectric constants in the vacuum and crystal, respectively. We consider a one-dimensional case. The field is modulated only along the *x*-axis.

For the special case $K \cdot L_d << 1$(short-length diffusion), that is common for the photorefractive media, the relation 2.40 may be simplified

$$E_{sc}(x) = \frac{\rho \cdot L_d^2}{2 \cdot \varepsilon \cdot \varepsilon_0} \cdot K \cdot \sin(K \cdot x). \tag{2.41}$$

It should be emphasized that in a diffusion mechanism the electric field is shifted relative to the light intensity distribution by $\pi/2$. Moreover, due to the increasing of the diffusion length and decreasing of the dielectric constant of the medium, the contrast of the redistributed-charge field E_{sc} is enhanced [14].

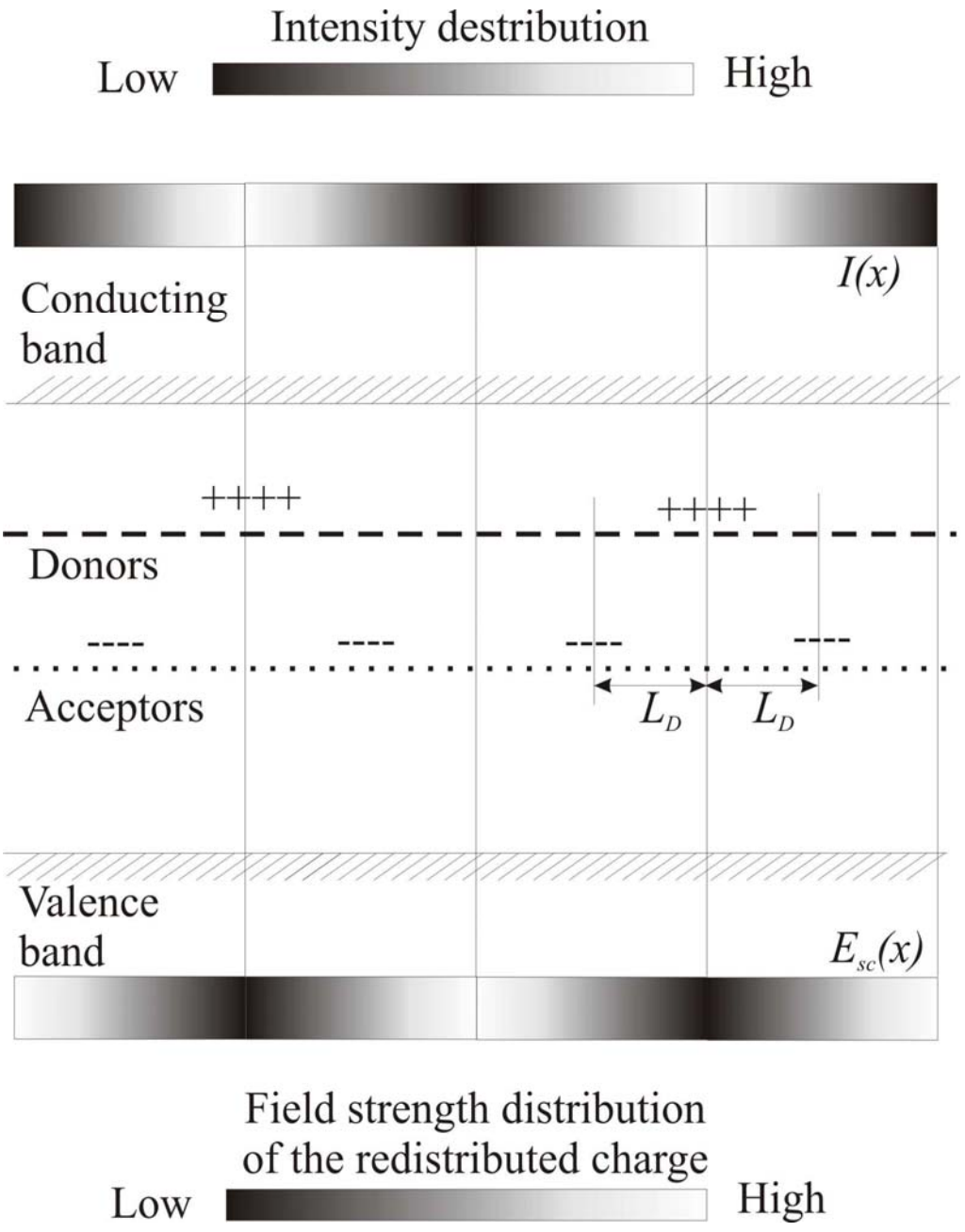

Fig. 2.9: Diffusion mechanism of the charge redistribution

During increasing of the light intensity the field amplitude E_{sc} rises up to the effective diffusion value $\left|\vec{E}_{sc}\right| = \left|\vec{E}_{D}\right|$. This field in the equilibrium state compensates the thermal motion of the electrons

$$E_D(x) = \frac{k_B \cdot T}{e} \cdot \frac{1}{N_e(x)} \cdot \frac{dN_e(x)}{dx}, \tag{2.42}$$

where $N_e(x)$ − concentration of free carriers. For the harmonic distribution of the light intensity $I(x) = I_0 \cdot [1 + n \cdot \cos(K \cdot x)]$ and at small modulation depths $m << 1$ we have

$$E_D(x) = m \cdot K \cdot \frac{k_B \cdot T}{e} \cdot \sin(K \cdot x). \tag{2.43}$$

In this case the diffusion current is determined as

$$j_{diff}(x) = \mu \cdot k_B \cdot T \cdot grad\left(N_e(x)\right), \tag{2.44}$$

where μ − charge mobility.

2.4.2 Drift

A distinctive feature of the drift mechanism is the fact that the motion of the excited electrons is due to an external electric field rather than due to the difference of the concentration densities. Fig. 2.10 demonstrates the special case for a homogeneous external field $E_0 \cdot L_0 = \mu \cdot \tau \cdot E_0$ − the drift length is covered by free electrons with the mobility μ during their lifetime τ. As before, a harmonic intensity modulation is considered.

The physical meaning of this process is as follows. The charge distribution for short-length drifts may be represented in the form of two gratings

$$\rho^{+}(x) = \rho \cdot \cos(K \cdot x) + \rho_0, \tag{2.45}$$

and

$$\rho^{-}(x) = -\rho \cdot \cos[K \cdot (x + L_0)] - \rho_0, \tag{2.46}$$

produced by positively-charged donors and negatively-charged acceptors, and the total charge density is

$$\rho = \rho^{+}(x) + \rho^{-}(x) = \rho \cdot (\cos(K \cdot x) - \cos[K \cdot (x + L_0)]). \tag{2.47}$$

For small drift lengths $K \cdot L_0 << 1$ we can determine from equation (2.39) a field of the redistributed charge as

$$E_{sc}(x) = -\frac{\rho}{\varepsilon \cdot \varepsilon_0} \cdot L_0 \cdot \cos\left[K\left(x + \frac{1}{2}L_0\right)\right]. \tag{2.48}$$

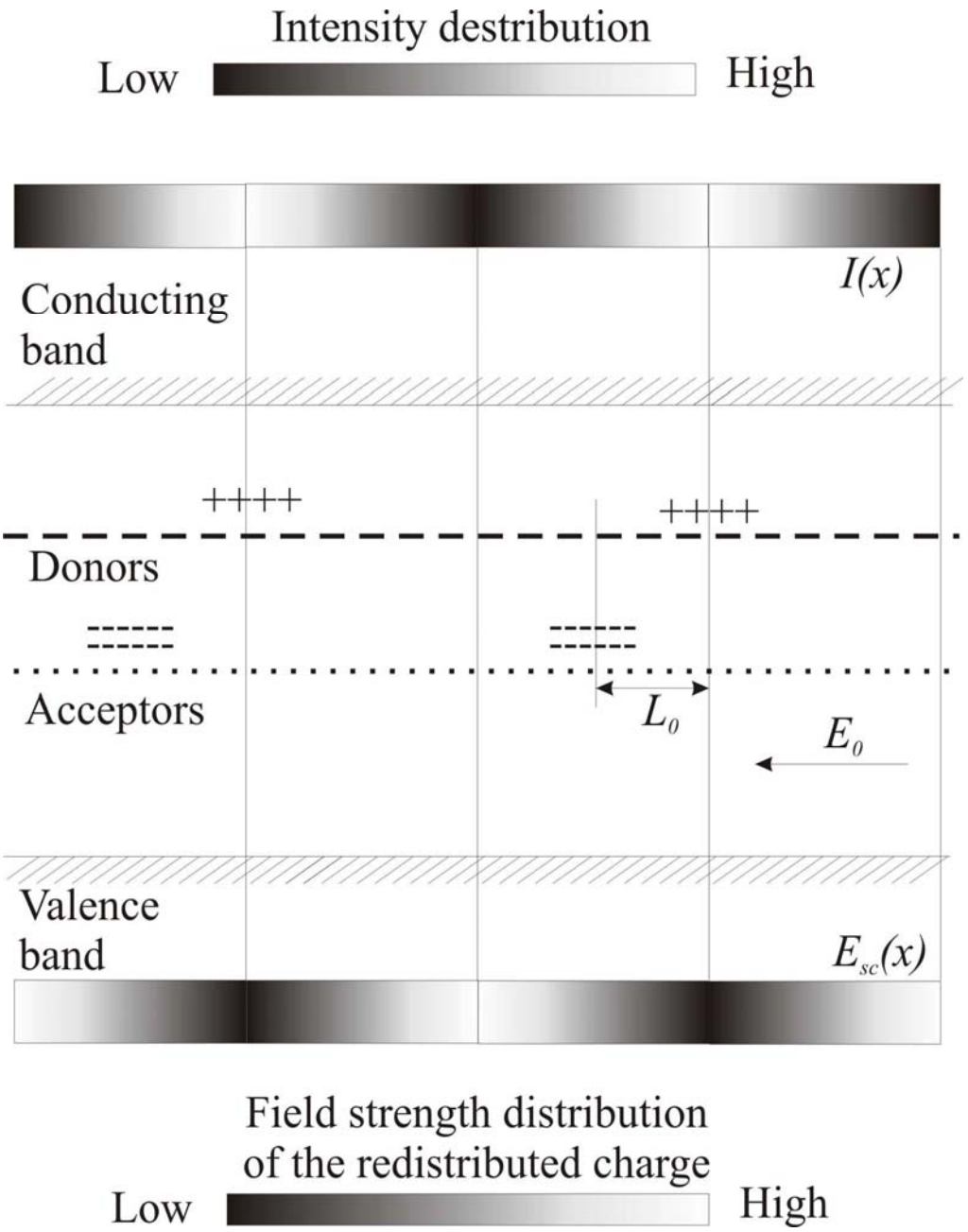

Fig. 2.10: Drift mechanism of the charge redistribution

In this case the field distribution is in phase with the intensity light distribution.

In the case of long-length drifts $K \cdot L_0 >> 1$ no negative-charge grating $\rho^-(x)$ is formed as the electrons have enough time to be uniformly distributed across the crystal. The remaining "grating" of positive-charge "$\rho^+(x) + \rho_0$" is responsible for the $\frac{\pi}{2}$ shift of the field E_{sc} within the crystal with respect to the intensity distribution.

A maximum saturation field created according to the drift mechanism corresponds to a minimal value of two donor and acceptor densities $N_{min} = \min\{N_D, N_A\}$, being equal to

$$E_q = \frac{e \cdot N_{\min}}{\varepsilon \cdot \varepsilon_0 \cdot K}. \tag{2.49}$$

The drift current is determined by the expression

$$\vec{j}_{drift} = e \cdot \mu \cdot n_{fcc} \cdot \vec{E}, \tag{2.50}$$

with n_{fcc} − free carrier concentration. The field $\vec{E} = \vec{E}_{sc} + \vec{E}_0 + \vec{E}_{pyro}$ is a sum over the redistributed charge field E_{sc}, external field E_0, and pyroelectric field

$$\vec{E}_{pyro} = -\frac{1}{\varepsilon \cdot \varepsilon_0} \cdot \frac{\partial P_S}{\partial T} \cdot \Delta T \cdot \vec{e}_S, \tag{2.51}$$

where ΔT − temperature variations in the medium subjected to high-intensity illumination, P_S − spontaneous polarization, and $\vec{e}_S$ unit vector for spontaneous polarization. The space charge field $\vec{E}_{sc}$ and pyroelectric field $\vec{E}_{pyro}$ are spatially modulated, whereas the external field $\vec{E}_0$ is considered to be homogeneous within the crystal.

2.4.3 Photovoltaic mechanism

Photocurrents in electro-optical crystals may be produced even without an applied electric field. Photoelectrons are excited to the conduction band in the direction of the polarization axis, generating a photovoltaic current

$$j_{ph_i} = \beta_{ijk} \cdot E_j \cdot E_k^*, \tag{2.52}$$

where E_j and E_k − components of an electromagnetic light wave, * denotes phase conjugation, and β_{ijk} − third-rank tensor ($\beta_{ijk} = \beta_{ijk}^*$) [55]. As a rule, the one-dimensional photovoltaic effect is measured along one of the axes, and we have

$$j_{ph} = -\beta_{333} \cdot E_3 \cdot E_3^* = -\beta_{333} \cdot I = -k \cdot \alpha \cdot I, \tag{2.52}$$

where k − absorption factor for the light polarized in the x_3-direction, α − constant factor characterizing the crystal and doping elements.

There are several similar explanations for the photovoltaic currents considering the wave functions and orientations of electronic orbitals around excited and unexcited ions of the crystal lattice.

But we may conclude that atoms in the lattice may be shifted along a particular axis that is specified during the growth of a crystal when an external field is applied. Due to such a shift, the effect of an external field is compensated during heating. And the grating becomes fixed as the crystal chills. Because of this, a field created within the crystal subsequently initiates the photovoltaic effect.

The photovoltaic effect is observed not only for light illumination but also with X-ray irradiation enabling applications in medical diagnostics. It should be noted that the photovoltaic effect is responsible for interactions of orthogonally polarized waves in photorefractive crystals.

In conclusion, the charge redistribution induced by the photovoltaic mechanism at small light modulation depths $m << 1$ may formally be represented as electron drift in a virtual external field and, as a consequence, the drift mechanism in the external field can be actually equivalent to the photovoltaic one.

2.5 Main photo-induced processes taking place in photorefractive crystals of the sillenite group

In this chapter we give a brief summary of photo-induced processes taking place in the studied $Bi_{12}TiO_{20}$ crystal (similare properties have all representatives of the sillenite group BTO, BSO, BGO). A nominally pure BTO crystal has an electronic conductance or n-type conductivity. For processes with short lifetimes one can use a one-level model. But for long-lived processes one has to use two-level model. The spectral and dynamical properties may differ obviously and even unpredictable. This will be shown in chapter 4 in details. The photorefractive effect is the response on the low-intensity irradiation with a modulation of the refractive index due to the electro-optical effect. The photochromic effect is the response on high-intensity radiation due to the modulation of the optical absorption in a certain spectral range. The main non-induced absorption takes place due to photoionization of deep impurities and direct electron transitions from the valence band (VB) to the conducting band (CB). The photo-induced absorption is realized due to the photoionization and photoneutralization of shallow and deep long-lived traps (chapter 4). The main spatial charge transport mechanisms are diffusion and drift. Photovoltaic mechanisms are not adequately detectable for the crystals

of the sillenite group in comparison with previous effects. Diffusion takes place always. Drift is taken into account only in the case of an external electrical field.

Chapter 3

Photorefractive crystals of the sillenite group

Our work is aimed on the investigation of photo-induced processes in photorefractive $Bi_{12}TiO_{20}$ crystals as one of the typical representatives of the sillenite group. Most of the properties are similar for the whole group

This kind of crystals is a popular medium due to response, high symmetry and crystal growth technique. Sillenites are promising structures for doping. Impurities can change the optical properties significantly. This makes the crystals flexible for applications.

In Chapter 3.1 the common chemical and crystalline properties of sillenite crystals are shown. Chapter 3.2 is devoted to the optical characteristics of the crystal $Bi_{12}TiO_{20}$ and compares them with other crystals.

3.1 Sillenites

Sillenites are one of the promising groups of photorefractive materials. These materials are named in honor of the Swedish chemist Lars Gunnar Sillen, who in 1937 studied the polymorphism of bismuth sesquioxide Bi_2O_3, and discovered the formation of abody-centered cubic (*bcc*) phase by the fusion of Bi_2O_3 in porcelain, or with the oxides Al_2O_3 or Fe_2O_3 [56].The obtained phase was isomorphous in the synthetic compound $Bi_{24}Si_2O_{40}$, which represents a large class of materials, later called sillenites, with the theoretical composition $Bi_{12}MO_{20}$.

The *bcc* cell with lattice constants in the range 10.10 - 10.26 Å is characteristic for a large group of compounds formed between the metastable γ-phase of Bi_2O_3 and various oxides. Both stable and metastable compounds have been reported [57, 58]. The oxides of quadrivalent elements MO_2 (M = Si, Ge, Ti) give stable phases approximated by the formula $Bi_{12}MO_{20}$, where the Bi : M ratio closely approaches 12 : 1. The formula $Bi_{12}MO_{20}$ describes the ideal or stoichiometric species in which all particular cationic and anionic sites in the *bcc* cell are fully occupied.

An ideal sillenite structure consists of two main fragments. Each M^{4+} atom is surrounded by four oxygen atoms forming perfect tetrahedra at the eight corners and center of a cube, with the oxygen atoms on the cube diagonals. On the other hand, each Bi atom is surrounded by seven oxygen atoms. In principle, this arrangement can be considered as octahedral coordination with the oxygen atom at the corner replaced by two atoms at higher distances [59, 60], or as distorted tetragonal pyramid whose base is formed by four oxygen atoms while the fifth oxygen atom occupies an axial vertex [61]. Two $[BiO_x]$ polyhedra sharing one oxygen-oxygen edge form the frame work of the sillenite structure. The unit cell can be written as $Bi_{24}M_2{}^{4+}O_{40}$ or $Bi_{24}[M^{4+}O_4]_2O_{32}$. $Bi_{12}SiO_{20}$, $Bi_{12}GeO_{20}$ and $Bi_{12}TiO_{20}$. It has stable *bcc* sillenite structure very close to the ideal. Theoretically all particular cationic and anionic sites in the *bcc* cell are fully occupied. In the real structure of sillenites, however, the occupancy factor q_M of the M cations in tetrahedral positions is less than unity, e.g., q_{Ge} = 0.87(2) for $Bi_{12}GeO_{20}$ (BGO), q_{Si} = 0.87(8) for BSO [62]. The vacancies in the cationic (Bi^{3+} and M^{4+}) and anionic (O^{2-}) sublattices create the acceptor and donor levels in the energy gap that are mainly responsible for the photorefractive properties of sillenites [63]. The vacancies present in the sillenite structure permit to add various elements by doping and therefore

change the electronic band structure and optical (photorefractive) properties of sillenites in the desirable direction.

Another, much more promising method of carrying out an intentional correction of optical properties of sillenites exists. It is known that the sillenite structure can fit various M atoms with a valence other than four, because the tetrahedron of oxygen atoms surrounding the M atom can expand or contract without a major effect on the remaining atomic arrangement [62].

There are two different descriptions of the resulting sillenite structure. A structural model in which the valence of the M cation or the effective valence of the isomorphous cationic mixture at the M site is always equal to four is discussed in [60, 64 - 66]. Based on the data of X-ray analysis, it was assumed that the partial oxidation of bismuth (3+) into the (5+) state is necessary to stabilize the sillenite phases of the compositions $Bi_{12}[M^{3+}_{1/2}M^{5+}_{1/2}]O_{20}$ and $Bi_{12}[M^{2+}_{1/3}M^{5+}_{2/3}]O_{20}$. Where M^{2+} = Zn, M^{3+} = Fe, Ca, M^{5+} = P, As, Bi. The structure of these phases can be derived from $Bi_{12}M^{4+}O_{20}$ by the substitution pair

$$2M^{4+} = M^{3+} + M^{5+} \,/\, 3M^{4+} = M^{2+} + 2M^{5+}. \qquad (3.1)$$

The chemical formulae of these compounds can be written as $Bi_{24}(M^{3+}M^{5+})O_{40}$ and $Bi_{36}(M^{2+}M^{5+})O_{60}$ or $Bi_{24}[M^{3+}O_4][M^{5+}O_4]O_{32}$ and $Bi_{36}[M^{2+}O_4][M^{5+}O_4]_2O_{48}$, respectively, where M^{n+} are the cations in a valence state other than four that fractionally occupied tetrahedral sites in the *bcc* sillenite structure. The $[M^{n+}O_4]$ is regular, and no oxygen deficiency was supposed to exist in the structure.

Another proposed model of the sillenite structure is based on neutron diffraction data [61]. According to this model all Bi atoms at tetrahedral positions in the sillenite structure are always trivalent. The presence of a large and asymmetric Bi^{3+} cation with $6s^2$ electron pair in the tetrahedral voids arises from the loss of one oxygen vertex in those tetrahedra populated by Bi atoms. This means that there are two types of the sillenite structure: regular and "distorted" [63]. The Bi^{3+} cations are populated in the distorted oxygen polyhedra. The space available to host the ion $6s^2$ electron pair of the Bi^{3+} ion is provided as a result of the oxygen vacancy [61]. The Bi^{3+} ion is displaced towards the oxygen vacancy, increasing the distances between the Bi atom and the other three neighboring oxygen atoms up to allowed values. The chemical formulae of these compounds can be written as $Bi_{24}(M^{3+}Bi^{3+})O_{39}$ and $Bi_{36}(M^{2+}Bi_2{}^{3+})O_{58}$ respectively. Obtained results have been confirmed for some sillenites containing M^{n+} cations in the valence state other four [61, 67, 68].

The Bi – O distances in some isostructural sillenites are compared in [62]. It has been shown that the Bi – O network in these compounds remains nearly unchanged. The increase in the M – O distance through the series BSO, BGO, BTO, causes a corresponding decrease in the Bi – O(3) distance (from 2.647 Å in BSO to 2.606 Å in BTO) [69].

Compared with four-valence sillenites (BGO, BSO, BTO), there are many more possibilities to influence the electronic band structure and thus the photorefractive properties of this group of sillenites.

As mentioned above, sillenites containing M cations in the valence state other than four were mainly studied crystallographically. The information concerning the phase diagrams of the binary systems Bi_2O_3-M_xO_y and the compositions of the obtained compounds are important. Only three compounds with a sillenite structure – $Bi_{12}GeO_{20}$, $Bi_{12}SiO_{20}$ and $Bi_{12}TiO_{20}$ – have been grown as large single crystals of high optical quality. All other sillenites have been obtained either as polycrystalline ceramics using solid-state synthesis or as small single crystals with an optical quality insufficient for any optical investigations nor, of course, practical application in any devices. Thus, it is possible to conclude that these sillenites are practically unknown because of the chemical-technological problems of their production.

As mentioned above, bismuth oxide, Bi_2O_3, can be stabilized in the metastable cubic γ-form by the addition of small amounts of oxides [58]. Depending on the melting characteristics of the obtained compounds, various techniques of the crystal growth can be used. Some compounds (e.g., those formed by the addition of GeO_2 and SiO_2) melt congruently and may be pulled by Czochralski technique. Others, formed by the addition of TiO_2 and Ga_2O_3, melt incongruently, and the hydrothermal technique or high temperature solutions should be used to crystallize these compounds. So, two principally different methods can be used for single crystals of sillenites: hydrothermal synthesis and crystallization from the melts (Czochralski method, e.g.).

Most of the crystals studied have been grown from stoichiometric or nonstoichiometric melts. The most rapid technique of crystal growth is the Czochralski method. Congruently melting $Bi_{12}GeO_{20}$ and $Bi_{12}SiO_{20}$ single crystals were first grown by this method in 1966 in the Bell Telephone Laboratories [70]. In later years significant efforts have been made to improve the optical quality and size of the grown BGO and BSO crystals [71-75]. Inductive (RF) heating and the resistance furnaces are usually used for growing crystals with a sillenite structure.

It was shown that the composition of the crystal depended on the melt composition and the oxygen pressure, which are the reason that a nonstoichiometric crystal will have native defects, such as substitutions, interstitials and vacancies [76, 77]. These defects were originally proposed as the source of the absorption shoulder that is the origin of the relatively large photocurrent in the visible spectrum [78].

The intentional variation of the optical properties of sillenites can be caused by doping. Doped sillenite crystals are obtained by adding small amounts of the desired oxides to the melt. Some impurities (Al, P, Ga and etc.) are introduced in concentrations of about several percent to improve the crystal transparency. Among the properties they can affect are crystal stoichiometry and photocarrier sign. Another group of impurities, mainly transition-metal and rare earth ions, can be introduced in concentrations ranging from 1-1000 ppm and various optical, EPR and spectroscopic studies involving this have been published. Studied impurities, their valence states and investigation techniques are reviewed in [79]. Also the scanning electron microscopy gives the possibility to check this. A typical spectrum of the BTO crystal is shown Fig. 3.1.

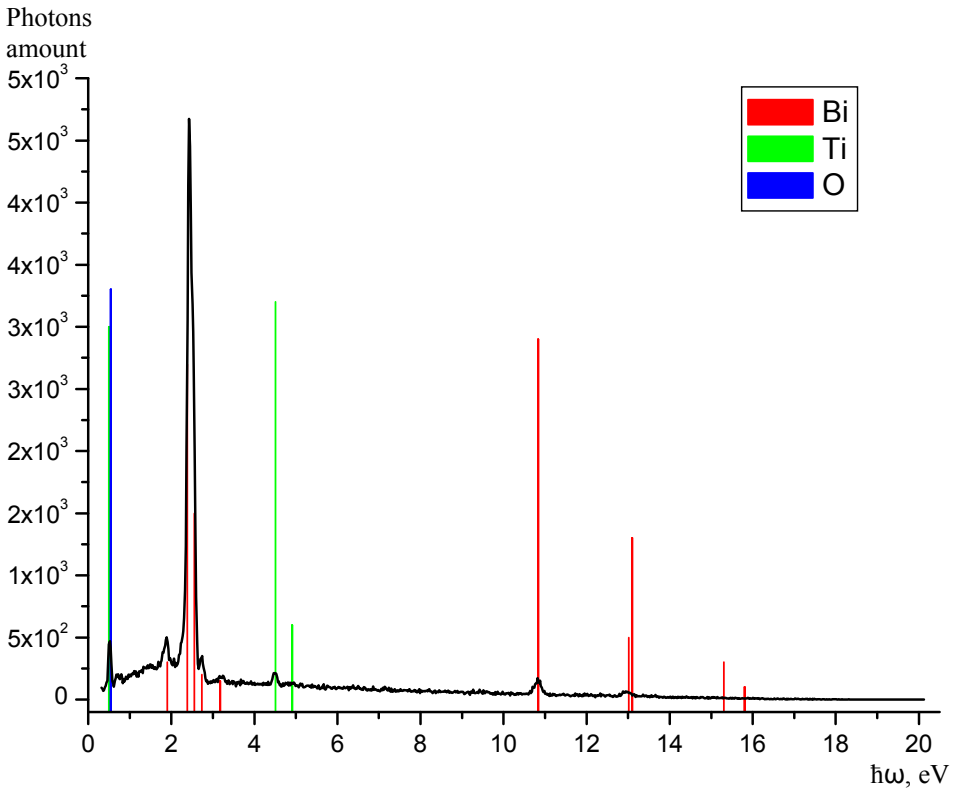

Fig. 3.1.Spectrum of the light emission under incident scanning electron beam detected by the scanning electron microscope: Leo1455VP “Carl-Zeiss”

The comparison of the emission spectrum with the characteristic lines of elements (coloured lines) shows chemical elements in the crystal. The quantitative analysis of the spectrum confirmed the purity of the observed crystal with an accuracy of 99.9%.

3.2 Properties of sillenites

In the band transport model of photorefractivity there are at least eight parameters of the material controlling the formation of the refractive index gratings when the material is illuminated with an optical interference pattern. These parameters are:

ε – low frequency dielectric constant

n_b – background refractive index

r_{eff} – effective electro-optic coefficient

s – cross-section for photoionization

N_D – number density of dopants

N_A – number density of acceptors compensating for the number density of ionized dopants N_D^+ in the dark

μ – mobility

γ_R – coefficient for electron recombination in ionized traps N_D^+.

The first three parameters are intrinsic properties of photorefractive crystals, which are not amenable to change in well-poled crystals and are not expected to vary significantly from one crystal sample to another. The remaining five parameters depend on the impurity and/or the defect content of the crystal, and thus may be adjusted by either doping during crystal growth, oxidation and reduction treatment, radiation, or in-diffusion. A detailed description of various experimental techniques for determining photorefractive parameters is given in [80]. Some ways of the materials parameters optimization for better performance are shown in [81]. Basic physicochemical properties and the main photorefractive parameters of sillenites are summarized in [79, 82, 83] and presented in table 1.

Parameter	**BSO**	**BGO**	**BTO**
Chemical composition	$Bi_{12}SiO_{20}$	$Bi_{12}GeO_{20}$	$Bi_{12}TiO_{20}$
Melting point. ˚C	9[illegible]5 congruent	9[illegible]5 congruent	8[illegible]5 incongruent
Unit cell Lattice constant, Å	*bcc* 10.1043	*bcc* 10.1455	*bcc* 10.18[illegible]
Density, g/cm ^{3}	9[illegible]9	9[illegible]2	9[illegible]6
Dielectric constant	56	3[illegible]7	47
Refractive index at 4[illegible]nm at 514 nm at 633 nm	 2.650 2.615 2.530	 2.650 2.615 2.530	 2.68[illegible] 2.650 2.563
Rotatory power, ˚mm^{-1} at 4[illegible]nm at 514 nm at 633 nm	 44 38 21	 45 38 22	 12.8 10.8 6.2
Optical bandgap, eV	3.25	3.25	3.1
Electro-optic coef. r_{41}, m/V	4.1 x 10^{-12}	3.8[illegible] x 10^{-12}	5.17[illegible] x 10^{-12}
Piezoelectric constant, C/N	4.05 x 10^{11}	3.39[illegible] x 10^{11}	4.8[illegible] x 10^{11}

Table 1. Physicochemical properties and main photorefractive parameters of sillenites

For the crystal BTO the tensor matrix of the electro-optic coefficients looks like

$$\hat{r} = \begin{pmatrix} 0 & 0 & 0 \\ 0 & 0 & 0 \\ 0 & 0 & 0 \\ r_{41} & 0 & 0 \\ 0 & r_{41} & 0 \\ 0 & 0 & r_{41} \end{pmatrix}. \qquad (3.2)$$

The half-wave voltage is $U_{\lambda/2}=\lambda/2\, n^3 r$ = 3.3 kV. Pure BTO crystals have a dominant electron photoconductivity in the blue-green. The charge carrier mobility under voltage is $\mu_\tau = 2.4\cdot10^{-8}$ cm^2/V. The mean free length L_D = 0.25 μm. The photovoltaic fields E_G in BTO do not exceed $2\cdot10^{-2}$ V/cm (λ = 4[illegible]m). The maximum diffraction effici ency was obtained in the (110)-cut samples with the $[1\,\bar{1}\,1]$ axis parallel to the H-polarized light beams. The efficiency of up to 30% was obtained for the diffusion grating reco rded by the light beams entering the crystal through adjacent orthogonal faces [14]. Because of the strong optical absorption in the blue-green, the working range of BTO is yellow-red.

Chapter 4

Investigation of long-lived centers in photorefractive $Bi_{12}TiO_{20}$ (BTO) crystals

The charge redistribution in donor and trapping centers should result in a reversible change of the properties of the crystal. The easiest way to observe the redistribution of the charge carriers between initially empty long-lived traps is the induced absorption dynamic measurements. As a rule, the photo-induced light absorption in crystals of sillenites is studied with their continuous illumination by broad-band lamps [84-90], and also by monochromatic lasers [41, 91-93] or quasi-monochromatic semiconductor light-emitting diodes [92, 93]. In a study [93] of the photo-induced absorption dynamics in calcium-doped crystals of bismuth titanate ($Bi_{12}TiO_{20}$:Ca) it has been found that, upon gradual irradiation of the crystals by quasi-monochromatic light from the red (660 nm) and green (525 nm) spectral regions, there is an interaction between illumination at one wavelength and absorption of radiation at another one.

In this chapter we are discussing long-lived photo-induced phenomena in a nominally pure photorefractive crystal $Bi_{12}TiO_{20}$ (BTO). In chapter 4.1 the initial and photo-induced light absorption is investigated. One calculates calculate theoretically the spectral properties of the long-lived centers (traps). Chapter 4.2 is devoted to the relaxation investigation for the experimental proof of the theoretical model and the spectral characteristics of the traps. In chapter 4.3 we present an experimental study of dynamic processes of the electron relaxation

to the deep traps located in the forbidden band (and responsible for the photorefractive effect) with the method of four-wave mixing (FWM). FMW gives the opportunity for direct measurements of the dynamical characteristics. In chapter 4.4 the influence of the multi-wavelength low intensity cw irradiation is investigated. Experimental methods to influence on the behavior of induced absorption are shown. Chapter 4.5 is devoted to the absorption induced by different methods. We compare the irradiations with ns and ps pulses. In chapter 4.6 the crystals $Bi_{12}TiO_{20}$ and $Bi_{12}SiO_{20}$ (BSO) are compared. In chapter 4.7 the results are summarized.

4.1 Excitation of the photo-induced absorption

4.1.1 Experimental setup

The investigation of the photo-induced absorption in BTO was carried out for a nominally pure $Bi_{12}TiO_{20}$ crystal, which was grown from a high-temperature solution by the Czochralski method. The crystal has the cubic symmetry 23 like the other members of the sillenite family. The light radiation propagated along the [100] crystallographic axis. The (100) faces with the transverse dimensions 7 x 7 mm^2 were polished with optical quality. The thickness of the crystal with regard to the dimension [100] was 2.8 mm. For inducing of the absorption a pulse laser at 532 nm (second harmonic of Nd:YAG) (Fig. 4.1a) was applied. The spatially homogeneous part of the laser beam was cut out by an aperture of 2.5 mm. The pulse duration was 30-50 ns, the repetition rate was 10 Hz, and the average pulse energy after passing through the diaphragm was 0.5 mJ. The average power of the pulse was 0.13 MW. So, the average intensity of the laser radiation incident on the surface of the crystal during the pulse was 2 MW/cm^2. The integral average intensity of the laser radiation incident on the crystal during exposition was 110 mW/cm^2. The polarization of the laser light was located in the plane (100) and parallel to [011].

The absorption of the crystal was measured with a spectrophotometer based on a CCD line array with 2048 pixels. The dispersion element was a fixed diffraction grating with 600 lines/mm yielding a resolution < 1 nm. The probe beam consisted of light emitted by a Xe and halogen lamp (Xe/HL) simultaneously with a total intensity below 0.8 mW/cm^2 in the whole spectral range. Five seconds after the irradiation with the laser (532 nm) the spectrophotometer and the Xe/HL were switched on, and the absorption was measured in the range 480 – 1100 nm. The integration time of the CCD array was 11 ms, which gives a time

of measurement of 0.11 s for 10 single measurements. After each cycle of measurement the laser was turned on for 5 s and the irradiation continued. The relaxation of the induced absorption was found to be constant in the darkness and at fixed room temperature. Within the VIS a long-lived photo-induced absorption appears which could be measured using the setup shown in Fig. 1b. In this case the laser beam was focused by a micro objective into a spot of 0.2 mm diameter.

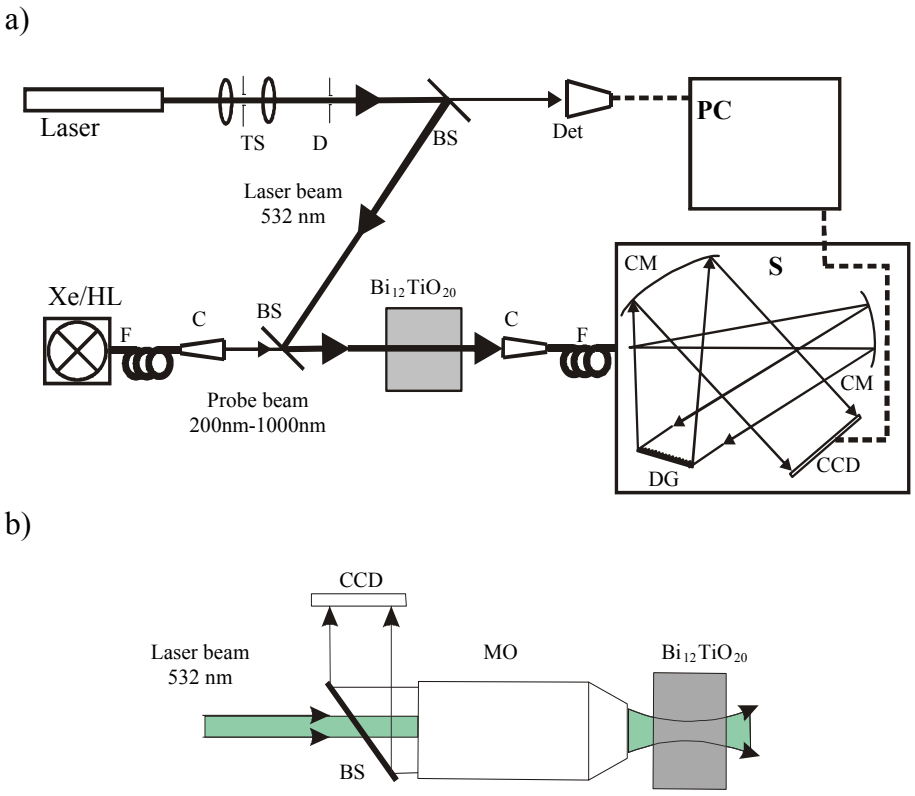

Fig. 4.1. a) Scheme of the experimental setup for the generation and measuring of the photo-induced absorption. Laser – Nd:YAG (532 nm) , TS – telescopic system, D – diaphragm, BS – beam splitter, Xe/HL – Xe/halogen lamp (200 nm-1000 nm), F - fiber optics, C – collimator, S – spectrophotometer, CM – collimating mirror, DG – diffraction grating, CCD – CCD linear array "Sony 2048", Det – photo detector, PC – computer. b) Scheme of the experimental setup for visualization of the photo-induced absorption in the VIS. MO – micro objective, CCD – CCD matrix 1400x1400 pixel.

4.1.2 Experimentally observed induced absorption

The spectra of the photo-induced absorption against the exposition energy are shown in Fig. 4.2. A change of absorption became detectable already after 1 minute of exposition (total energy per square centimeter - ca. 7 J).

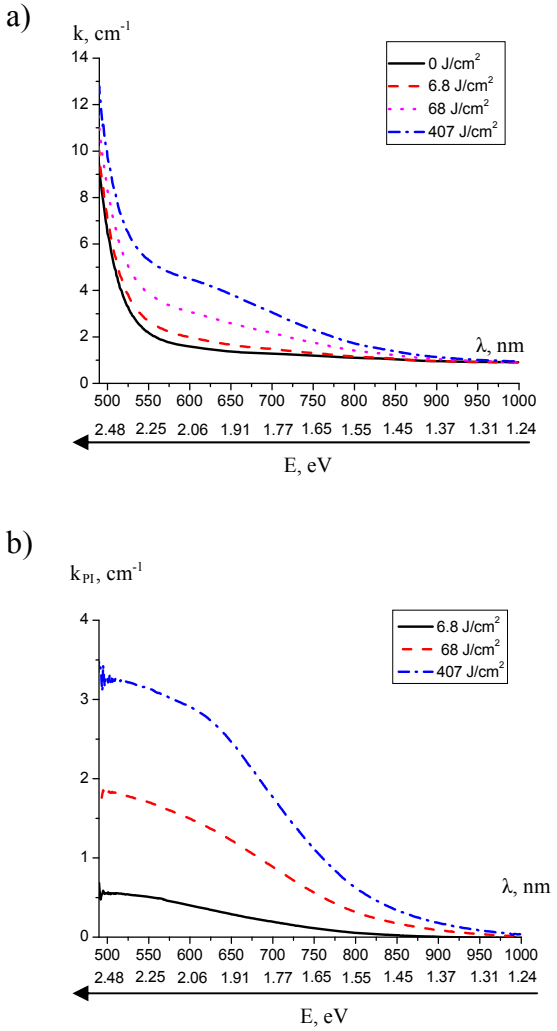

Fig. 4.2. a) Absorption spectrum of BTO for different values of the total exposition (J/cm_2). k is the absorption coefficient. b) Dependence of the photo-induced absorption k_{PI} (difference between integral absorption k and initial absorption without exposition k_0). The pulse laser had an average intensity of 110 mW/cm^2 at 532 nm.

One can observe a strong increasing of the absorption in the range up to 900 nm during the light exposition. This effect can be explained by long-lived centers with energy levels in the forbidden band that are caused by impurities and defects in the bulk of the crystal [18]. These centers can be denoted as intermediate-level traps (IT) [94, 95] (Fig. 4.3).

Under normal conditions at room temperature and without pre-exposure the absorption is coursed only by the excitation of charges from deep levels (deep traps DT) and from the valence band (VB) to the conducting band (CB) [96]. The DT can be attributed to the spreading of the VB due to impurities and defects. The population of the DT is due e. g. to a stochastic excitation of charges from the VB and is much weaker than the population of the VB. The spectrum of the non-photo-induced absorption (Fig. 4.2a) shows that the upper level of the DT lays at ca. 2.3 eV (ca. 540 nm) below the CB. The width of the forbidden band of

$Bi_{12}TiO_{20}$ is experimentally detected in measurements of the transmission of the light through thin samples (thickness is 30 μm) of pure crystals of the sillenite group BGO, BSO, BTO (Fig. 4.4). Measurement errors are less than 5%. The width of the forbidden band of $Bi_{12}TiO_{20}$ crystals is approximately 3.1 eV (ca. 400 nm) [10].

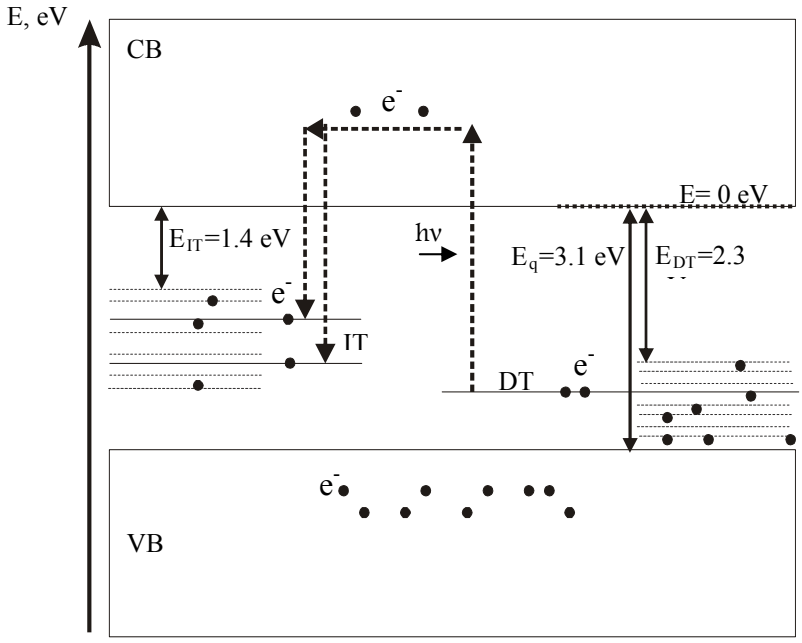

Fig. 4.3. Schematic illustration of the photo-induced absorption in BTO. The long-lived intermediate traps (IT) are located in the forbidden band and are responsible for the stronger increasing of the photo-induced absorption in the VIS and near IR spectral ranges. E_q –width of the forbidden band, E_{DT} –depth of the upper border of the deep levels, E_{IT} - depth of the upper border of the levels of the long-lived centers (intermediate-level traps).

In our case for an irradiation at 532 nm the excitation of electrons basically takes place from the DT to the CB. If the charges are excited into the CB they can recombine back to the VB and DT as well as to the long-lived IT. The lifetime of charges in the CB is relatively short because of the short recombination time constant τ_r, which is below 100 ns [17, 44]. The charges of the long-lived levels can be excited again into the CB by photons with lower energy. A growth of the photo-induced absorption k_{PI} is observed at wavelengths below 900 nm (Fig. 4.2b). The photo-induced absorption k_{PI} is connected with the excitation of charges from the IT to the CB. It will be shown below that there are two different long-lived levels in the system of IT. The upper level border of the long-lived levels lays at ca. 1.4 eV (900 nm) below the CB (Fig. 4.2b).

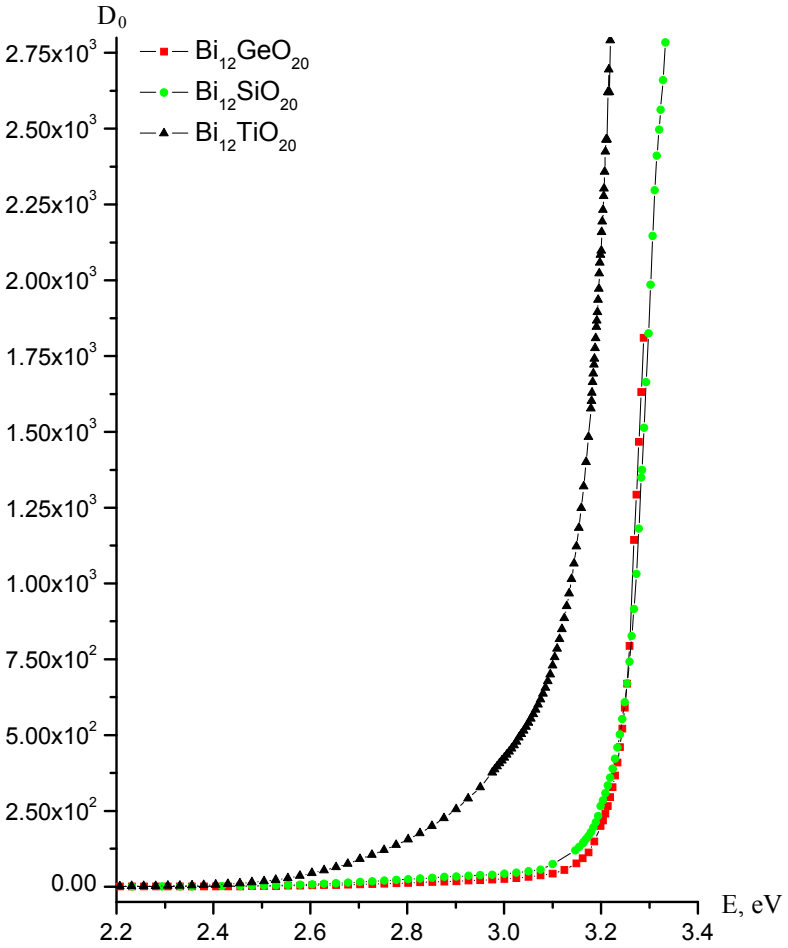

Fig. 4.4. Spectrum of the fundamental absorption of the sillenite group crystals: $Bi_{12}TiO_{20}$, $Bi_{12}SiO_{20}$, $Bi_{12}GeO_{20}$. D_0 is the optical density of the crystals with a thickness 30μm.

4.1.3 Theoretically approximated induced absorption

The spectrum of the induced changes in absorption may be derived as the difference $k_{PI}(\lambda,t) = k(\lambda,t) - k(\lambda,0)$. k is the absorption coefficient, t is the time of exposition. For the theoretical consideration it is convenient to go to the relationship between the induced changes in absorption and the energy of a single photon $E = \hbar\omega$ expressed in eV. The experimental results of $k_{PI}(E,t)$ are represented by points in Fig. 4.5. The measurement error is less than 5%.

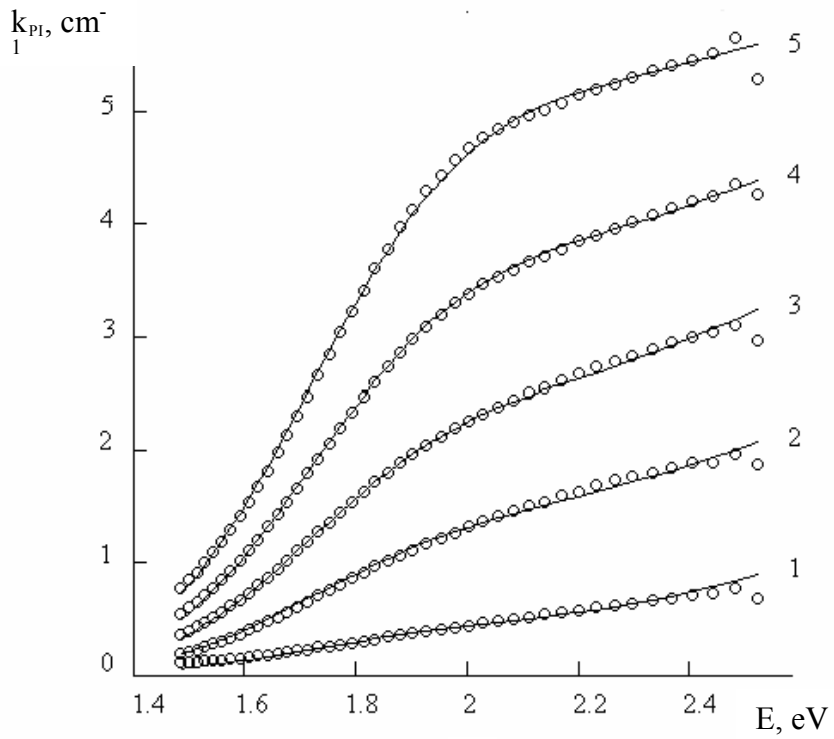

Fig. 4.5. Spectral dependences of the additional absorption in a BTO crystal subjected to illumination by laser pulses at values of the total exposition (J/cm^2): 14 J/cm^2 (1), 70 J/cm^2 (2), 140 J/cm^2 (3), 420 J/cm^2 (4), 1260 J/cm^2 (5). Points – experiment, solid curves – theory

As shown in Fig. 4.5, the absorption is growing with the photon energy reaching their maximum values ~5.5 cm^{-1} at $E = 2.52$ eV (for $\lambda = 492$ nm).

Quantitative models of the photo-induced light absorption in crystals of sillenites are based on the hypothesis that the defect centers with differing photoionization cross-sections are recharged [41, 97, 98]. It is assumed that the electrons photoexcited from deep donor centers into the conduction band fill the traps, leading to changes in optical absorption. In some works [41, 98] the traps are supposed to be shallow, and their depletion, as the electrons are thermally excited into the conduction band, provides relaxation of the induced changes in absorption under dark conditions. But in [97] it is demonstrated that the localization of the energy levels associated with these traps in the bandgap of a $Bi_{12}TiO_{20}$:Ca crystal is deeper than 1.43 eV with respect to the conduction band. The corresponding value for an undoped BTO crystal may be estimated from the data of [99] as 1.17 eV.

The form of an absorption spectrum for the photoexcitation by photons with the energy $\hbar\omega$ from the deep defect center that is characterized by a discrete local energy level within the bandgap and ionization energy E_I may be approximated as follows [42]

$$k_{\delta}(\hbar\omega, E_I) = B_{EI}\frac{\sqrt{\hbar\omega/E_I - 1}}{\left(\hbar\omega/E_I\right)^3}, \tag{4.1}$$

where the factor $B_{EI} = SN_{EI}$ is proportional to the concentration N_{EI} of these centers and to their photoionization cross-section S. It is seen from Fig. 4.5 that the spectral dependence of the induced absorption in a BTO crystal doesn't correspond with the equation (4.1). This may be caused by different factors. First, by the presence of several types of traps with different energies and photoionization cross-sections. Second, a highly imperfect structure of bismuth titanate crystals [85, 90] should result in significant random fluctuations of the defect concentration with associated fluctuations of the ionization potential. As this takes place, local levels of the defects are overlapping, and the energy distribution density for their concentrations within the bandgap may be represented in the form of a smooth function $N(E_I)$. This makes it possible to introduce a factor $B(E_I)dE_I = SN(E_I)dE_I$ determining the light absorption associated with the ionization energy interval dE_I. The total absorption factor for radiation at the frequency ω may be determined in the integral form by

$$k(\hbar\omega) = \int_0^{\hbar\omega} SN(E_I)\frac{\sqrt{\hbar\omega/E_I - 1}}{\left(\hbar\omega/E_I\right)^3}\frac{1}{1+\exp\left[\left(E_F - E_I\right)/k_BT\right]}dE_I, \tag{4.2}$$

where the energy E_F equals the distance of the Fermi level to the conduction band, k_B – Boltzmann constant, and T – absolute temperature.

Let us assume the normal energy distribution law for the concentrations $N_n(E_I)$ of the *n*-type traps. As it is claimed that the parameters of each distribution remain constant during filling or depletion of the traps, the functional relationship $B(E_I, t)$ between the ionization energy and time may be represented in the following form

$$B(E_I, t) = \sum_n b_n(t)\exp\left[-\frac{\left(E_n - E_I\right)^2}{\Delta E_n^2}\right], \tag{4.3}$$

where the function $b_n(t)$ allows for the time dependence of the *n*-type trap filling by the electrons.

The results obtained by approximation of the experimental dependences for the induced changes in absorption $k_{PI}(E,t)$ on the basis of relations, taking account of two centers with the average ionization energies $E_1 = 1.597 \pm 0.092$ eV and $E_2 = 2.566 \pm 0.028$ eV, are demonstrated by solid curves in Fig. 4.5. The values for the distribution half-width

and Fermi level position are $\Delta E_1 = 0.277 \pm 0.018$ eV, $\Delta E_2 = 0.580 \pm 0.031$ eV and $E_F = 1.027$ eV.

Fig. 4.6 shows the dependences of the approximated parameters $b_1(t)$ and $b_2(t)$ on illumination. The second center, whose energy levels are distributed close to the top of the valence band, is filled by the electrons and reaches saturation at the exposure time $t \sim 900$ s (210 J/cm^2). The first center occupation is far from saturation even at $t \sim 3600$ s (1260 J/cm^2).

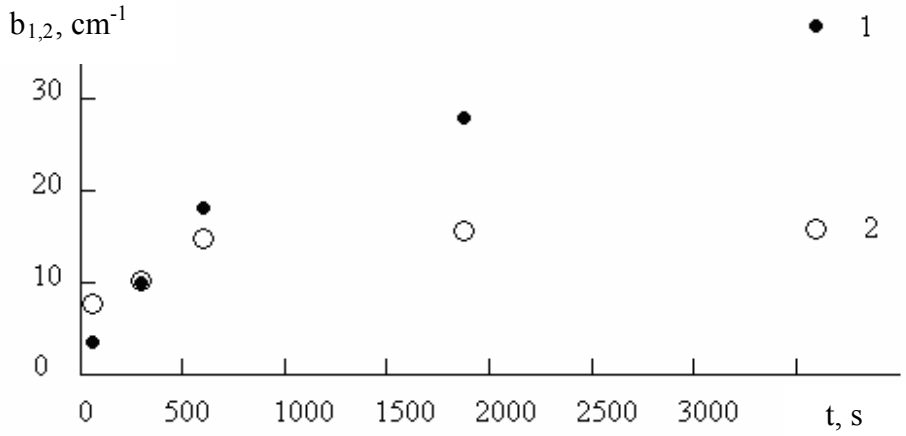

Fig. 4.6. Time profiles of the functions $b_1(t)$ and $b_2(t)$ which characterize the trap filling by electrons at the ionization energies $E_1 = 1.597$ eV (1) and $E_2 = 2.5668$ eV (2) on illumination of the crystal by laser pulses. The pulse laser had an average intensity of 110 mW/cm^2 at 532 nm.

4.2 Relaxation of photo-induced absorption

4.2.1 Experimentally observed relaxation of the photo-induced absorption

The BTO crystal shows slow relaxation characteristics and keeps the absorption induced during the exposition by laser pulses with a relatively high intensity (2 MW/cm^2) for a long time (till 80 hours). E. g. the induced absorption in VIS and its dynamics of relaxation can be seen in Fig. 4.7a. The dependence of the spectrum of the induced absorption in BTO versus the relaxation time is shown in Fig. 4.7b.

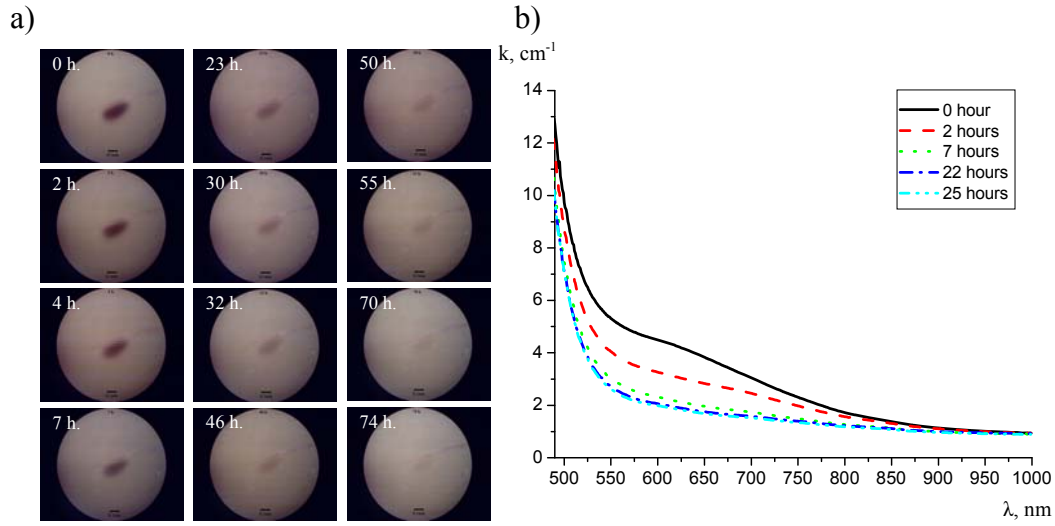

Fig. 4.7. a) View of the crystal with photo-induced absorption in its center. A microscope took the images during the relaxation process. The laser radiation was focused to a spot size of 0.2 mm. b) Absorption spectrum for different relaxation times after laser exposition during 1 hour with an average intensity of 110 mW/cm^2 at the wavelength 532 nm (exposition was approx. 400 J/cm^2). k is the coefficient of absorption.

The absorption coefficient k in the case of the transition between two fixed energy levels is given by

$$k = (n_1 - n_2) \cdot \sigma \approx n_1 \sigma \,, \tag{4.4}$$

where n_1 is the population of the lower level (quantity of the absorption centers), n_2 is the population of the upper level (quantity of the emitting centers), and σ is the cross section of absorption. The approximated equation (4.4) occurs in the case of higher population of the lower level ($n_2 << n_1$).

The population of the long-lived levels decreases as a result of thermal processes in darkness and can be described by

$$n = n_0 e^{-t/\tau} \,, \tag{4.5}$$

where n_0 is the population of the level at the beginning, t is the time, τ is the lifetime of charge carriers on the trap level. Fig. 4.8a shows the temporal development of the coefficient of absorption for different wavelengths during relaxation.

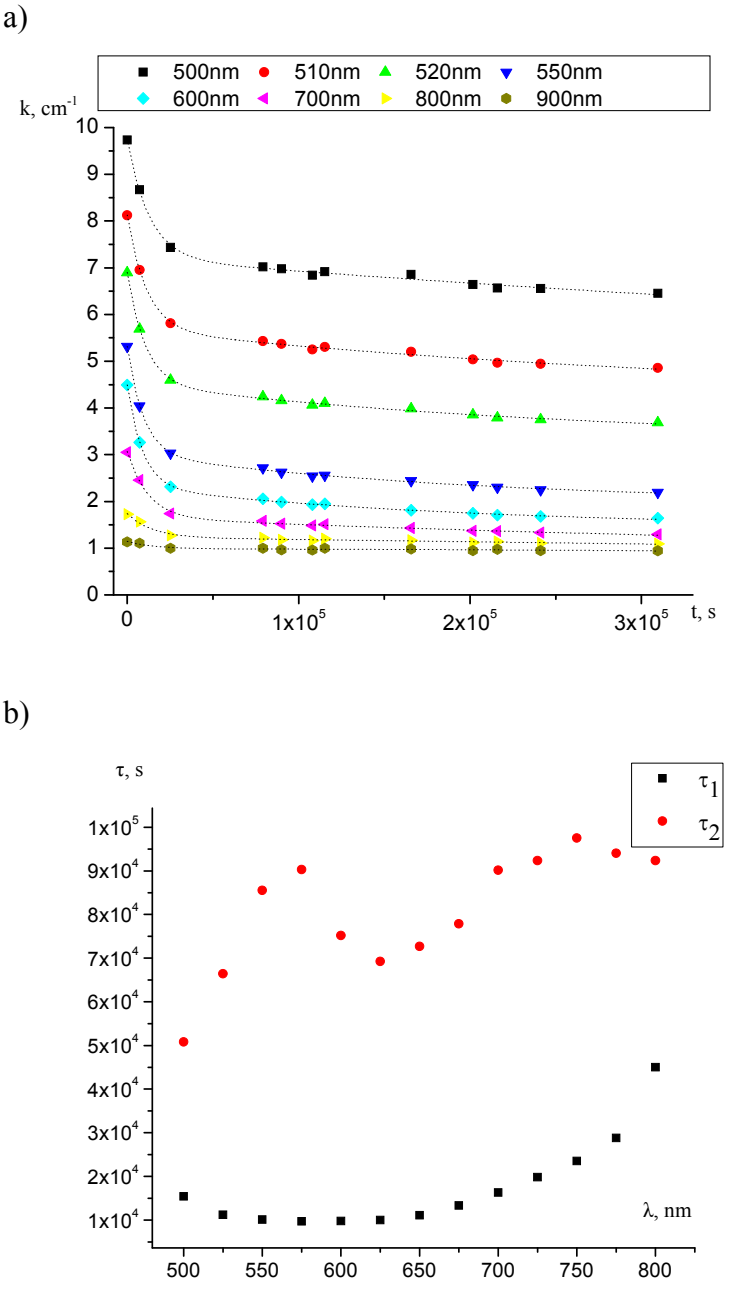

Fig. 4.8. a) Dependence of absorption on the relaxation time for different wavelengths after laser exposition during 1 hour with an average intensity of 110 mW/cm^2 and a wavelength 532 nm. b) Spectral dependence of the lifetimes τ_1 and τ_2 of the long-lived levels. The measurement error is less than 5%.

Analyzing the relaxation dynamics presented in Fig. 4.8a shows that it can be approximated by a double - exponential function (dotted line)

$$k = k_0 + k_1 e^{-t/\tau_1} + k_2 e^{-t/\tau_2}, \qquad (4.6)$$

where k_0, k_1, k_2, τ_1, τ_2 are the mathematical coefficients of approximation. It is possible to find a relationship between the coefficients of approximation and the physical magnitudes: k_0

is the coefficient of absorption without the photo-induced effect, k_1, k_2 are the initial coefficients of absorption for long-lived levels, τ_1, τ_2 are the corresponding lifetimes. There are two relaxation components ($k_1 e^{-t/\tau_1} + k_2 e^{-t/\tau_2}$). Each of them is connected with a specific type of absorption centers. Using the experimental values (Fig. 4.8a) and equation (4.6) the spectral dependences of lifetimes of the long-lived levels can be found (Fig. 4.8b). The two "spectra" of lifetimes for the two kinds of induced long-lived centers can be seen in Fig. 4.8b. In the ideal case the lifetime of the absorption centers has to be constant for the relatively narrow trap's level. In our case the dependences of the lifetimes on the wavelengths are non linear and non monotone, which is in agreement with the stochastic nature of the traps. A random variation of the surrounding of each center yields a broadening of the levels of the traps. Moreover, the variation of the surrounding influences on the lifetimes of centers and gives dispersion of the energy level of each center. Fig. 4.8b shows that the lifetime of the trap depends on its location depth in the forbidden band. This is explicitly expressed for the second type of traps with longer lifetimes.

Using the experimental values (Fig. 4.8a) and equation (4.6) the initial induced absorption spectrum of each long-lived trap can be found (Fig. 4.9). Using a similar method [101] the lifetimes of the traps were determined.

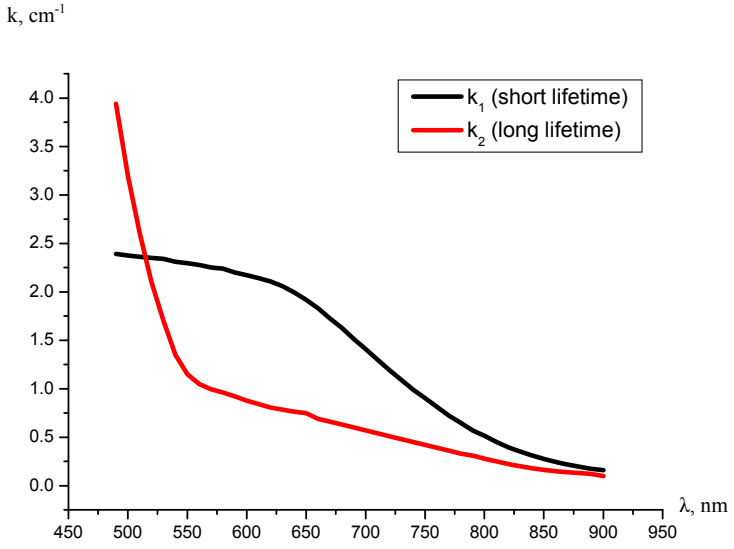

Fig. 4.9 Experimentally investigated absorption spectrum of the long-lived trap with short lifetime – red line and long lifetime – green line.

As it is seen in Fig. 4.10 the separated (calculated) initial absorption (black line) of the crystal is in good agreement with the measured one (dotted line). Therefore this is an indirect test of the correctness of the used method.

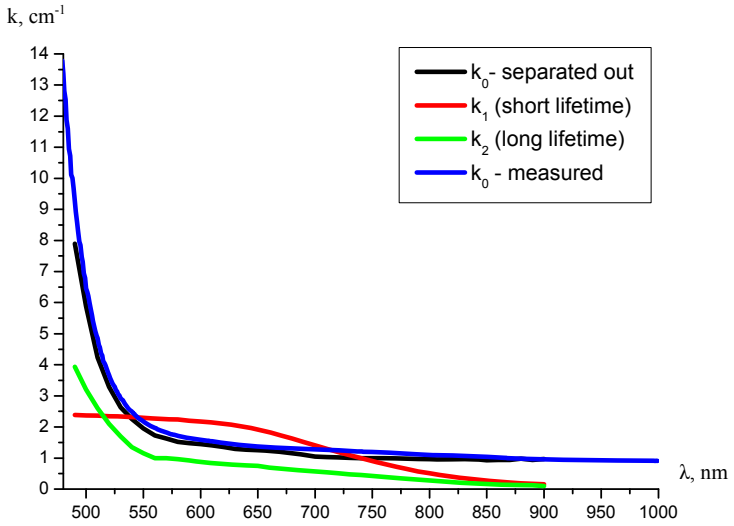

Fig. 4.10. Separated absorption spectrum of the long-lived trap with short lifetime – red line and long lifetime – green line, separated initial absorption of the non irradiated crystal – black line, direct measured real initial absorption of the non irradiated crystal – dotted line.

If the absorption characteristics are measured in the VIS at photorefractive semiconductor crystals one can use the scheme of the absorption presented in Fig. 4.11. The absorption coefficient k at the corresponding wavelength λ or energy $\hbar\omega$ can be described by

$$k(\hbar\omega) = \int_0^{\hbar\omega} N(E) \cdot S(E) \cdot dE \,, \tag{4.7}$$

where *N(E)*- is the density of the absorption centers, which is the quantity of absorption centers per volume unit with energy *E*. *S(E)* - is the cross section of the absorption of the absorption centers localized at the depth *E* in the forbidden band, $\hbar\omega$ – is the energy of the absorbed light quantum.

To simplify the discussion the parameter "level density" - *K(E)* can be introduced by

$$K(E) = N(E) \cdot S(E) \,, \tag{4.8}$$

which connects the absorption with the absorption centers localized at the depth *E*.

From equation (4.7) it is easy to isolate the level density

$$\frac{\partial k(\hbar\omega)}{\partial(\hbar\omega)} = K(\hbar\omega) \,. \tag{4.9}$$

According to the experimental absorption spectra of the traps (Fig. 4.9) one can calculate the level density for each of the long-lived traps in the forbidden band (Fig. 4.12).

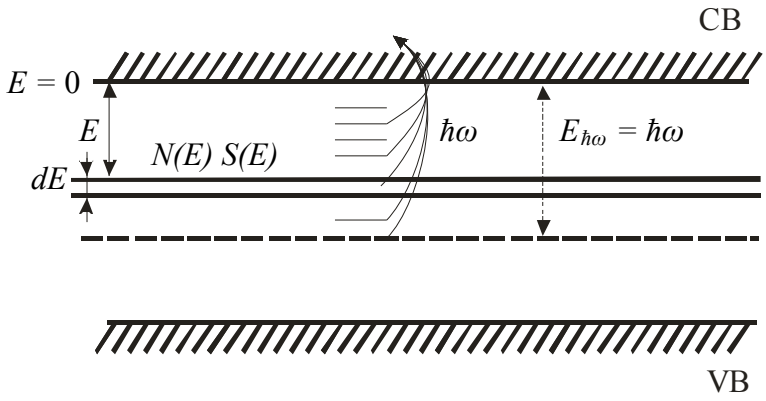

Fig. 4.11. Scheme of the transitions between energy levels and corresponding absorption of light. In the case of the photo-induced absorption, all electrons located in the forbidden band over the $E_{ħω}$ (energy of the absorbed light quant) can be excited to the CB by absorption of a light photon $ħω$.

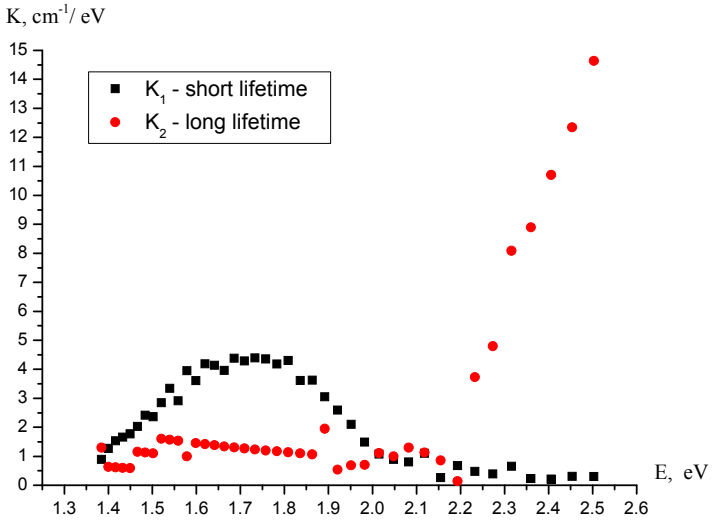

Fig. 4.12. Separated dependences of the long-lived traps level densities at the depth of the energy in the forbidden band with short lifetime – black line – and long lifetime – red line.

4.2.2 Hysteresis

It is found that the lifetimes differ by one order for both components and depend on the wavelength. This could be connected with the complex structure and the high vacancy of the tetrahedral lattice of sillenites [18]. The multicentered nature of photo-induced absorption was additionally proved by comparison of the absorption for different wavelengths. The phase-plane picture of the system for basic parameters: (absorption at 600 nm and 800 nm) is shown in Fig. 4.13. At the wavelengths 600 nm and 800 nm the effect of hysteresis can be

clearly seen. The existence of two different ways of evolution during inducing and relaxation of absorption (hysteresis) is the consequence of the multilevel structure of the long-lived levels in the forbidden band of the crystal. During relaxation the redistribution of charge carriers takes place between different levels with various spectral and temporal properties.

Thus, from the observations of the dynamics of the photo-induced absorption one can conclude about the multicentered nature of the long-lived levels in the forbidden band of BTO. At the same time the intraband transportation of energy results in a hysteresis behavior of the dark relaxation of the induced absorption relatively to the stimulation of the effect.

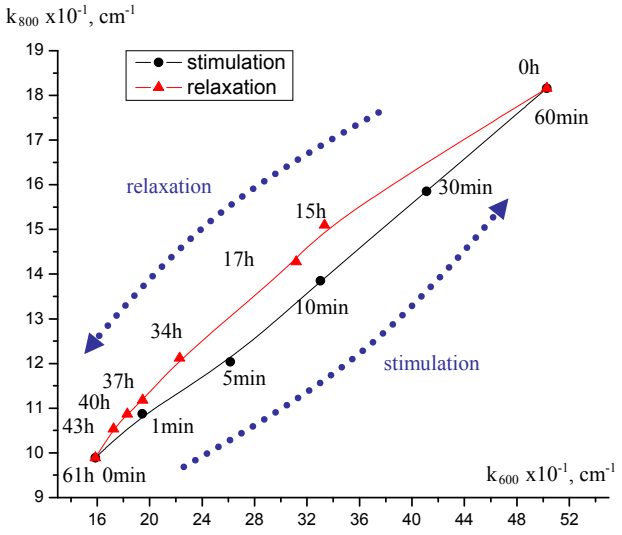

Fig. 4.13. Dependence of the absorption coefficient for the wavelength 800 nm on the absorption coefficient for the wavelength 600 nm (bistability). The exposure was realized with a pulse laser (average intensity - 110 mW/cm^2, 532 nm) during 1 hour. The relaxation was studied during 61 hours. The measurement error was less than 5%.

4.2.3 Dynamics of trap filling by electrons during relaxation of the induced absorption

It is possible to approximate theoretically the absorption spectrum during relaxation as it was made in chapter 4.1 for the laser-induced absorption and analyze it. In the process of dark relaxation (Fig. 4.14) a reduced contribution to the induced absorption for the first center that is described by the function $b_1(t)$ (Fig. 4.15) is nearly exponential, with the time constant ~ 18 h. We take into account that filling of these traps with the average ionization energy E_1 ~ 1.6 eV proceeds through the conduction band only, while their depletion occurs by means of

tunneling with subsequent recombination of the electrons into ionized donors and some lower lying traps. The possibility of such tunneling, by the way confirmed in [100] for lithium niobate with a high content of iron, stems from great concentrations of structural defects in bismuth titanate [85, 90]. Just trapping of some tunneling electrons into the centers with the average energy E_2 ~ 2.57 eV may be responsible for the nonmonotonic time dependence observed on relaxation of the photoinduced absorption changes due to these traps (curve $b_2(t)$ in Fig. 4.15).

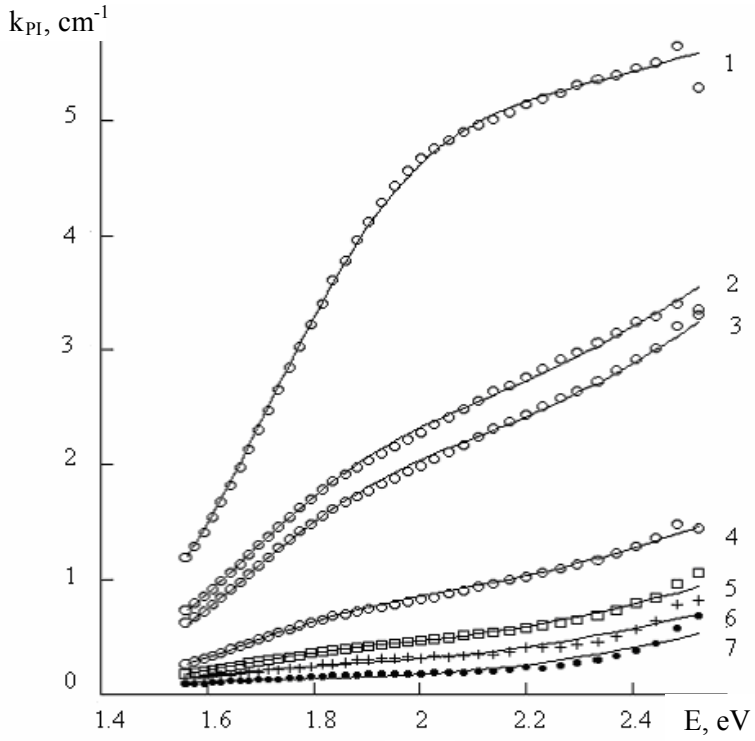

Fig. 4.14. Spectral dependences of additional absorption in a BTO crystal at the different relaxation stages: 0 (1), 15 (2), 17 (3), 34 (4), 40 (5), 43 (6), and 60 h. (7). Points - experiment, solid curves - theoretical approximation. Measurements errors are less than 5%

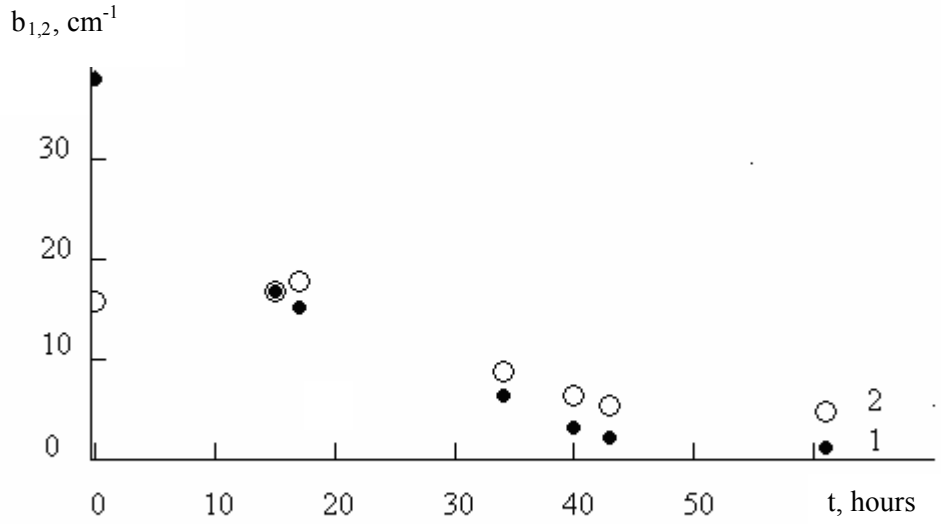

Fig. 4.15. Time profiles of the functions $b_1(t)$ and $b_2(t)$ which characterize the trap filling by electrons at the ionization energies $E_1=1.597$ eV (1) and $E_2=2.566$ eV (2) on illumination of the crystal by laser pulses (a) and at the relaxation stage (b).

4.2.4 Comparison of the experimental results with the theoretical model

In Fig. 4.16 the level density of the long-lived centers with lifetimes in the order of 10^4 s [101] is demonstrated. One can conclude that these traps are mostly localized at a depth of 1.7 eV with a half width of the level of about 0.5 eV. The center of the levels predicted by the theoretical calculations [43] is in good agreement with the experimental results, whereas the level width is greater than predicted. This means that the nature of the absorption is not pure as it was taken into account for the theoretical calculations but it is a mixture of accompanying effects like exciton interaction and others. This spreads the function of the absorption and shifts it.

Fig. 4.17 shows the level density of the long-lived centers with lifetimes in the order of 10^5 s [101]. The measured range of the absorption limits the investigation to the low energy part of these traps. Extrapolating the curve at Fig. 4.10 yields that the centre of the traps level is localized in the forbidden band at a depth greater than 2.5 eV and that its half width is

greater than 0.5 eV. These results are in agreement with the theoretically calculated values [43].

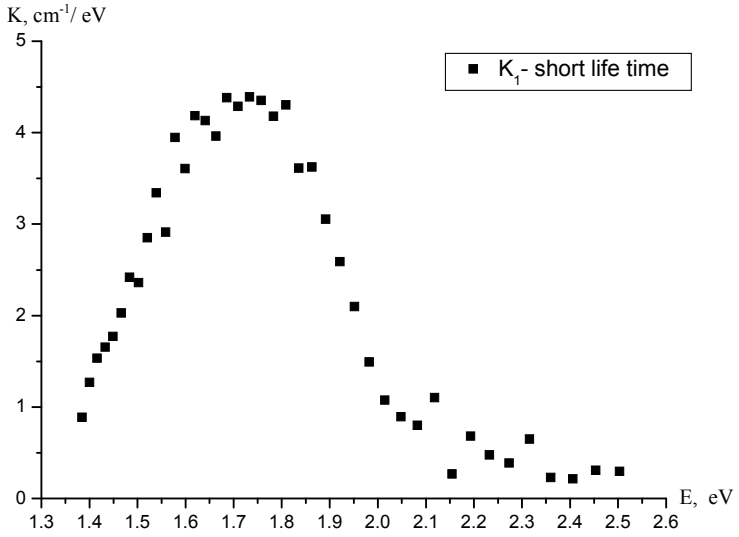

Fig. 4.16. Dependence of the long-lived traps level densities on the depth of the energy in the forbidden band with short lifetime.

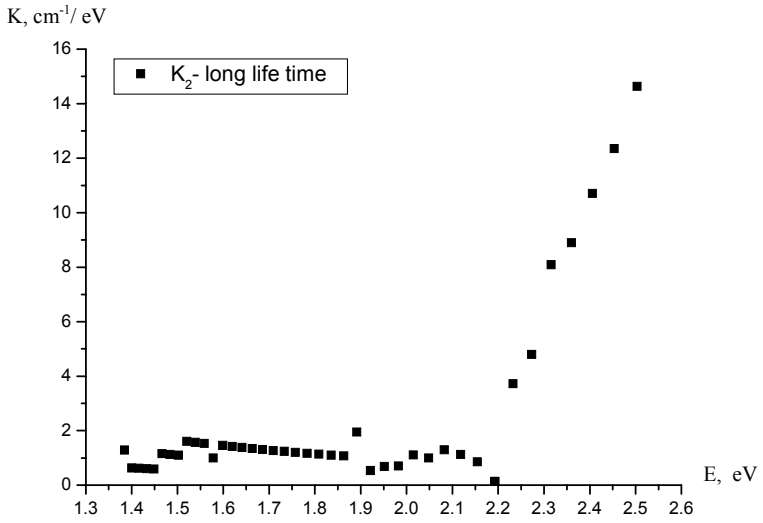

Fig. 4.17 Dependence of the long-lived traps level densities on the depth of the energy in the forbidden band with long lifetime.

4.3 Investigation of lifetime of electrons in the conduction band with four wave-mixing

Redistribution of the space charge at the traps produces an internal electrical field (Chapter 2.4). The electro-optical effect takes place. As result a modulation of the refractive index appears (Chapter 2.2 – 2.3). Detecting the changes of the refractive index one can measure the dynamic recombination of charges to the traps. Modulation of the refractive index produces Bragg phase diffraction gratings due to the photorefractive effect. Four wave-mixing generates a conjugate wave as a result. Studying the response dynamics of four wave-mixing yields the redistribution dynamics of the charge carriers between traps.

4.3.1 Experimental setup

The photorefractive response depends on the properties of the crystal. $Bi_{12}TiO_{20}$ belongs to the noncentrosymmetric class *23*. Being optically isotropic due to the cubic crystalline system, it has no inversion center and hence exhibits a linear electrooptic effect. The crystal displays the optical activity that in turn is independent of the light propagation direction, being described by the only constant: specific optical rotation or rotatory power. Both dextro- and levorotatory modifications are known, their specific activities being identical in absolute value. Impurity conductivity in the blue-green spectral region is the electronic conductivity. When no field is applied, the length of the photoexcited electron free path may be fairly large up to 10 μm. The BTO crystal is characterized by a high photoconductivity (compared to $LiNbO_3$) and hence it shows a rather fast response. At a power density of light of 1 W/cm^2 the recording/erasure cycle is effected (aiming at transfer to the stationary mode) in a few tenths of microseconds. A BTO crystal also features a relatively high electron mobility. Because of this, the drift mean free path of electrons may be comparable to the period of the excited light grating. In the general case, sillenite crystals, and BTO crystals in particular, demonstrate the diffusion-drift type of the photorefractive response. As previously mentioned, the diffusion charge transfer is due to the free-carrier density gradient (section 2.4.1), whereas the drift charge transfer is caused by the presence of an external field (section 2.4.2). We neglect the drift charge transfer, because an external field is not applied.

Fig. 4.18 shows the experimental setup used to create the four-wave mixing process in a BTO crystal with the help of a pulse laser. Within the crystal, three beams Lb1, Lb2, and Lb3 are convergent at a common point. Lb1 is the reference wave, Lb2 - reading wave that is propagating counter to the reference one, Lb3 - object wave. All these beams are coherent and interfere with each other to produce an interference pattern. A diffraction structure is recorded in the crystal. The beams, for which the necessary requirements are met, diffract from this structure.

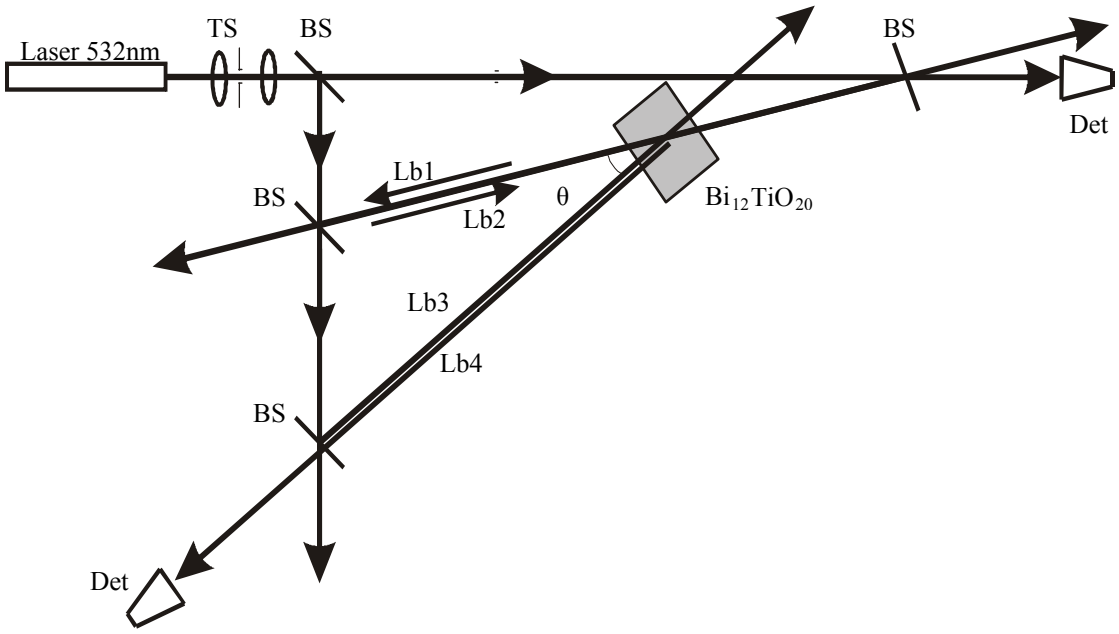

Fig. 4.18. Scheme of the experimental setup for the investigation of four-wave mixing. Laser 532 nm – Nd:YAG pulse laser, TS – telescopic system, BS – beam splitter, θ - angle between beams, Lb1, Lb2, Lb3, Lb4 – laser beams, Det – photodetector

4.3.2 Four wave-mixing

The interference pattern written in the crystal in our case may be represented as three independent interference patterns. The interference patterns are associated with the interference of the beam pairs Lb1 and Lb2, Lb2 and Lb3, Lb3 and Lb1.

These beams represent coherent plane waves with a horizontal polarization plane, and the interference of two beams results in the illumination-induced sinusoidal interference grating formed within the crystal. The illuminated regions exhibit manifestations of two phenomena associated with the radiant energy absorption: photogeneration of free carriers and

heating of the crystal lattice followed by the appearance of thermal optical nonlinearities. The first phenomenon that is essential for the photorefractive effect leads to the formation of the internal electrical field grating shifted by π/2 relative to the initial interference grating as it is shown in chapter 2.4. The internal electrical field affects the impermeability tensor η_{ij} and the index of refraction *n* due to the electrooptic effect

$$\Delta\eta_{ij} = \Delta\left(\frac{1}{n}\right)_{ij} = r_{ijk}E_k + s_{ijkm}E_kE_m\,, \tag{4.10}$$

where E_k, E_m are components of the electrical field, r_{ijk} are electrooptic coefficients, s_{ijkm} are quadratic electro-optic coefficients. For sillenite crystals the linear electrooptic effect is basic (Pockels-effect). For the crystal $Bi_{12}TiO_{20}$ equation (4.10) (Chapter 3)

$$\Delta n = -\frac{1}{2}n^3 r_{41}E\,. \tag{4.11}$$

The modulation of the refractive index induces a phase diffraction grating.

The second phenomenon results in the emergence of its own (thermal) phase diffraction grating without shift. It will be demonstrated that this thermal grating has no significant effect on measurements of the photorefractive dynamics due to the high characteristic time of the thermal nonlinearity. The exposition of the crystal at 532 nm by one pulse is low, so photo-induced absorption is not taking in account.

Four-wave mixing in a photorefractive crystal results in recording of three sinusoidal phase diffraction gratings with the involvement of the following beam pairs: Lb1 and Lb2, Lb2 and Lb3, Lb3 and Lb1. These gratings are of the Bragg-type. With the use of the above setup for two of the formed gratings, the Bragg condition of diffraction is met: for the grating formed between beams Lb2, Lb3 and the beam Lb1, grating between beams Lb3, Lb1 and the beam Lb2.

The fulfilled Bragg condition leads to diffraction of the reference and reading waves from the corresponding gratings with the phase conjugation of wave Lb4. The period of the grating formed by beams Lb3 and Lb1 is by an order of magnitude greater than that formed between Lb2 and Lb3, and the amplitude of the second grating is lower due to its smoothing under the effect of diffusion processes. The wave front reversal in turn may be considered as indication of the formation of a dynamic hologram in the photorefractive crystal. Comparing the intensities of the conjugate and object waves, one can estimate the efficiency of a diffraction grating formed in the medium.

Four-wave mixing in a BTO crystal is realized with a 532nm pulse laser. Varying the laser pulse length with constant energy of a single pulse, independent of its length, we can observe the dynamics of the diffraction efficiency exhibited by the formed hologram. Besides, we can estimate the time of the grating recording process based on the photorefractive effect in the BTO crystal.

Let us perform the calculations to determine the required time and experimental parameters. The grating period Λ is determined as

$$\Lambda = \frac{\lambda}{2 \cdot \sin\left(\frac{\Theta}{2}\right)}, \tag{4.12}$$

where θ - angle between Lb2 and Lb3 (θ = 18°). As a result, Λ = 1.7μm. This period is characteristic for the initial interference grating as well as for the gratings of thermal and electrooptic nonlinearities.

Thermal processes in the medium proceed at the speed of sound propagation in this medium ($\upsilon_{sound} \sim 5 \cdot 10^3$ m/s). Thus, the characteristic time of the thermal grating formation is given by

$$T_{therm} = \frac{\Lambda}{\upsilon_{sound}}, \tag{4.13}$$

whereas the characteristic relaxation (erasure) time for the thermal nonlinearity grating is determined by

$$\tau_{therm} = \frac{\Lambda^2}{4 \cdot \pi^2 \cdot a_{therm}}. \tag{4.14}$$

with a_{therm} the thermal conductivity coefficient, $a_{therm} \sim 10^{-3}$cm^2/s. Substituting the numerical values, we have $T_{therm} \sim 0.4$ ns, $\tau_{therm} \sim 200$ ns.

The calculation of the characteristic times for a grating of thermal nonlinearities is more difficult due to various factors affecting the grating formation. Because of this, only approximate estimates are given: τ_{eo} may be as great as hundreds of nanoseconds, and τ can reach a few minutes depending on the experimental conditions. Fig. 4.19 demonstrates the experimental diffraction efficiency of a hologram as a function of the laser pulse length used for its recording and reading. η_{hol} is the ratio of the diffracted beam's pulse energy to the incident beam's pulse energy.

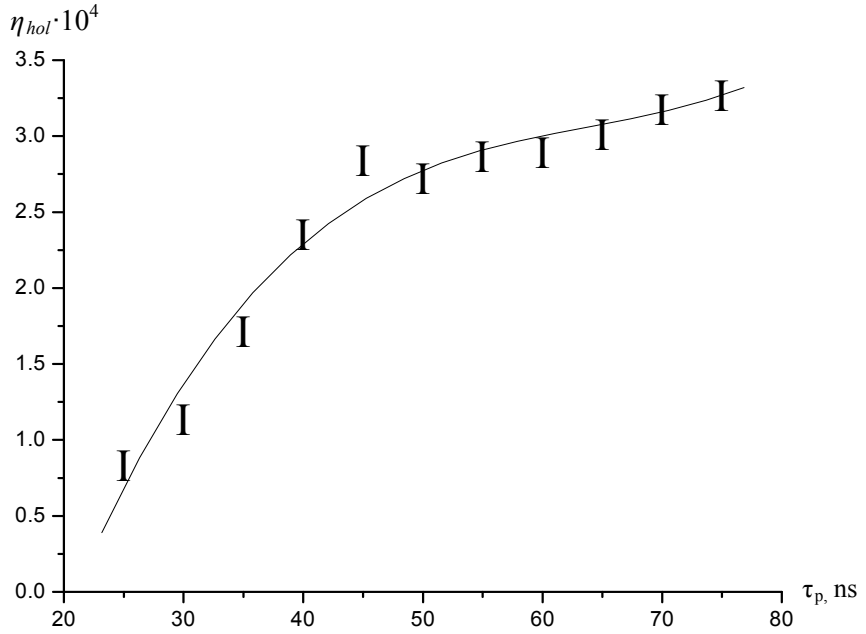

Fig. 4.19 Experimental diffraction efficiency of the formed hologram (η_{hol}) versus the recording pulse length (τ_p). The measurement error is less than 10%.

Fig 4.19 shows that the diffraction efficiency is increased with a growing length of the recording pulse.

As discussed above, two independent phase diffraction gratings in case under consideration appear in the crystal due to the

- thermal nonlinearity,
- electrooptic nonlinearity (photorefractive effect).

The characteristic time of the formation of a thermally nonlinearity grating in the case under study is T_{therm}~0.2 ns, being less than the pulse length or formation time of the electrooptic nonlinearity grating (and hence formation time of the photorefractive effect) by two orders of magnitude. This means that a thermal grating is formed and fixed during a laser pulse. However, the theoretical calculations demonstrate that a grating of thermal nonlinearity is considerably weaker than the grating caused by the photorefractive effect.

The transition of the thermal nonlinearity effect to the stationary mode is much faster than the pulse length. That's why the length of the pulse has no effect on the contribution made by the thermal grating to the phase conjugation. This contribution is influenced only by the initial energy of the laser pulse used for recording and reading.

So, a thermal grating formed by pulses with the same energy has the same contributions to the energy of a conjugate wave front independently of the recording pulse

length. In other words, the thermal grating is responsible for a minor constant component of the experimental diffraction efficiency, having no effect on its dynamics. It may be stated that the experimental dependence shows time of the formation of the photorefractive effect as a function of the recording pulse length.

Experimental measurements show that the time of the photorefractive response is approx. 50 – 60 ns. One can estimate that this is the characteristic time of the relaxation of the charge carriers from the CB to DT in the $Bi_{12}TiO_{20}$ crystal.

4.4 Methods for controlling of the laser-induced absorption in a BTO crystal by cw-laser radiation

4.4.1 Experimental setup

The investigation of the photo-induced absorption in BTO was carried out for a nominally pure $Bi_{12}TiO_{20,}$ which was grown from a congruent melt by the Czochralski method. It has the cubic symmetry 23 like all representatives of the sillenite family. The light radiation propagated along the [100] crystallographic axis. The (100) faces with transverse dimensions of 7x7 mm^2 were polished with optical quality. The thickness of the crystal in the [100] direction was 2.8 mm. The light induced absorption was realized by a cw-laser at 514 nm (Ar^+) (Fig. 4.20). The spatially homogeneous part of the laser beam was cut out by an aperture of 5.45 mm. The average power of the laser achieved 100 mW. The average intensity of the laser radiation incident on the crystal during the exposition was 430 mW/cm^2. The polarization of the laser light was located in the plane (100) and parallel to [011].

The absorption of the media was measured with a spectrophotometer based on a CCD line array with 2048 pixels. As the dispersion element a diffraction grating was used with 600 lines/mm. It results in a resolution of the absorption measurements less than 1 nm. The probe beam was emitted by a Xe/halogen lamp (Xe/HL) with a total intensity less than 0.8 mW/cm^2 in the whole spectral range. After 5 seconds of irradiation with the laser at 514 nm the spectrophotometer and the Xe/HL were switched on and the absorption was measured in the wave range between 480 nm and 1100 nm. The integration time of the CCD array was 11 ms. Therefore the time for one measurement corresponding to an averaging of 10 values of absorption was about 0.1 s. After 5 seconds of completing the measurement cycle the laser was switched on and the irradiation went on. During the measurement of the induced

absorption's relaxation the crystal was in darkness (laser was switched off) and with fixed room temperature.

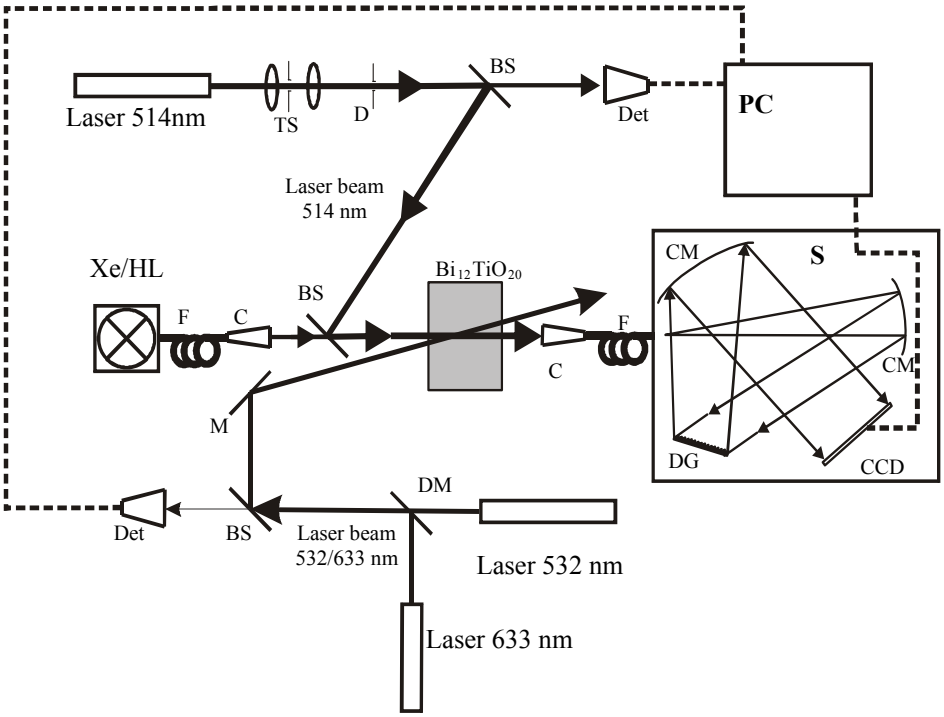

Fig. 4.20. Scheme of the experimental setup for the generation and measuring of the photo-induced absorption. Laser 514 nm – Ar^+ cw-laser, Laser 532 nm – Nd:YAG cw-laser, Laser 633 nm – He-Ne cw-laser, TS – telescopic system, D – diaphragm, BS – beam splitter, M – mirror, DM – dichroitic mirror AR@532 nm/HR@633 nm, Xe/HL – Xe/halogen lamp (200 nm-1000 nm), F - fiber optics, C – collimator, S – spectrophotometer, CM – collimating mirror, DG – diffraction grating, CCD – CCD linear array "Sony 2048", Det – photo detector, PC – computer.

In Fig. 4.21a and 4.21b the spectra of common and photo-induced absorption against the exposition energy are shown. A cw-laser with a wavelength of 514 nm was used for inducing of absorption.

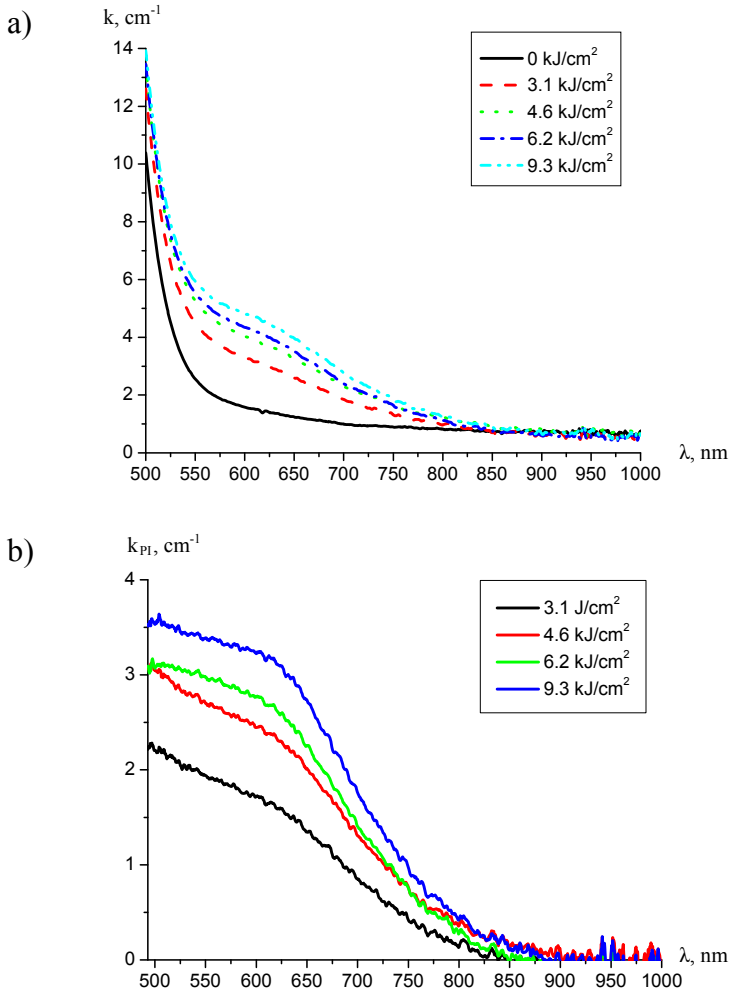

Fig. 4.21. a) Absorption spectrum of BTO for different values of the total exposition (J/cm^2). k is the absorption coefficient. b) Dependence of the photo-induced absorption k_{PI} (difference between integral absorption k and initial absorption without exposition k_0) for cw-laser: 430 mW/cm^2 at 514 nm.

4.4.2 Control of the photo-induced absorption in a BTO crystal by low intensity cw-lasers

The relaxation of the photo-induced absorption can be slowed down using cw-radiation with low intensity (Fig. 4.22, Fig. 4.23). If the photo-induced absorption is generated with an intensity of 430 mW/cm^2 at 514 nm, it is enough to use cw-radiation at the wavelengths 532 nm and 514 nm with low intensities (e. g. 12 mW/cm^2 and 15 mW/cm^2 correspondingly) to stop the relaxation process (Fig. 4.22). In such a way it is possible to stop the relaxation at any stage. If one switches off the low cw-radiation, the relaxation process resumes (Fig. 4.23).

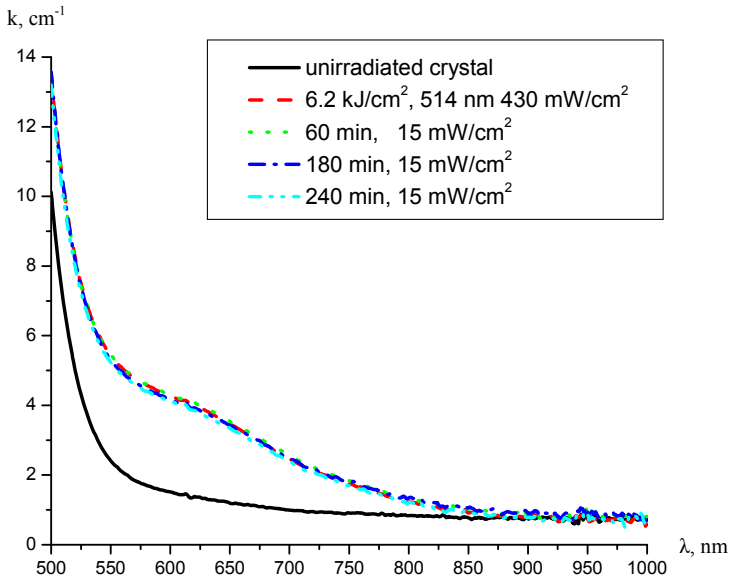

Fig.4.22. Influence of the cw-radiation with the low intensity 15 mW/cm^2 and wavelength 514 nm on the photo-induced absorption of BTO. The absorption is generated by cw-radiation: 430 mW/cm^2 at 514 nm.

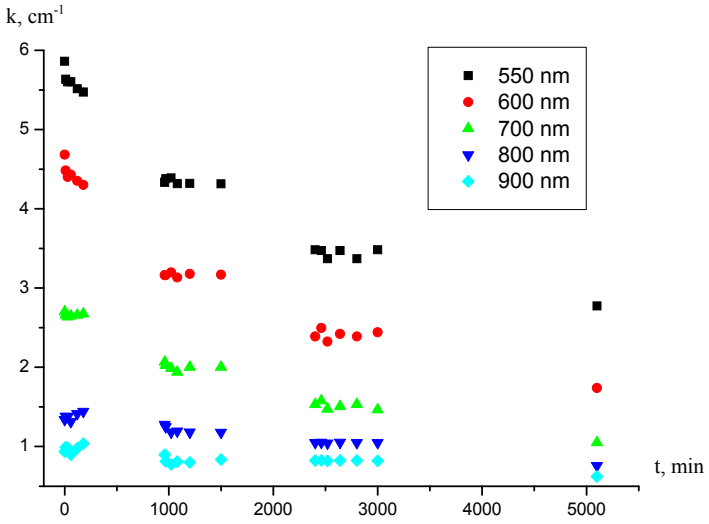

Fig.4.23 An example for the temporal retardation of the relaxation at different stages by a cw-radiation with low intensity 12 mW/cm^2 at 532 nm in BTO. It demonstrates the dependence of the coefficient of absorption on the time of free relaxation and cw-radiation at 532 nm for the given wavelengths; during the free relaxation the cw-radiation at 532 nm is switched on for 0-180 min., 970-1500 min., 2400-3000 min (there are three plateaus at the curves).

If the BTO crystal with induced absorption is exposed by a cw-radiation at 633 nm with low intensity (e. g. 17 mW/cm^2), the relaxation is accelerated. If one switches off the low cw-radiation of 633 nm, the relaxation process resumes with the evolution as without previous acceleration (Fig. 4.24). One can calculate the exponential lifetime of the photo-induced

absorption under stimulation of the relaxation (Fig. 4.24b). Compared with the results from [101] for the unstimulated relaxation red light accelerates the relaxation approximately by a factor of 10.

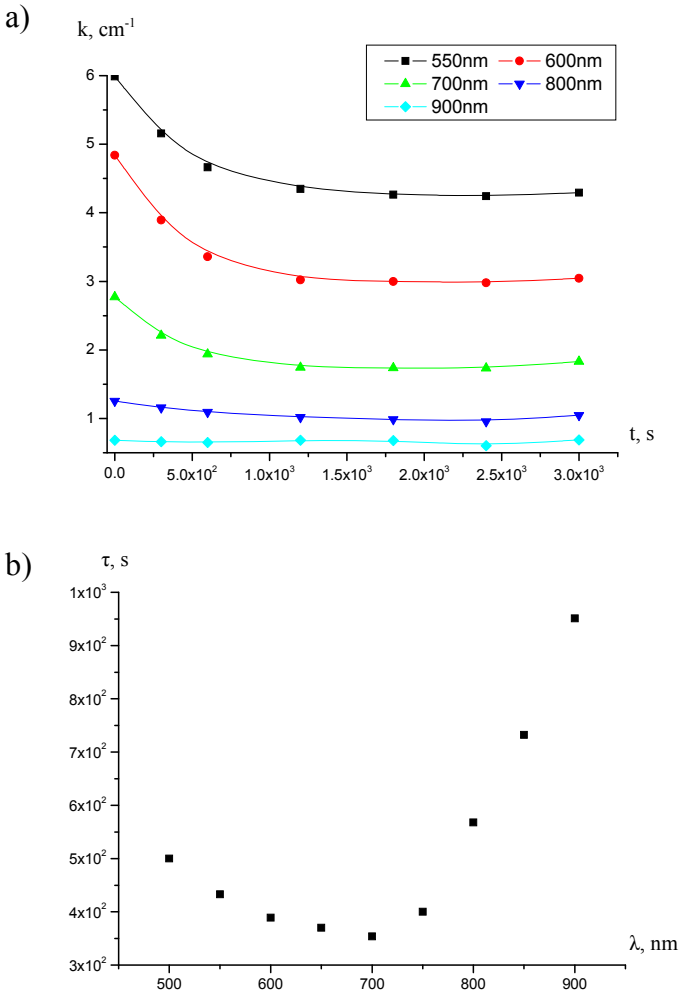

Fig.4.24. Example for the temporal acceleration of the relaxation at different stages by a cw-radiation with low intensity 17 mW/cm^2 at 633 nm in BTO. a) Dependence of the coefficient of absorption for the given wavelengths on the time of exposition, b) dependence of the calculated long-lived centers lifetimes on the probe beam wavelength.

Low intensity cw-radiation of the wavelengths 514 nm, 532 nm, and 633 nm didn't produce enough photo-induced absorption to be experimentally detected. Thus, one can use low intensity expositions at different wavelengths in order to control the photo-induced absorption.

Qualitatively, the mechanism of induced absorption can be explained by the scheme in Fig. 4.25. The long-lived absorption is connected with a population of the IT. During relaxation of the crystal the number of absorption centers at the trap levels decreases with

approx. lifetimes of 10^4 s and 10^5 s [101]. This quantity can be kept invariable. Using low intensity exposition of "green" light one transfers electrons from DT to IT. When the number of transferred electrons is equal to the number of relaxed ones from IT to VB or DT than the absorption remains constant (Fig. 4.25a). The induced absorption relaxation can be accelerated by low intensity "red" radiation. In this case the radiation excites electrons from IT to CB with a following relaxation to the VB. Together with the normal relaxation this speeds up the decreasing of the absorption (Fig. 4.25b).

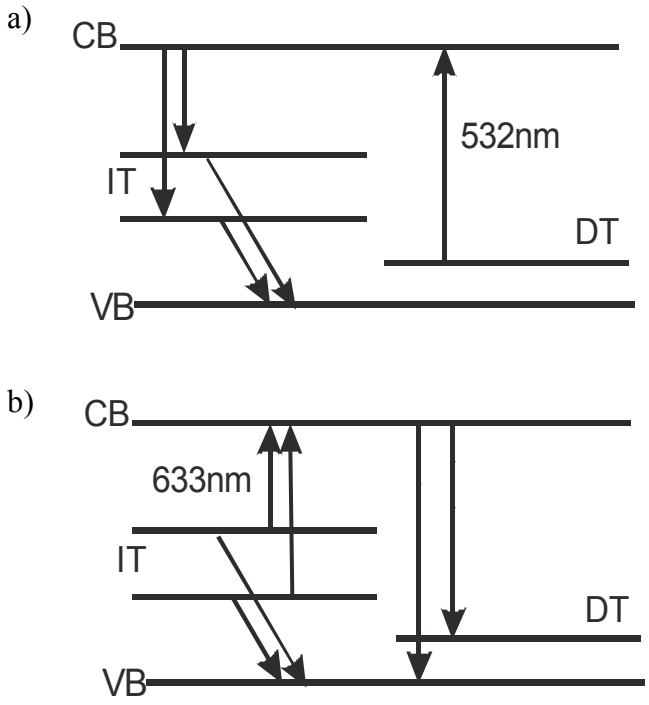

Fig. 4.25. Schematic illustration of the photo-induced absorption in BTO controlled by "green" and "red" radiations. a) – stopping of the relaxation by light at 532 nm, b) speeding of the relaxation by light at 633 nm.

According to the experimental results one is able to write down the coupling equation for describing of the BTO dynamical characteristics, which is also schematically illustrated in Fig 4.26 (Chapter 2)

$$\frac{\partial N_1}{\partial t} = -S_1 I N_1 + r_{3,1} N_3 N_1^+ + r_{2a,1} N_1^+ N_{2a} + r_{2b,1} N_1^+ N_{2b}, \tag{4.15}$$

$$\frac{\partial N_{2a}}{\partial t} = -S_{2a} I N_{2a} + r_{3,2a} N_3 N_{2a}^+ - r_{2a,1} N_1^+ N_{2a} - \beta_{a,b} N_{2a} + \beta_{b,a} N_{2b}, \tag{4.16}$$

$$\frac{\partial N_{2b}}{\partial t} = -S_{2b} I N_{2b} + r_{3,2b} N_3 N_{2b}^+ - r_{2b,1} N_1^+ N_{2b} + \beta_{a,b} N_{2a} - \beta_{b,a} N_{2b}, \tag{4.17}$$

$$\frac{\partial N_3}{\partial t} = S_1 I N_1 + S_{2a} I N_{2a} + S_{2b} I N_{2b} - r_{3,1} N_3 N_1^+ - r_{3,2a} N_3 N_{2a}^+ - r_{3,2b} N_3 N_{2b}^+ . \quad (4.18)$$

N_1, N_{2a}, N_{2b}, N_3 are the concentrations of the charge carriers (electrons) involved in the phenomena at the levels of deeps traps, lower long-lived traps, upper long-lived traps and the conducting band respectively. N_1^+, N_{2a}^+, N_{2b}^+ are the corresponding concentrations of the ionized centers (ready to "receive" electron) at the levels of the traps. S_1, S_{2a}, S_2 are cross sections of the light quantum absorption during excitation of the electrons from traps to CB. S_i is a function of the light frequency $S_i(\omega)$ and the depth of the level in the forbidden band. $r_{i,j}$ are the recombination coefficients from the upper level i to the lower j. $\beta_{a,b}$ and $\beta_{b,a}$ are the constants defining inner transitions coefficients between long-lived levels caused by thermal excitation, recombination, tunneling and etc. According to the initial spectrum of the absorption and especially low absorption in the long-wave range one may ignore thermal ionization between DT, IT and CB. Low long-wave absorption at the final spectrum means insignificant light induced transition of the electrons between the long-lived traps. I is the intensity of the homogenous and uniform light with the frequency ω measured in $\frac{photon}{m^2 \cdot s}$.

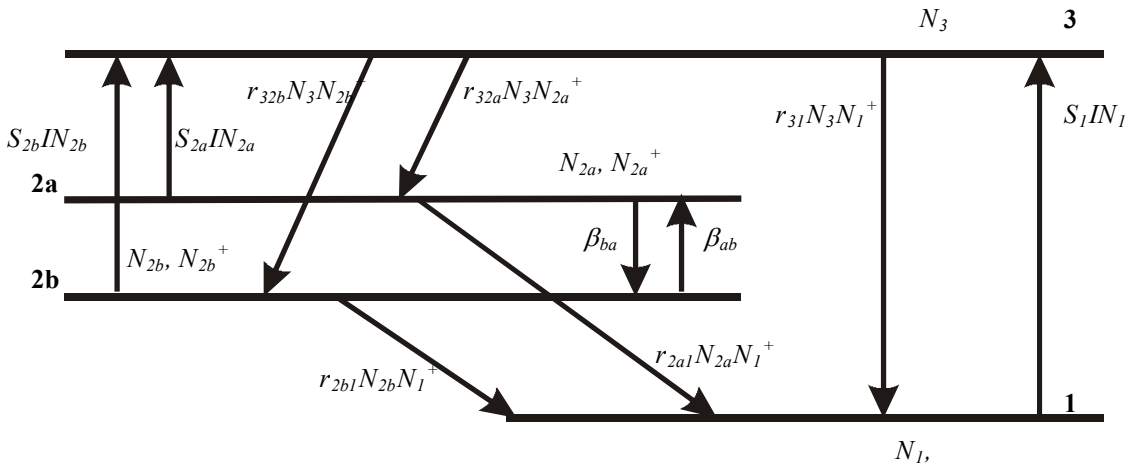

Fig. 4.26. Schematic illustration of electron transitions between levels of the photo-induced absorption in BTO.

As the result of the initial electric neutrality of the crystal

$$N_1 + N_{2a} + N_{2b} + N_3 = N_1^+ + N_{2a}^+ + N_{2b}^+ + N_3^+ . \quad (4.19)$$

In such way the absorption coefficients of the light for the wavelengths 514 nm and 532 nm have the form

$$k = S_1 N_1 + S_{2a} N_{2a} + S_{2b} N_{2b} , \quad (4.20)$$

The corresponding photo-induced absorption is

$$k_{pi} = S_{2a}N_{2a} + S_{2b}N_{2b}\,. \tag{4.21}$$

The average recombination coefficient $r_{2,1}$ is

$$r_{2,1} = \frac{r_{2a,1}\cdot N_{2a} + r_{2b,1}\cdot N_{2b}}{N_{2a} + N_{2b}}\,. \tag{4.22}$$

Physically this means a common probability of recombination of the electrons from IT to DT. $r_{3,2}$ is the average recombination coefficient for recombination of the electrons from CB to IT

$$r_{3,2} = \frac{r_{3,2a}\cdot N_{2a}^{+} + r_{3,2b}\cdot N_{2b}^{+}}{N_{2a}^{+} + N_{2b}^{+}}\,, \tag{4.23}$$

S_2 is the average absorptions cross section for the IT

$$S_2 = \frac{S_{2a}\cdot N_{2a} + S_{2b}\cdot N_{2b}}{N_{2a} + N_{2b}}\,. \tag{4.24}$$

After the summation of the (4.16) and (4.17) and considering equations (4.22) - (4.24) we can write Eqs. (4.15) - (4.18) as follows

$$\frac{\partial N_1}{\partial t} = -S_1 I N_1 + r_{3,1}N_3N_1^{+} + r_{2,1}N_1^{+}(N_{2a} + N_{2b})\,, \tag{4.25}$$

$$\frac{\partial (N_{2a} + N_{2b})}{\partial t} = -S_2 I (N_{2a} + N_{2b}) + r_{3,2}N_3(N_{2a}^{+} + N_{2b}^{+}) - r_{2,1}N_1^{+}(N_{2a} + N_{2b})\,, \tag{4.26}$$

$$\frac{\partial N_3}{\partial t} = S_1 I N_1 + S_2 I (N_{2a} + N_{2b}) - r_{3,1}N_3N_1^{+} - r_{3,2}N_3(N_{2a}^{+} + N_{2b}^{+})\,. \tag{4.27}$$

The general and the photo-induced absorption coefficients obtain the form

$$k = S_1N_1 + S_2N_2\,, \tag{4.28}$$

$$k_{pi} = S_2N_2\,. \tag{4.29}$$

As it was shown in the experiment (Fig. 4.22) for a low intensity radiation at the wavelength response for inducing of the long-lived absorption, relaxation stopped. This means that the system was in equilibrium.

Under these conditions (Fig. 4.22) the adiabatic approximation $\frac{\partial N_i}{\partial t} = 0$ can be used, and Eqs. (4.25) - (4.27) take the from

$$0 = -S_1 I N_1 + r_{3,1}N_3N_1^{+} + r_{2,1}N_1^{+}N_2\,, \tag{4.30}$$

$$0 = -S_2 I N_2 + r_{3,2}N_3N_2^{+} - r_{2,1}N_1^{+}N_2\,, \tag{4.31}$$

$$0 = S_1 I N_1 + S_2 I N_2 - r_{3,1}N_3N_1^{+} - r_{3,2}N_3N_2^{+}\,. \tag{4.32}$$

The characteristic recombination time of the electrons from the CB to the DT and VB lays in order of 10 ns [96]. On the other hand the characteristic recombination time of the electrons from the IT to the DT and VB averages out hours [101]. That's why

$$r_{3,1} >> r_{2,1}, \tag{4.33}$$

and Eq. (4.30) takes the form

$$S_1 I N_1 = r_{3,1} N_3 N_1^+ . \tag{4.34}$$

Taking into account (4.32) and (4.34) yields

$$S_2 I N_2 = r_{3,2} N_3 N_2^+ , \tag{4.35}$$

and from the equation of (4.34) and (4.35) we get

$$\frac{S_1 N_1}{S_2 N_2} = \frac{r_{3,1} N_1^+}{r_{3,2} N_2^+} . \tag{4.36}$$

In other words

$$\frac{k_0}{k_{pi}} = \frac{R_{3,1}}{R_{3,2}} , \tag{4.37}$$

where k_0 and k_{pi} are the initial and the photo-induced absorption coefficients reached during the "relaxation stopping" experiment. $R_{3,1}$ and $R_{3,2}$ are the relaxation constants from CB to DT and IT respectively. $R_{3,1}$ and $R_{3,2}$ are inverse parameters to the lifetimes of the electrons at the levels $\tau_{3,1}$ and $\tau_{3,2}$. So one finds out the ratio between the electron recombination from CB to long-lived IT and DT. This ratio shows that the electrons ionized to the CB have a relaxation probability to the long-lived IT, which is 1.2 times lower than to the DT for 532 nm (1.9 for 514 nm).

Our conclusions may be applied to all the wavelengths of the range, which can induce the absorption. For wavelengths of the stimulation range one can present a dependence of the ratio (4.36) on the wavelength (Fig. 4.27). According to the spectrum of the initial absorption (Fig. 4.21a) the stimulation range lies up to the 580 nm. However, this border is dither and depends on the complex nature of the traps. The dependence on the wavelength is the result of the broad long-lived energy level and of the various concentrations of the absorption centers therein.

According to this result and to our previous experimental investigations [101, 96] one can estimate the dynamical characteristics of the levels (traps) (Table 4.1) illustrated in Fig. 4.28.

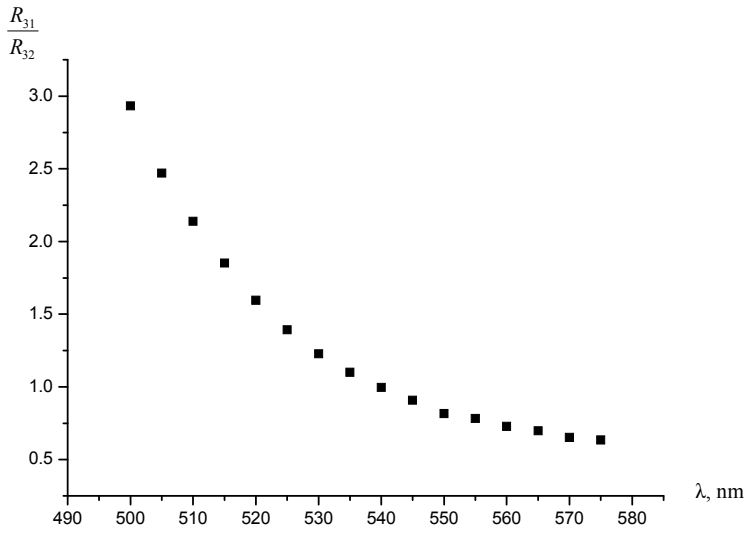

Fig. 4.27. Dependence of the ratio of the effective recombination coefficients on the stimulation wavelength.

λ, nm	514	532
$\tau_{2a,1}$, s	$1.2\text{x}10^{4}$	$1\text{x}10^{4}$
$\tau_{2b,1}$, s	$5.5\text{x}10^{4}$	$7.5\text{x}10^{4}$
$\tau_{3,1} = \frac{1}{R_{3,1}}$, s	$\sim 6\text{x}10^{-8}$	$\sim 6\text{x}10^{-8}$
$\tau_{3,2} = \frac{1}{R_{3,2}}$, s	$\sim 12\text{x}10^{-8}$	$\sim 7\text{x}10^{-8}$

Table 4.1. Dynamical characteristics of the nominally pure $Bi_{12}TiO_{20}$

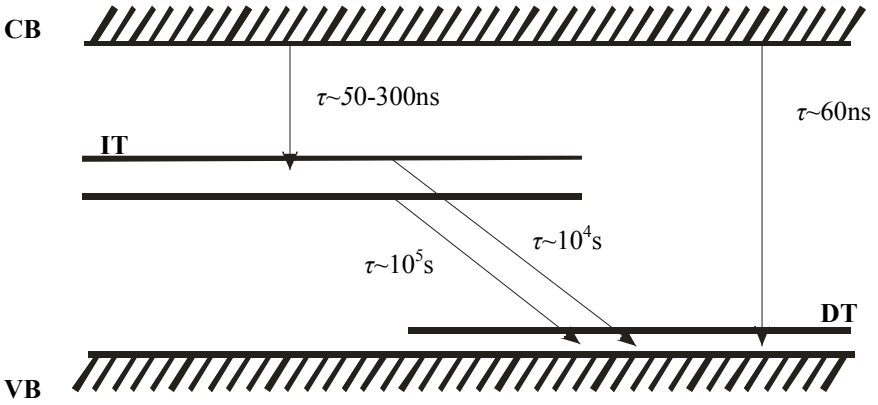

Fig. 4.28. Dynamical characteristics of the nominally pure $Bi_{12}TiO_{20}$

4.5 Evolution dynamics of the photo-induced light absorption in sillenite crystals for ns and ps laser pulses

As described in chapter 4.4, no photo-induced absorption is observed in a bismuth silicate crystal at temperatures from 25 ^{0}C and light intensities from 1 to 100 mW/cm^2. This is in agreement with the data of [85], where a maximum photochromic effect in BSO, BGO, and BTO is observed at $T < 200$ K.

In this chapter the evolution dynamics of the photoinduced light absorption is analyzed for a bismuth titanate crystal on the base of its band structure and the material parameters at the corresponding temperature. An analysis is performed on a time scale comparable with the width of the ns or ps illumination pulses.

4.5.1 Evolution dynamics of the photo-induced light absorption in BTO crystals on illumination by ns pulses

The photo-induced light absorption dynamics, when the extended illumination is switched on or switched off, is adequately described by the model from chapter 4.4. The system of coupled rate equations associated with this model (4.15) - (4.18) is nonlinear for pulse laser radiation, and its analysis may be performed by numerical methods only. The intensity of a light pulse may be given as

$$I(t) = I_p \left[\theta(t) - \theta(t - \tau_p) \right], \tag{4.38}$$

with $\theta(t)$ - step Heaviside function, τ_p - pulse width. The intensity of the laser pulse with $\tau_p = 50$ ns used for illumination of the bismuth titanate crystal is ~ $2 \cdot 10^9$ W/m^2.

The results of numerical analysis for the dynamics of the electron redistribution in donor and trapping centers as well as for the changes in electron concentrations within the conduction band and in optical absorption of a bismuth titanate crystal at a temperature of 25 ^{0}C are presented in Fig. 4.29. The rate of an increase or decrease in the electron concentrations within the conduction band under the effect of a light pulse (Fig. 4.29a) is determined by their lifetime that is close to the time of recombination into the N_{2a}^+- and N_{2b}^+-type centers,

$$\tau^{e}_{N^{+}_{2a},N^{+}_{2b}} = \frac{1}{(r_{3,1} + r_{3,2b}) \cdot (N_D - N^{+}_{2a} - N^{+}_{2b})}. \tag{4.39}$$

n – the concentration of electrons in the CB, N_D – total amount of the donor centers in the forbidden band.

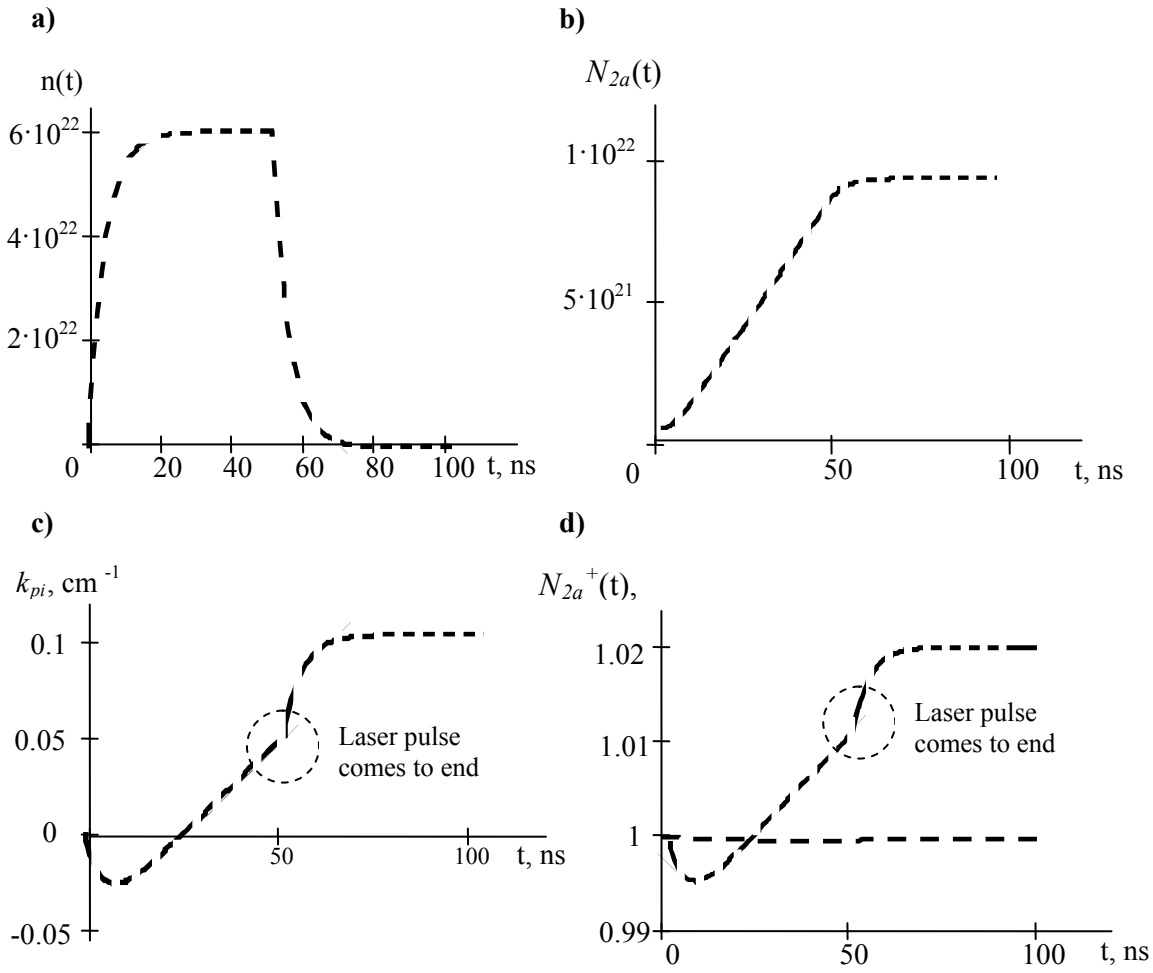

Fig. 4.29 Calculated from the experimental measurements: electron concentrations at the conduction band under the effect of a light pulse a), population of the N_{2a}^{+}-type centers by electrons b), change of optical absorption c), population of donors and traps per laser pulse d). Electronic noise of the detection system is the cause of the noise at the dependence in the fig. b). The common measurement error is less than 3%.

The population of the N_{2a}^{+}-type centers by electrons occurs in the course of time of their existence within the conduction band (Fig. 4.29b), their contribution to a change in optical absorption (Fig. 4.29c) being relatively small. Characteristics for the initial illumination stage are the decreasing of electron population of donors and traps (Fig. 4.29d) due to photoexcitation that leads to crystal bleaching. However, at $t > 8$ ns the rate of recombination

into traps begins to exceed the electron photoexcitation rate, and optical absorption of the crystal is growing up to k_{pi}~ 0.1 cm^{-1}, that is provided by the first illuminating pulse.

The time required for depletion of traps that may be estimated as

$$\tau^{N_{2b}^{+}} = \frac{1}{\beta \cdot \exp(-\frac{E_a^{N_{2b}}}{k_B T})}, \tag{4.40}$$

comes to about 3000 s and hence the attained value of an increase in the crystal absorption is retained to the beginning of the next light pulse. $E_a^{N_{2b}}$ is the energy of the thermal activation of the donor $N_{2b.}$

4.5.2 Evolution dynamics of the photo-induced light absorption in BTO crystals on illumination by ps pulses

100-ps laser pulses have a length of about 12 mm in crystals of sillenites with the refractive index $n \sim 2.5$. This is comparable to the thickness of photorefractive samples.

The foregoing system of rate equations (4.15) - (4.18) is valid in all the cases when the photoexcited electrons are thermalized, i.e. when we can neglect the contribution made by so-called "hot" electrons for the charge transfer processes which provide the formation of photorefractive holograms. According to [102], the relaxation time of the nonthermalized charge carriers down to the conduction band bottom in a photorefractive lithium niobate crystal is in the order of 0.1 ps. Assuming the same order for the electron thermalization time in bismuth titanate, when analyzing the evolution dynamics of the photo-induced light absorption in this crystal on illumination by 100-ps pulses, we can use the system of rate equations (4.15) - (4.18).

The results obtained by the numerical analysis of the electron redistribution dynamics in donor and trapping centers as well as of the changes in the electron concentrations within the conduction band and in optical absorption of bismuth titanate at 25^{0}C are shown in Fig. 4.30, at the time scale associated with the time of the electron recombination processes $\tau^{e}_{N_{2a}^{+},N_{2b}^{+}}$. It is assumed that the energy of the light pulse is the same as for the above-mentioned nanosecond pulse ($I_p = 10^{12}$ W/m^2). As demonstrated by comparison of Figs. 4.29 and 4.30, the changes of the electron redistribution in the defect centers and also in optical absorption as the result of the recombination processes are nearly identical in both cases. The

efficiency of the initial crystal bleaching by a picosecond pulse is by an order of magnitude higher than that for the crystal bleaching induced by the nanosecond pulse with the same energy.

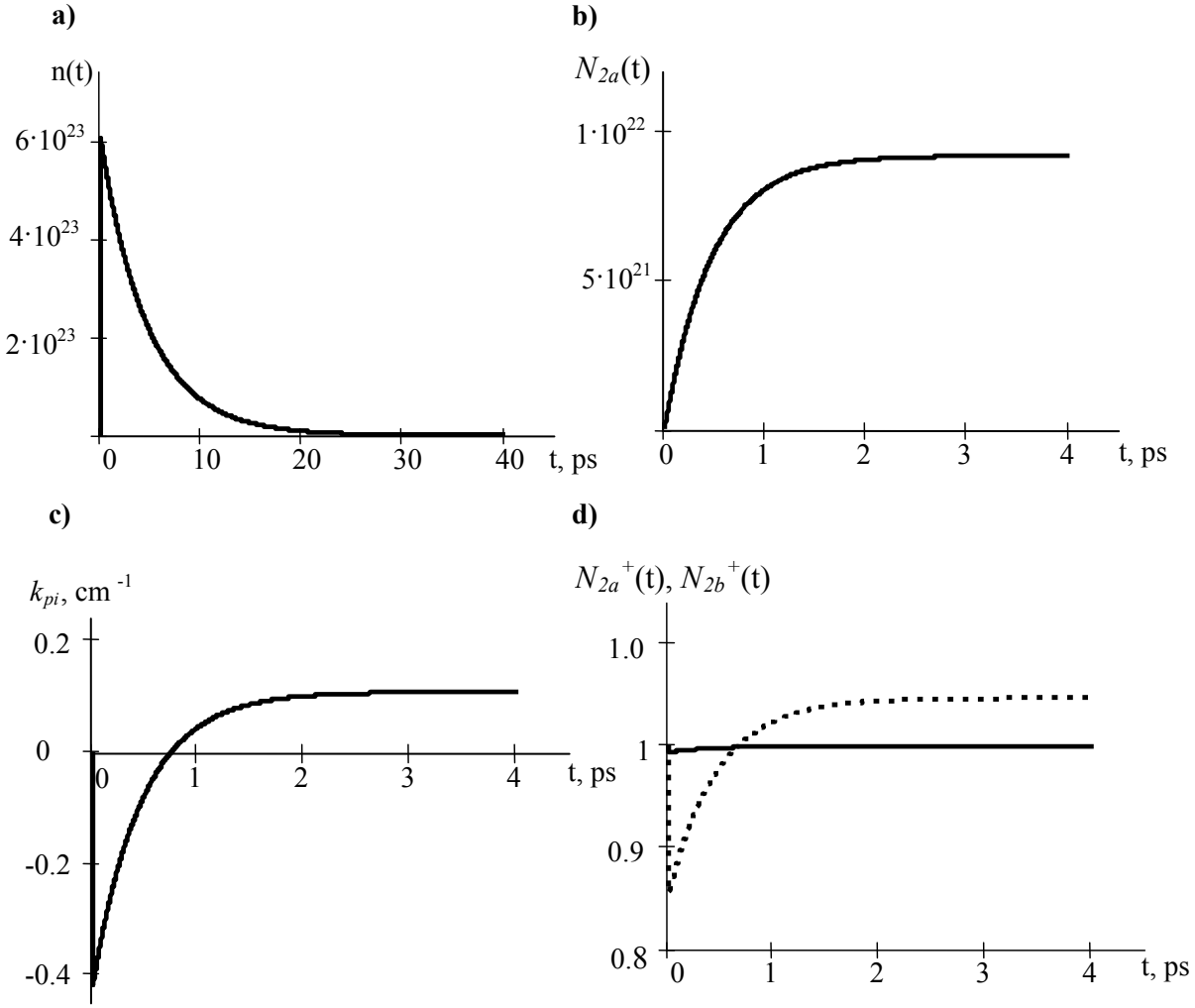

Fig. 4.30 Calculated from the experimental measurements: electron concentrations at the conduction band during illumination of the laser pulse a), population of the N_{2a}^{+}-type centers by electrons b), change in optical absorption c), population of donors and traps d).

4.6 Comparison of the induced absorption in photorefractive BTO and BSO crystals

The experiments have been conducted with monocrystalline samples of bismuth titanate $Bi_{12}TiO_{20}$ and bismuth silicate $Bi_{12}SiO_{20}$. The samples were grown in a platinum crucible in the air using the seed with [100] orientation and under the conditions specified in

[25, 85]. The (100)-cut plates of the single crystal were subjected to grinding and polishing to attain the optical grade quality.

Absorption spectra of these samples $T(\lambda)$ in the region 350 to 900 nm were recorded by a Specord M40 spectrophotometer. The measurement error $\Delta T / T$ was below 0.02. The spectral dependence of the light absorption factor $k(\lambda)$ was calculated as [103]

$$T = \frac{(1-R)^2 \exp(-kd)}{1-R^2 \exp(-2kd)}, \tag{4.41}$$

where d – sample thickness, R – Fresnel coefficient for reflection from the crystal edge.

The experimentally obtained curves as a function of the quantum energy $k(E)$ for the region of impurity absorption, where the long wavelength limit is determined by the admissible experimental error and the short wavelength one – by the bandgap E_g, are denoted by circles in Figs. 4.4, 4.31 and 4.32 for BTO (E_g = 3.08 eV [85]) and BSO (E_g = 3.25 eV [85]) crystals, respectively. The logarithmic scale used here for the absorption factor enables one to distinguish the spectral curve bends known as absorption "shoulders" [84, 85].

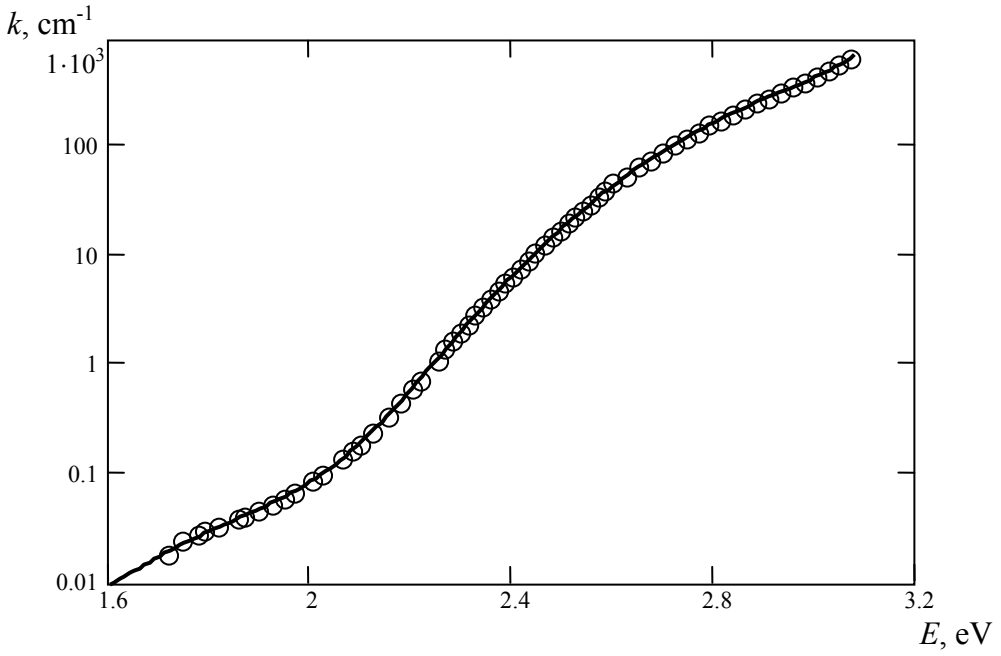

Fig. 4.31. Spectral dependences of the impurity absorption in a BTO crystal. Points - experiment, solid curve – theoretically calculated.

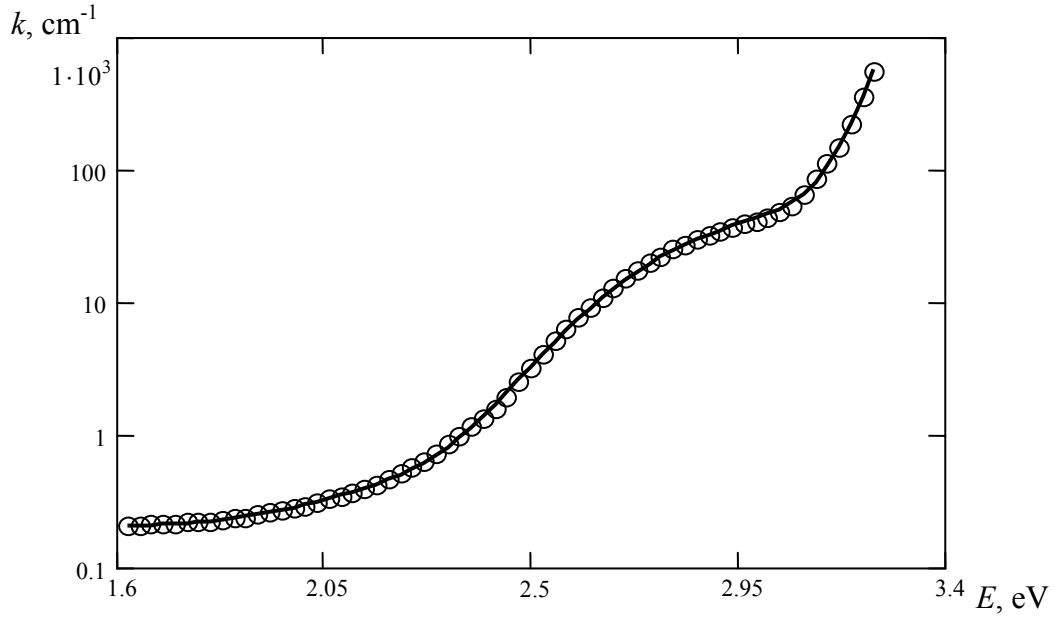

Fig. 4.32. Spectral dependences of the impurity absorption in a BSO crystal. Points - experiment, solid curve – theoretically calculated.

As is known [84, 85, 90, 103], in many crystalline materials including the sillenites the curve $k(E)$ close to the fundamental absorption edge follows the exponential law that is called Uhrbach rule. As seen in Fig. 4.33, such a situation is observed in BSO crystals at the quantum energy from 3.15 to 3.25 eV. And further, at $E < 3.15$ eV, the absorption "shoulder" is observed. In the case of a BTO crystal this shoulder is directly adjacent to the fundamental absorption edge at $E = E$g = 3.08 eV (see Fig. 4.4, 4.32).

Approximating the absorption spectra of nonilluminated crystals in the "shoulder' region, we assume that photoexitation of the electrons is mostly from deep donors described by equations (4.1), (4.2). As a result, the spectral dependence of the absorption factor is given in the form

$$k(\hbar\omega) = k_U \exp\left(-\frac{E_g - \hbar\omega}{E_U}\right) + \int_0^{\hbar\omega} B_D(E_I)\frac{\sqrt{\hbar\omega/E_I - 1}}{(\hbar\omega/E_I)^3}\frac{1}{1+\exp\left[(E_F - E_I)/k_BT\right]}dE_I \,, \quad (4.42)$$

where E_U is the characteristic energy conforming to the Uhrbach rule that is proportional to *kBT* at high temperatures [103]. The function B_D (E_I) that determines the light absorption by donor centers taking place within the ionization energy interval dE_I represented from (4.3) as the superimposed contributions of the donor centers following the normal distribution law

$$B_D(E_I) = \sum_n b_n^D \exp\left[-\frac{\left(E_n^D - E_I\right)^2}{\left(\Delta E_n^D\right)^2} \right]. \tag{4.43}$$

The experimental results for BTO and BSO crystals are well approximated within this model (see solid curves in Figs. 4.31 and 4.32) based on three donor-traps centers (two intermediate traps IT and one deep trap DT at the scheme Fig 4.3).

Crystal	$Bi_{12}TiO_{20}$	$Bi_{12}SiO_{20}$
E_1^{IT}, eV	1.597	1.111
E_2^{IT}, eV	2.566	2.525
E^{DT}, eV	2.897	2.751
ΔE_1^{IT}, eV	0.277	0.167
ΔE_2^{IT}, eV	0.580	0.598
ΔE^{DT}, eV	0.326	0.259
b_1^{IT}, cm^{-1}/eV	0.088	5.152
b_2^{IT}, cm^{-1}/eV	1.561	6.936
b^{DT}, cm^{-1}/eV	4545	440
E_U , eV	0.0585	0.0469
k_U , cm^{-1}	228	601

Table 4.2. Properties of the BTO and BSO crystals

The distribution parameters for these centers as well as the values of k_U and E_U derived in the process of the theoretical curve fitting by the least-squares method are listed in Table 4.2. The main contribution to the absorption of these crystals in the “shoulder” region adjacent to the absorption band edge is made by the centers with the average ionization energies ~2.9 (for BTO) and ~2.75 eV (for BSO). It should be noted that the contribution of these centers to the absorption is by one order of magnitude higher for bismuth titanate compared to bismuth silicate. This point to the fact that the donor centers of this type may be associated with vacancies of Me (Ti in BTO or Si in BSO) as, according to the data given in [90], similar differences are exhibited for BTO and BSO crystals in the Me vacancy concentrations by neutron diffraction analysis.

4.7 Summary

In chapter 4 we have observed long-lived photo-induced absorption in the crystal BTO. The long-lived absorption is studied at the stage of the excitation and relaxation. Under normal conditions at room temperature and without pre-exposure the absorption is coursed only by the excitation of charges from deep levels (deep traps DT) and from the valence band (VB) to the conducting band (CB). The DT can be attributed to the spreading of the VB due to impurities and defects. The population of the DT is due e. g. to a stochastic excitation of charges from the VB and is much weaker than the population of the VB. The spectrum of the non-photo-induced absorption shows that the upper level of the DT lays at ca. 2.3 eV (ca. 540 nm) below the CB. The width of the forbidden band of the $Bi_{12}TiO_{20}$ crystal was measured and is approximately 3.1 eV (ca. 400 nm). After pre-exposure a growth of the photo-induced absorption k_{PI} is observed at wavelengths below 900 nm. The photo-induced absorption k_{PI} is connected with the excitation of charges from the long-lived intermediate traps (IT) to the CB. Traps are populated by charges due to the excitation of electrons from the DT and the VB to the CB and relaxation to the IT.

Due to the experimental observation of the induced absorption relaxation a two level (trap) model is suggested. The results are obtained with an approximation of the experimental dependences of the induced changes of absorption $k_{PI}(E,t)$ on the basis of relations, taking into account two centers that cause the average ionization energies $E_1 = 1.597 \pm 0.092$ eV and $E_2 = 2.566 \pm 0.028$ eV. The values of the half-widths of the distribution are $\Delta E_1 = 0.277 \pm 0.018$ eV and $\Delta E_2 = 0.580 \pm 0.031$ eV. The theoretically calculated values are compared with the experimentally detected in table 4.3 and stay in good agreement.

Experimental investigations approve the theoretical results On the base of the selected model and according to the experimental results one can estimate the dynamical characteristics of the energy levels (table 4.4).

It is shown that the pulse radiation is more effective for the stimulation of the long-lived absorption The relaxation of the photo-induced absorption can be slowed down and stopped using cw-radiation with low intensity from the blue-green wave range. In such a way it is possible to stop the relaxation at any stage. If one switches off the low cw-radiation, the relaxation process keeps going.

Crystal $Bi_{12}TiO_{20}$	Theoretically calculated	Experimentally measured
E_1^{IT}, eV	1.597	1.7
E_2^{IT}, eV	2.566	2.6
E^{DT}, eV	2.897	2.7
ΔE_1^{IT}, eV	0.277	0.4
ΔE_2^{IT}, eV	0.580	0.6
ΔE^{DT}, eV	0.326	0.4

Table 4.3. Comparison of the theoretical calculations and experimental measurements. E_i^j - ionization energy of the corresponding electron trap, ΔE_i^j - half-width of the corresponding electron trap

λ, nm	514	532
$\tau_{2a,1}$, s	$1.2\text{x}10^{4}$	$1\text{x}10^{4}$
$\tau_{2b,1}$, s	$5.5\text{x}10^{4}$	$7.5\text{x}10^{4}$
$\tau_{3,1} = \frac{1}{R_{3,1}}$, s	$\sim 6\text{x}10^{-8}$	$\sim 6\text{x}10^{-8}$
$\tau_{3,2} = \frac{1}{R_{3,2}}$, s	$\sim 12\text{x}10^{-8}$	$\sim 7\text{x}10^{-8}$

Table 4.4. Dynamical characteristics of the nominally pure $Bi_{12}TiO_{20}$. τ - lifetime of an energy level

If the BTO crystal with the photo-induced absorption is exposed by cw-radiation from the red wave range with low intensity the relaxation is faster. Compared with the previous results for the unstimulated relaxation red light accelerates the relaxation approximately by a factor of 10. On the other hand low intensity cw-radiation of the wavelengths 514 nm, 532 nm, and 633 nm didn't produce enough photo-induced absorption to be experimentally detected. Thus, one can use low intensity expositions at different wavelengths to control the photo-induced absorption.

The same method can be applied to other sillenite crystals. The spectral properties of the $Bi_{12}SiO_{20}$ (BSO) are analyzed successfully. The crystal $Bi_{12}SiO_{20}$ has the same structure of the two long-lived intermediate traps with a shift of the energy levels.

Chapter 5

Application of the photo-induced absorption

In chapter 4 we studied photo-induced properties of BTO (BSO) crystals as representatives of the sillenite group and investigated the high effective long-lived photo-induced absorption. Unstable absorption properties are on the way to the application of photorefractive crystals. In chapter 4.4 we discussed methods to control, reduce or stabilize the induced absorption. In this chapter we analyze possible applications of induced absorption.

Chapter 5.1 is devoted to the arising of the photorefractive sensibility for the red and IR spectral range due to long-lived induced absorption centers. In chapter 5.2 we analyze the possibility of information processing by controlling the long-lived absorption in BTO. The outlook for the application of induced absorption for the measurement of short pulses is discussed in chapter 5.3.

5.1 Analysis of the induced photorefractive sensitivity of BTO in the near IR

The increasing sensitivity of a BTO crystal for the recording of photorefractive holograms in the near IR region, as observed in [99, 104] under illumination of the crystal by VIS, is mainly due to the population of traps with an average energy E_1 = 1.60 eV by electrons. We express the photorefractive sensitivity in terms of the relation between the growth rate of the refractive index modulation amplitude Δn for the photorefractive grating at the initial stage of its formation and the intensity modulation amplitude mI_0 as follows

$$S_{ph} = \frac{1}{mI_0}\frac{d|\Delta n|}{dt}, \tag{5.1}$$

where m - contrast and I_0 - average light intensity of the interference pattern [14]. With the diffusion mechanism of the photorefractive grating formation [99, 104], the relations given in [14] make it possible to express the photorefractive sensitivity as follows

$$S_{ph}(\omega) = \frac{n^3 r_{eff} E_D}{2\left(1+K^2 L_D^2\right)}\frac{e\mu\tau_R}{\varepsilon}\frac{\phi(\omega)k(\omega)}{\hbar\omega}, \tag{5.2}$$

where n and r_{eff} - refractive index of the crystal and the effective Kerr constant, $E_D = K\left(k_B T/e\right)$ - diffusion field, $L_D = \left(\mu\tau_R k_B T/e\right)^{1/2}$ - diffusion length, μ and τ_R - mobility and recombination of a charge carrier, $K = 2\pi/\Lambda$, Λ - spatial grating period, k_B - Boltzmann constant, T - absolute time, ε - low frequency dielectric constant, e - elementary electric charge, and ϕ - quantum efficiency.

The dependence of the photorefractive effect on the wavelength described in (5.2) by the last factor is varying with the irradiation of the crystal due to changes in its optical absorption $k(\omega)$. At a wavelength of 780 nm, the experimental absorption factor of a BTO crystal not subjected to irradiation measured k = 0.14 cm^{-1}, being equal to 1.56 cm^{-1} for 1 hour of irradiation. As the wavelength is growing to 840 nm, the initial absorption decreases down to 0.02 cm^{-1}, coming to k = 0.76 cm^{-1} after the irradiation is terminated.

For the spectral region with $\lambda > 840$ nm the absorption of the BTO crystal is decreased as the wavelength is increasing. For the BTO crystal under study, the changes in the photorefractive sensitivity caused by an increase of optical absorption in the process of

irradiation, including the range of $\lambda > 840$ nm, may be estimated by the above-mentioned experimental results and theoretical model. In the region from 700 nm till 1100 nm, the dependence of the induced absorption on the wavelength calculated with the averaged model parameters and factors $b_{1,2}(t)$ at the relaxation times τ = 17 h and 34 h are shown in Fig. 5.1. It can be seen that the irradiation of the BTO crystal by nanosecond laser pulses (λ = 532 nm) may contribute significantly to its photorefractive sensitivity to IR radiation at wavelengths up to 1100 nm. However, the estimated absolute values of the photorefractive sensitivity for $\lambda = 1064$ nm are lower by decades compared to 780 nm.

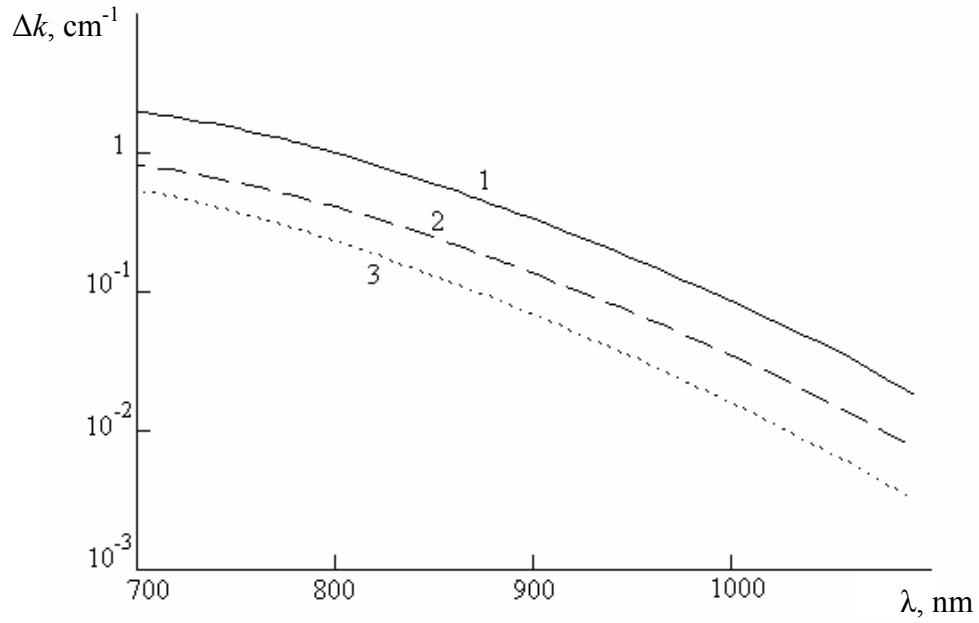

Fig. 5.1. Spectral dependence calculated for the induced absorption of a BTO crystal in the near IR immediately after irradiation (1), and after 17 h (2) and 34 h (3) dark relaxation. Absorption was induced with ns laser pulses (532 nm).

In this way, owing to irradiation of the BTO crystal by laser pulses at a wavelength of 532 nm, one can observe the changes of the optical absorption spectrum, which increases with the exposure. In the dark, the relaxation of the photo-induced changes of the absorption proceeds for more than 60 h. The spectral dependence of the additional absorption is adequately described with the model for the trapping of the photoexcited electrons by traps of two types with the normal energy distribution law for the concentrations at the average values of the ionization energy $E_1 \sim 1.6$ eV and $E_2 \sim 2.57$ eV.

On the base of the approximation methods for the spectral dependences of the induced absorption, one can estimate the dynamics of trap filling by electrons during the process of illumination by nanosecond laser pulses as well as the dynamics of trap depletion at the stage of dark relaxation. When the electrons populate the traps with the average energy $E_1 \sim 1.6$ eV the photorefractive sensitivity of the irradiated crystal in the near IR is increased, which depends on the magnitude of the induced absorption.

5.2 Processing of information

Using four light sources with different wavelengths one will be able to realize in future a system for information processing and storage. The location of electrons in the valence band, at the first or second long-lived energy level, is detected by changes of the absorption spectra. Due to the pulse laser radiation at 532 nm these levels are populated with electrons from the valence band during the pulse length of about 100 ns. Cw laser radiation at 514 nm or 532 nm enables one to maintain the redistribution of the electrons as long as necessary. The electrons are transferred back to the valence band by photoirradiation at 633 nm. A low-intensity probe beam with a visible-range wavelength can be used to control absorption and population of the levels. An electron is considered as a carrier of information. Its location in an energy system and space represents a bit of information. The distribution of electrons between the levels can be taken as a data register. Data processing can be realized by changes of the distribution of electrons. The usage of “UV-“green” radiation pulses offers a fast information recording in the bulk structure of the media, and the reverse operation is enabled by radiation of the “Red”-region. (Fig. 5.2)

It was shown in chapters 4.1.2 and 4.6 that the most effective wavelengths for the inducing of absorption in crystals of the sillenite group are in the UV-blue range (Fig. 4.4 p. 42) and in the green range for the pulse laser irradiation. Using short pulses one can work with two-photon absorption (Fig. 5.3). This gives the opportunity to write information with one ps or ns pulse.

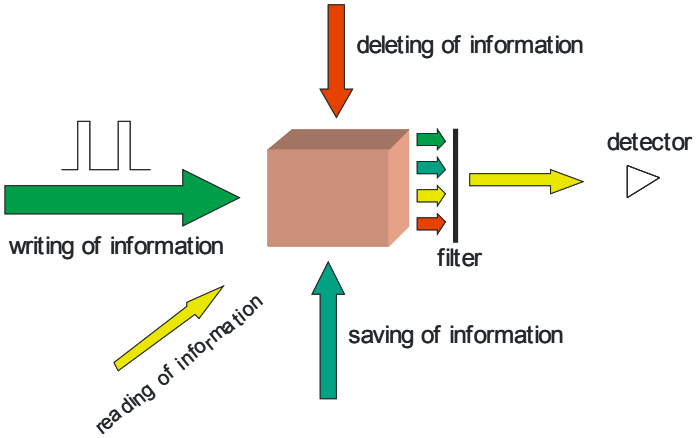

Fig. 5.2. On the base of the photochromic effect and methods of controlling of photo-induced absorption different kinds of switchers, optical logical and memory elements could be built.

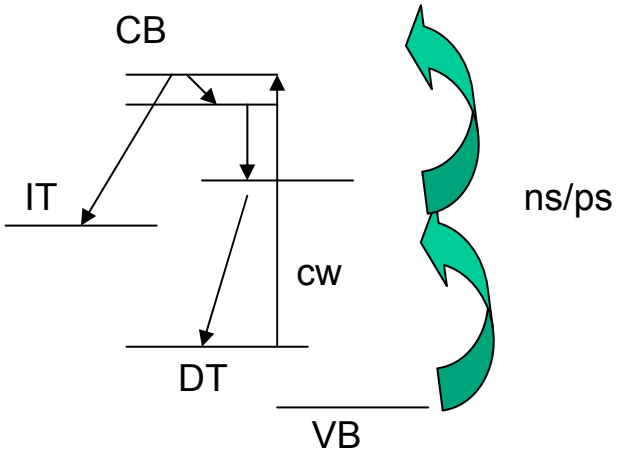

Fig. 5.3. Illustration of the multi-photon inducing of absorption centers.

Petrov et al. [14] showed that the diffusion length L_D in BTO crystals is 0.25 μm (0.29 μm for BGO). This is demonstrated in Fig. 5.4a.

Using the Bouguer law

$$I = I_0 e^{-kx} \tag{5.3}$$

one finds that the induced absorption can be already detected in crystals with a thickness of 50 μm. It is possible to realize data storage (Fig. 5.4b).

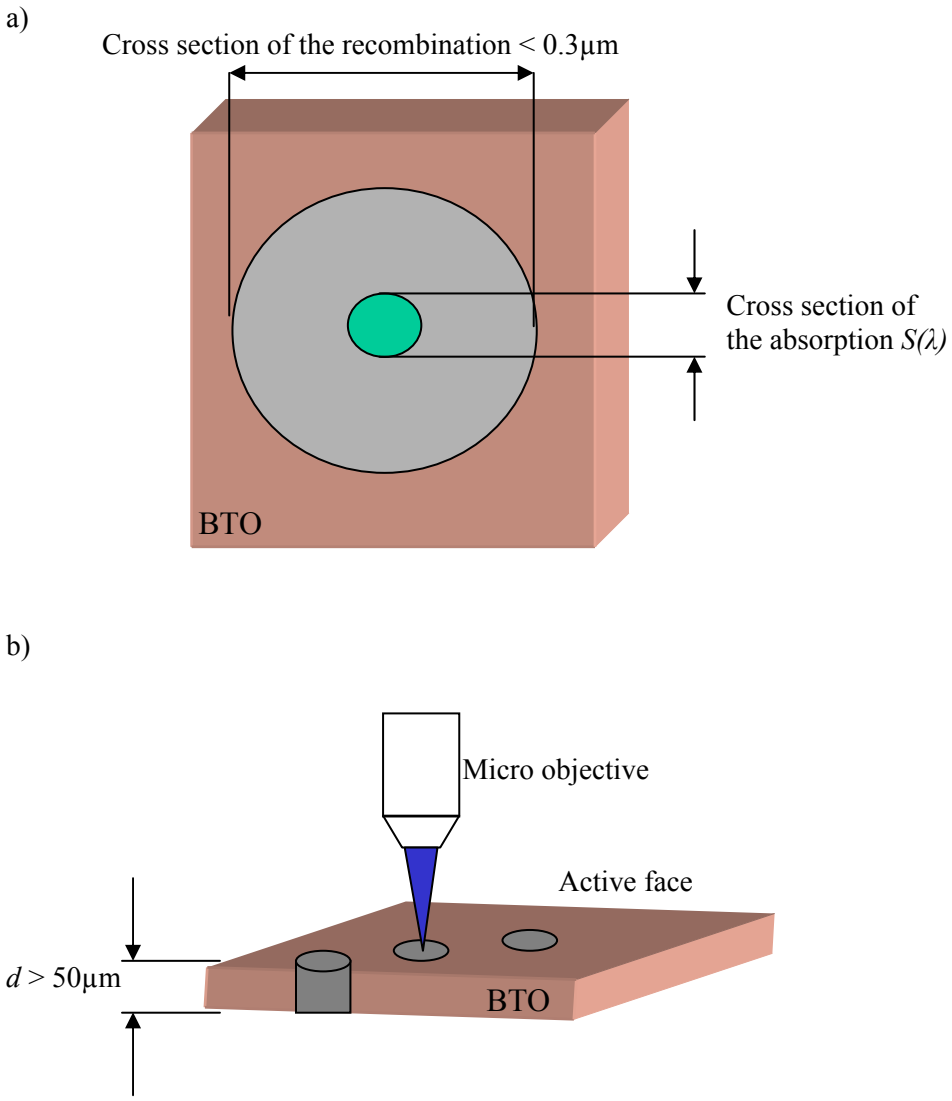

Fig. 5.4. a) Cross sections of the recombination and absorption during irradiation of the crystal, b) writing of the information on the active face of the crystal

5.3 Autocorrelator

The past decade has seen a tremendous progress in the development of lasers that emit ultrashort pulses. Light pulses are approaching durations of a single optical cycle: one to two femtoseconds for visible and near-IR wavelengths. And, in addition, the use of ultrashort pulses for both fundamental studies and applications is rapidly increasing. As these pulses shrink in length and grow in utility, the ability to measure them becomes very important.

The pulse is defined by its electric field *E(t)* as a function of time. For the sake of simplicity, we treat the field as linearly polarized and therefore consider only the scalar component of it. We also assume that the pulse separates into the product of spatial and temporal factors, and we neglect the spatial factor. The time-dependent component of the pulse can be written as

$$E(t) = \mathrm{Re}\{\sqrt{I(t)}\exp(i\omega_0 t - i\varphi(t))\}, \tag{5.5}$$

where *I(t)* and $\varphi(t)$ are the time-dependent intensity and phase of the pulse, and ω_0 is the carrier frequency. The time-dependent phase contains the frequency versus time information, and the pulse instantaneous frequency $\omega(t)$ is given by

$$\omega(t) = \omega_0 - \frac{d\varphi}{dt}. \tag{5.6}$$

Also the analytic signal in the single-side inverse Fourier transform of the field is

$$E(t) = \int_0^\infty d\omega \cdot \tilde{E}(\omega)\exp(-i\omega t), \tag{5.7}$$

where

$$\tilde{E}(\omega) = \int_{-\infty}^{+\infty} dt \cdot E(t)\exp(i\omega t). \tag{5.8}$$

It is complicated to measure ultrashort fs- and ps- pulses with typical semiconductor detectors. One uses autocorrelation methods to find the length of pulses. Specifically, an autocorrelator yields

$$A(\tau) = \int_{-\infty}^{+\infty} I(t)\cdot I(t-\tau)dt, \tag{5.9}$$

where τ is the relative delay between the pulses. Unfortunately, this measurement yields a smeared out version of *I*(*t*), and it often hides structure. For example, satellite pulses must be indirectly inferred from enlarged wings in *A(t)*.

Practically, one can use a two-photon process which takes place in a semiconductor detector excited at a wavelength below the band-gap cut off (Fig.5.6). Only a high peak power of laser pulses can give a two-photon signal which can be directly recorded on an oscilloscope as a function of the delay τ . Alternatively, a phase-matched doubling crystal, properly filtered to provide only the second-harmonic field, can extract the correct answer from the interferometer output. This harmonic field, recorded by a photodetector – a photomultiplier or a simple photodiode if the average signal is sufficient – as a function of the delay will give the same result.

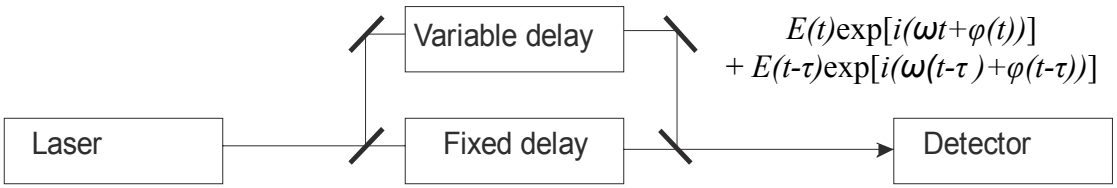

Fig. 5.6. Basic scheme of the autocorrelator

The main disadvantages of commonly used interferometric methods or the optical parametric generation are dependence on the wavelength and high frequency repetition rate.

Here, we propose a new autocorrelator concept based on the photo-induced absorption in BTO crystals which can be realized in future. Two pulse replicas without delay are mixed in the BTO crystal (Fig. 5.7a). Each pulse replica will be absorbed according to two photon processes. The modulation of the induced absorption is

$$k_{pi} \cong \left\{a^*(I) + b^*\right\} I \,, \tag{5.10}$$

where I – intensity, a^* – coefficient of the two-photon absorption, b^* – coefficient of one-photon absorption. As it was shown in chapter 4 one-photon absorption can be neglected. In the area of pulse mixing the induced absorption (Fig. 5.7b) is

$$k_{pi}(x) \cong \int_{-\infty}^{+\infty} a^*(I(x_0)) I(x_0) \cdot I(x_0 - x) \cdot dx_0 \,, \tag{5.11}$$

where x – coordinate of the axis of the light propagation. Equation (5.11) is the autocorrelation function of the short laser pulse (Fig. 5.7b). Detecting of the induced absorption with another probe beam and a linear photodetector array in transversal direction determines the correlation function (Fig. 5.7c).

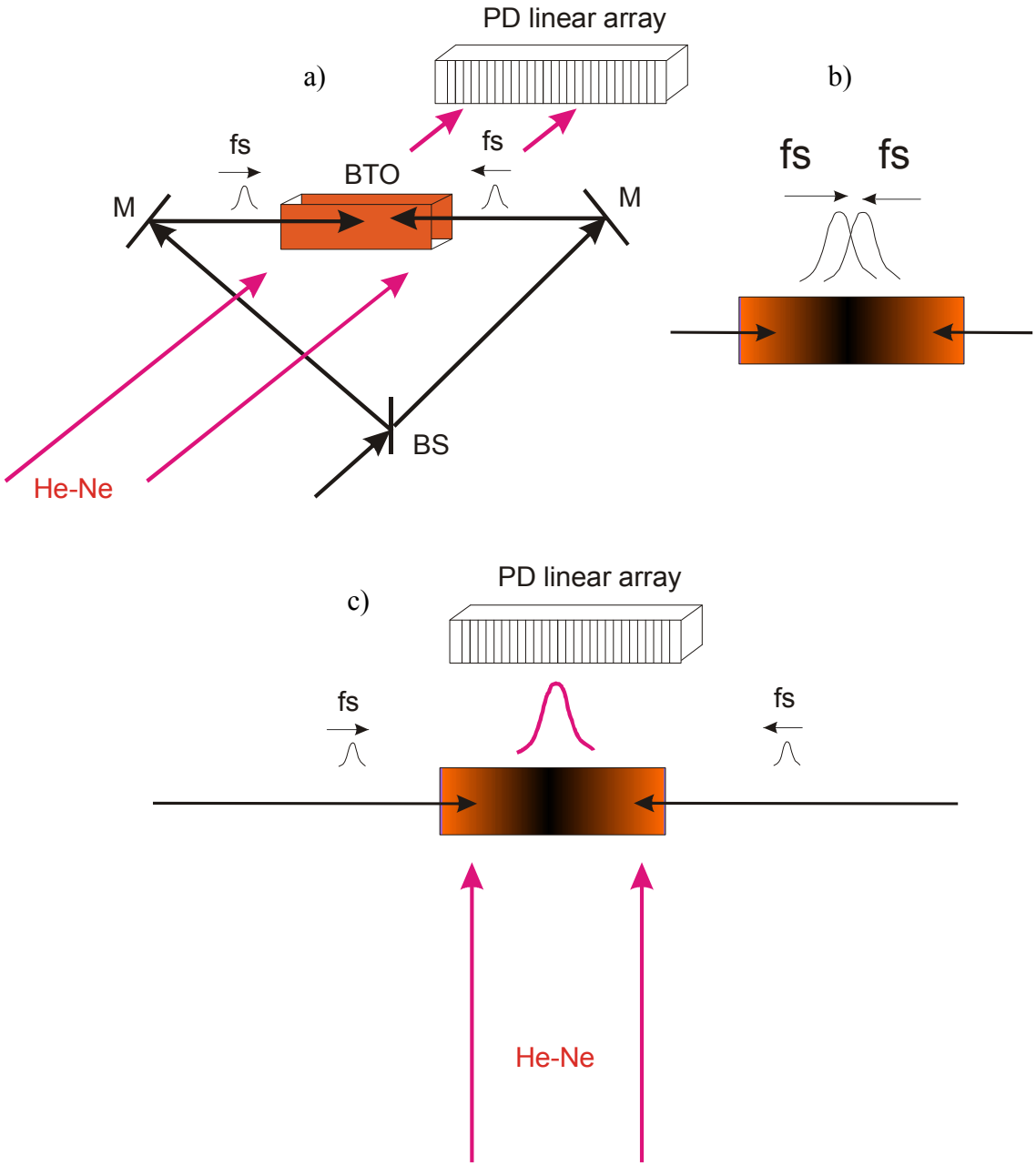

Fig. 5.7 a) basic scheme of the autocorrela tor on the base of the BTO crystal, b) two photon absorption in the crystal, c) detection of the induced absorption with another probe beam and a linear photodetector (PD)

Advantages of this method are the detection of the single-pulse characteristics and the insensibility to the wavelength. The forbidden band of the BTO is 3.1eV and the depth of the deep traps is 2.3 eV (chapter 4). The multi-photon processes are detectable due to induced absorption for wavelengths in the range of 500 nm-1100 nm. Using crystals in the form of the plane waveguides with a length till 10 cm one gets a detection range for pulses till 300 ps. The minimal length of pulses and the resolution of the system are limited only by the detector area.

Chapter 6

Summary

This work was devoted to long-lived photo-induced processes which are due to long-lived spectral changes of the photorefractive $Bi_{12}TiO_{20}$ crystal.

I. We study experimentally the spectral properties of the $Bi_{12}TiO_{20}$ crystal with and without induced long-lived absorption at room temperature. The long-lived photo-induced absorption is connected with the excitation of charges from the long-lived intermediate traps to the conducting band. Due to the experimental observation of the induced absorption under cw- and pulse laser radiation a model of two level (trap) relaxations is suggested. The investigation of the relaxation dynamics shows lifetimes of the long-lived levels of $1 \cdot 10^4$ s and $7 \cdot 10^4$ s. The experimental dependences show ionization energies of 1.6 eV and 2.8 eV of the levels. The values of the levels half-widths are 0.3 eV and 0.6 eV. These two intermediate levels are populated by charges due to excitation of electrons from the deep traps and the valence band to the conducting band and relaxation to the intermediate traps. The recombination times of electrons to the long-lived intermediate traps are 100 ns and 60 ns for the deep traps.

II. The investigation method can be applied to other sillenite crystals. Spectral properties of the $Bi_{12}SiO_{20}$ are analyzed and compared with $Bi_{12}TiO_{20}$. The crystal $Bi_{12}SiO_{20}$ has the same structure of the two long-lived intermediate levels. The ionization energies are 1.1 eV and 2.5 eV, with half-width 0.2 eV and 0.6 eV respectively. The energy level of the deep traps is 2.8 eV.

III. The changes of the electron redistribution in the defect centers and also the optical absorption caused by the recombination processes are nearly identical for picosecond, nanosecond and cw- irradiation. But the level of the initial crystal bleaching by a picosecond

pulse is by an order of magnitude higher than for nanosecond pulses with the same energy and by three orders higher than for cw-regime.

The long-lived induced absorption can be controlled by low cw-laser radiation ($100\mu W/mm^2$). The relaxation of the photo-induced absorption can be slowed down and stopped using cw-radiation from the blue-green wave range. If the crystal with the recently photo-induced absorption is exposed by a cw-radiation from the red wave range, the relaxation is accelerated. On the other hand low intensity cw-radiation of the wavelengths 514 nm, 532 nm, and 633 nm doesn't produce enough photo-induced absorption to be experimentally detected.

Photo-induced absorption influences on the photorefractive effect in crystals. When electrons populate the traps with the average energy 1.6 eV, the photorefractive sensitivity of the irradiated crystal in the near IR is increased, that may be estimated by the magnitude of the induced absorption.

IV. The photo-induced absorption can be used for information processing and storage based on four light sources with different wavelengths. Laser irradiation changes the electron distribution at the energy levels. The location of electrons in the valence band, at the first or second long-lived energy level, is detected by changes in the light absorption spectra. Due to the high-intensity green-blue pulse laser radiation these levels are populated. Low-intensity of green cw-laser radiation enables one to maintain the redistribution of the electrons as long as necessary. The electrons are transferred back to the valence band by red wave range light. The distribution of electrons between the levels can be taken as a data register.

We propose a new possible realization of an autocorrelator based on the photo-induced absorption in a BTO crystal. Two pulse replicas without delay are mixed in the BTO crystal. Each pulse replica will be absorbed according to two photon processes. The absorption is higher when the short laser pulses are overlapping. Detecting of the induced absorption with another probe beam and a linear photodetector array in transversal direction gives the correlation function. Advantages of this method are detection of the single pulse characteristics in the wide range 500-1100 nm.

In this work we have investigated experimentally and theoretically the long-lived photo-induced absorption in a $Bi_{12}TiO_{20}$ and $Bi_{12}SiO_{20}$ crystals. We characterize the internal system of the energy levels and its dynamic properties under room temperature, the pulse laser irradiation and show the bistable characteristics of the photo-induced absorption, to our knowledge for the first time.

As outlook for the future work the investigations of the multi-photon processes like two- and three- photon absorption are important. The sillenite crystals are promising media for transformation and control of high power pulse radiation generated by fs and ps lasers with high repetition. That's why it is important to get full information about the spectral and dynamical properties of the multi-photon processes in sillenite crystals. Also the investigation of the influence of the high power irradiation on the photorefractive and photochromic characteristics of the sillenite crystals and their possible applications will be continued.

ZUSAMMENFASSUNG

Diese Arbeit ist langlebigen photoinduzierten Prozessen gewidmet, die durch langlebige Spektralveränderungen des photorefraktiven $Bi_{12}TiO_{20}$ Kristalls bedingt sind.

I. Wir haben experimentell die Spektraleigenschaften von $Bi_{12}TiO_{20}$ Kristallen mit und ohne photoinduzierte langlebige Absorption bei Raumtemperatur untersucht. Die langlebige photoinduzierte Absorption ist mit der Anregung der Ladungen von Zwischenniveaus in das Leitungsband verbunden. Aufgrund der experimentellen Ergebnisse der photoinduzierten Absorption unter cw- und Pulslaserstrahlung wird ein Modell von Zweienergieniveaus vorgeschlagen. Die Untersuchung der Relaxationsdynamik zeigt Lebenszeiten der langlebigen Niveaus von $1 \cdot 10^4$ s und $7 \cdot 10^4$ s. Die experimentellen Abhängigkeiten zeigen Ionisationsenergien der Niveaus von 1,6 eV und 2,8 eV. Die Niveauhalbwertsbreiten betragen 0,3 eV und 0,6 eV. Diese zwei Zwischenniveaus werden wegen der Anregung von Elektronen von den tiefen Niveaus und dem Valenzband in das Leitungsband und der danach folgenden Relaxation in die Zwischenniveaus besiedelt. Die Rekombinationszeiten von Elektronen zu den langlebigen Zwischenniveaus betragen 100 ns und 60 ns für die tiefen Niveaus.

II. Die Untersuchungsmethode kann auf andere Sillenitkristalle angewandt werden. Die Spektraleigenschaften von $Bi_{12}SiO_{20}$ sind analysiert und mit $Bi_{12}TiO_{20}$ verglichen worden. Der Kristall $Bi_{12}TiO_{20}$ hat dieselbe Struktur der zwei langlebigen Zwischenniveaus. Die Ionisationsenergien sind 1,1 eV und 2,5 eV mit den entsprechenden Halbwertsbreiten von 0,2 eV und 0,6 eV. Die Energie des tiefen Niveaus ist 2,8 eV.

III. Die Veränderungen der Elektronenverteilung in den Defektzentren und auch der optischen Absorption, die durch Rekombinationsprozesse verursacht werden, sind fast identisch für ps-, ns- und cw-Strahlungen. Aber der Grad der anfänglichen Kristallbleiche für

ps-Pulse ist eine Größenordnung höher als für ns-Pulse mit derselben Energie und drei Ordnungen höher als für das cw-Regime.

Die langlebige photoinduzierte Absorption kann von der cw-Laserstrahlung mit niedriger Leistung (z. B. 100µW/mm^2) gesteuert werden. Die Relaxation der photoinduzierten Absorption wird mit einer cw-Strahlung mit einer Wellenlänge aus dem grün-blauen Bereich verlangsamt und angehalten. Wenn der Kristall mit der gerade photoinduzierten Absorption einer cw-Strahlung mit einer Wellenlänge aus dem roten Bereich ausgesetzt wird, wird die Relaxation beschleunigt. Andererseits erzeugt die cw-Strahlung niedriger Leistung der Wellenlängen 514 nm, 532 nm, und 633 nm nicht genug photoinduzierte Absorption, die experimentell messbar ist.

Die photoinduzierte Absorption beeinflusst den photorefraktiven Effekt in Sillenitkristallen. Wenn Elektronen die Niveaus mit der durchschnittlichen Energie 1,6 eV besiedeln, wird der photorefraktive Effekt im nahen IR-Bereich verstärkt. Das kann über die Modulation der photoinduzierten Absorption berechnet werden.

IV. Eine mögliche Anwendung der photoinduzierten Absorption für die Informationsspeicherung und -verarbeitung kann mit vier Lichtquellen verschiedener Wellenlängen realisiert werden. Die Laserstrahlung ändert die Elektronverteilung in den Energieniveaus. Die Position der Elektronen im Valenzband sowie im ersten oder zweiten langlebigen Energieniveau wird durch Änderungen in den Absorptionsspektren bestimmt. Wegen der hohen Intensität der grün-blauen Pulslaserstrahlung werden diese Niveaus besiedelt. Die niedrige Intensität grüner cw-Laserstrahlung ermöglicht es, die Neuverteilung der Elektronen so lange als notwendig aufrechtzuerhalten. Durch Beleuchtung aus dem roten Wellenlängenbereich gehen die Elektronen zurück in das Leitungsband. Die Verteilung von Elektronen zwischen den Niveaus kann als ein Datenregister genutzt werden.

Wir schlagen eine mögliche Realisierung einer Autokorrelation für kurze Laserpulse in einem Sillenitkristall vor, die auf der photoinduzierten Absorption basiert.

Zwei Laserpulszüge werden ohne Verzögerung im BTO Kristall gemischt. Jeder Pulszug wird gemäß der Zweiphotonenprozesse absorbiert. Die Absorption ist höher, wenn die kurzen Laserpulse überlappen. Die Messung der induzierten Absorption mit einem anderen Probestrahl und einem linearen Photodetektorarray in transversaler Richtung ergibt die Korrelationsfunktion. Der Vorteil dieser Methode wäre die Messung der charakteristischen Eigenschaften der Laserpulse im Wellenlängenbereich von 500 nm - 1100 nm.

In dieser Arbeit haben wir experimentell und theoretisch die langlebige photoinduzierte Absorption in $Bi_{12}TiO_{20}$ und $Bi_{12}SiO_{20}$ Kristallen untersucht. Wir charakterisierten das innere System der Energieniveaus und seine dynamischen Eigenschaften unter Raumtemperatur, Pulslaserstrahlung und zeigten die bistabilen Eigenschaften der photoinduzierten Absorption nach unserem Kenntnisstand zum ersten Mal.

Die zukünftige Arbeit sollte besonders den Mehrphotonenprozessen, wie der Zwei- und Dreiphotonenabsorption, gewidmet werden. Die Sillenitkristalle stellen ein gutes Medium für die Transformation und Kontrolle von Hochleistungspulslaserstrahlung dar, die durch fs - und ps - Laser mit hohen Wiederholungsraten erzeugt wird. Deshalb ist es wichtig, weitere Informationen über die spektralen und dynamischen Eigenschaften der Mehrphotonenprozesse in Sillenitkristallen zu gewinnen. Ebenso sollten Untersuchungen zum Einfluss hoher Bündelleistungen auf die photorefraktiven und photochromen Charakteristiken von Sillenitkristallen und ihren möglichen Anwendungen fortgesetzt werden.

References

[1] J. Feinberg, *Self-pumped, continuous-wave using internal reflection,* Opt. Lett., **7**, 486 (1982)

[2] V. Leyva, G. A. Rakuljic, B. O'Conner, *Narrow bandwidth volume holographic optical filter operating at the Kr transition at 1547.82 nm,* Appl. Phys. Lett., **65**, 1079 (1994)

[3] V. M. Petrov, C. Denz, A. V. Shmray, M. P. Petrov, T. Tschudi, *Electric field selectivity and multiplexing of volume holograms in $LiNbO_3$*, Appl. Phys. B, **71,** 43 (2000)

[4] C. Denz, T. Rausch, K.-O. Mueller, T. Heimann J. Trumpfheller, T. Tschudi, *Realization of a high-capacity holographic memory for analog and digital data storage based on phase-encoded multiplexing,* Technical Digest of the "Topical Meeting on photorefractive Materials, Effects and Devices", Waseda International Symposium, Tokyo, Japan, 232 (1997)

[5] M. Saffman, D. Z. Anderson, *Mode multiplexing and holographic demultiplexing communication channels on a multimode fiber,* Opt. Lett., **16**, 300 (1991)

[6] P. Yeh, *Introduction to photorefractive nonlinear optics,* John Wiley and Sons, Inc. (1993)

[7] K. Buse, *Light-induced charge transport processes in photorefractive crystals I: Models and experimental methods,* Appl. Phys. B, **64**, 273 (1997)

[8] J. Feinberg, D. Heiman, A. R. Tanguay, R. W. Hellwarth, *Photorefractive effects and light-induced charge migration in barium titanate,* J. Appl. Phys. **51(3)**, 1297 (1980)

[9] N. V. Kuchtarev, V. B. Markov, S. G. Odulov, M. S. Soskin, V. L, Vinetski, *Holographic storage in electrooptic crystals. I. Steady state,* Ferroel., **22**, 949 (1979)

[10] G. C. Valley, M. B. Klein, *Optical properties of photorefractive materials for optical data processing,* Opt. Engin. **22**, 705 (1983)

[11] F. P. Strohkendl, J. M. C. Jonathan, R. W. Hellwarth, *Hole-electron competition in photorefractive gratings,* Opt. Lett., **11**, 312 (1986)

[12] G. C. Valley, *Simultaneous electron/hole transport in photorefractive materials,* J. Appl. Phys., **5910**, 3363 (1986)

[13] M. C. Bashaw, T. P. Ma, R. C. Barker, S. Mroczkowski, *Theory of complementary holograms arising from electron-hole transport in photorefractive media,* JOSA B, **7,** 2329 (1990)

[14] M. P. Petrov, S. I. Stepanov, A. V. Khomenko, *Photorefractive crystals in coherent optical systems,* Springer-Verlag (1990)

[15] V. Prokofiev, *Photorefractive crystals and fibers for optical information processing,* University of Joensuu, Department of Physics, Väisälä Laboratory, Dissertation 11, 53 (1996)

[16] K. V. Yumashev, P. V. Prokoshin, A. M. Malyarevich, and V. P. Mikhailov, *Transient bleaching/induced absorption in reduced $SrTiO_3$ under picosecond excitation,* J. Opt. Soc. Am. B, **14**, 415 (1997)

[17] N. A. Vainos, S.L. Clapharm, R. W. Eason, *Multiplexed permanent and real time holographic recording in photorefractive BSO,* Appl. Opt., **28**, 4381, (1989)

[18] A. Kamshilin, *Simultaneous recording of absorption and photorefractive gratings in photorefractive crystals,* Opt. Comm., **93**, 350 (1992)

[19] J.J Martin, I. Foldvari, C.A. Hunt, *The low-temperature photochromic response of bismuth germanium oxide,* J. Appl. Phys., **70 (**12**)**, 7554 (1991)

[20] D.W. Hart, C.A. Hunt, D.D. Hunt, J.J Martin, Meckie T. Harris, John J. Larkin, *The low-temperature photochromic response of bismuth silicon oxide,* J. Appl. Phys., **73** (3), 1443 (1993)

[21] O. Kobozev, S. Shandarov, A. Kamshilin, V. Prokofiev, *Light-induced absorption in a $Bi_{12}TiO_{20}$ crystal,* J.Opt. A: Pure Appl. Opt., **1**, 442 (1999)

[22] V. Marinova, S. H. Lin, V. Sainov, M. Gospodinov, K. Y. Hsu, *Light-induced properties of Ru-doped $Bi_{12}TiO_{20}$ crystals,* J. Opt. A: Pure Appl. Opt., **5**. S500 (2003)

[23] S. M. Shandarov, A. E. Mandel', A. V. Kazarin, A. M. Plesovskikh, Yu. F. Kargin, V. V. Volkov, A. V. Egorysheva, *Dynamics of the Light-Induced Absorption in a $Bi_{12}TiO_{20}$: Ca Crystal,* Russian Physics Journal., **45**, 763 (2002)

[24] A. N. Dubrovin, A. E. Mandel', S. M. Shandarov, M. A .Zhnykina, Yu. M. Sukhoverkhov, Yu. F. Kargin, V. V. Volkov, A. V. Egorysheva, V. V. Shepelevich, *Temperature-dependent optical absorption and its photoinduced changes in $Bi_{12}TiO_{20}$〈Ca〉 crystals,* Inorganic Materials, **40**, 1280 (2004)

[25] Yu. F. Kargin, A. V. Egorysheva, V. V. Volkov, M. N. Frolova, M. V. Borodin, S. M. Shandarov, V. M. Shandarov, D. Kip, *The growth of photorefractive planar BTO/BSO and BTO/BGO waveguide,* Journal of Crystal Growth **275**, e2403 (2005)

[26] J. S. McCullough, A. Harmon, J.J Martin, M.T. Harris, J.J. Larkin, *Low-temperature photochromic response of phosphorus-doped bismuth silicon oxide,* J. Appl. Phys., **78** (3), 2010 (1995)

[27] J. S. McCullough, A. M. Georgalas, C.A. Hunt, Susan P. Hoefler-Coster, D.W. Peakheart, G.S. Dixon, J.J. Martin, *Kinetics of the photorefractive response of bismuth silicon oxide,* J. Appl. Phys. **89** (10), 5276 (2001)

[28] J. S. McCullough, A.L. Harmon Bauer, C.A. Hunt, J.J Martin, *Photochromic response of bismuth germanium oxide doped with chromium,* J. Appl. Phys. **90** (12), 6017 (2001)

[29] Adam W. Wood, C.A. Hunt, J.J Martin, *The low-temperature photochromic and photorefractive response of bismuth germanium oxide doped with molybdenum,* J. Appl. Phys. **101**, 063517 (2007)

[30] A. Harmi, M. Secu, V. Topa, B. Briat, *Influence of initial conditions on the optical and electrical characterisation of sillenite-type crystals,* Optical materials, **4**, 197 (1995)

[31] B. Briat, T. V. Panchenko, H. Bou Rjeily, A. Hamri, *Optical and magneto-optical characterization of the Al acceptor levels in $Bi_{12}SiO_{20}$,* J. Opt. Soc. Am. B. **15**, 2147 (1998)

[32] F. Ramaz, L. Rakitina, M. Gospodinov, B. Briat, *Photorefractive and photochromic properties of ruthenium-doped $Bi_{12}SiO_{20}$,* Optical materials, **27**, 1547 (2005)

[33] T. V. Pavchenko, *Thermooptical investigation of deep levels in doped Bi12SiO20 crystals,* Physics of the Solid State, **40**, 3, 415 (1998)

[34] G. Cedilnik, M. Esselbach, A. Kiessling, R. Kowarschik, E. Nippolainen, A. A. Kamshilin, V. V. Prokofiev, *Photorefractive effects in long, narrow BSO crystals with applied electric field,* Appl. Phys. B, **68**, 983 (1999)

[35] A. I. Grachev, *Monopolarity of extrinsic photoconduction in sillenite-type crystals,* Phys. Sol. Stat., **40**, 1975 (1998)

[36] A. I. Grachev, *Holographic recording in photorefractive crystals with nonstationary and nonlinear photoconductivity,* Phys. Sol. Stat., **41**, 922 (1999)

[37] P. Tayebati, D. Mahgereftech, *Theory of the photorefractive effect for $Bi_{12}SiO_{20}$ and $BaTiO_3$ with shallow traps,* JOSA B, **8**, 1053 (1991)

[38] G. A. Brost, R. A. Motes, J. R. Rotge, *Intensity-dependent absorption and photorefractive effects in barium titanate,* JOSA B, **5**, 1879 (1988)

[39] S. M. Shandarov, O. V. Kobozev, A. V. Reshet'ko, M. G. Krause, V. V. Volkov, Yu. F. Kargin, *Photorefractive response in sillenite crystals with shallows traps by applying an alternative electric field,* Ferroel., **202**, 257 (1997)

[40] R. S. Cudney, R. M. Pierce, D. G. Bacher, J. Feinberg, *Absorption grating in photorefractive crystals with multiple levels,* JOSA B, **8**, 1326 (1991)

[41] O. V. Kobozev, S. M. Shandarov, A. A. Kamshilin, V. V. Prokofiev, *Light-induced absorption in a $Bi_{12}TiO_{20}$ crystals,* J. Opt. A.: Pure Appl. Opt., **1**, 442 (1999)

[42] A. N. Pikhtin, *Optical and Quantum Electronics,* Handbook for Higher Institutes, Moscow: Higher School, 573 (2001)

[43] A. Tolstik, A. Matusevich, M. Kisteneva, S. Shandarov, S. Itkin, A. Mandel, Yu. Kargin, Yu. Kylchin, R. Romashko, *Spectral dependence of absorption photoinduced in a $Bi_{12}TiO_{20}$ crystal by 532-nm laser pulses,* Quantum electronics, **37**, 1027 (2007)

[44] V. Matusevich, A. Kiessling, R. Kowarschik, *Model of deep and shallow traps for the crystal $Ba_{0.77}Ca_{0.23}TiO_3$,* Appl. Phys. B, **72**, 435 (2001)

[45] K. Buse, *Light-induced charge transport processes in photorefractive crystals I: Models and experimental methods,* Appl. Phys. B, **64**, 273 (1997)

[46] D. Fluck, P. Amrhein, P. Guenter, *Photorefractive effect in crystal with a nonlinear recombination of charge carriers: theory and observation,* JOSA B, **8**, 2196 (1991)

[47] G. C. Valley, *Erase rates in photorefractive materials with two photoactive species,* Appl. Opt., **22**, 3160 (1983)

[48] G. Lesaux, G. Roosen, A. Brun, *Observation and analysis of the fast photorefractive processes in BSO,* Opt. Commun., **56**, 374 (1986)

[49] V. Matusevich, A. Kiessling, R. Kowarschik, *Experimental determination of the electro-optic coefficients in $Ba_{0.77}Ca_{0.23}TiO_3$,* Appl. Phys. B, **71**, 533 (2000)

[50] M. H. Garrett, J. Y. Chang, H. P. Jenssen, C. Warde, *High beam-coupling gain and deep- and shallow-trap effects in cobalt-doped barium titanate, $BaTiO_3$:Co,* JOSA B, **9**, 1407 (1992)

[51] M. B. Klein, G. C. Valley, *Beam coupling in $BaTiO_3$ at 442nm,* J. Appl. Phys., **57(11)**, 4901 (1985)

[52] R. A. Rupp, A. Maillard, J. Walter, *Impact of the sublinear photoconductivity law on the interpretation of holographic results in $BaTiO_3$,* Appl. Phys. A, **49**, 259 (1989)

[53] I. Biaggio, M. Zgodnik, P. Guenter, *Build-up and dark decay of transient photorefractive gratings in reduced $KNbO_3$,* Opt. Commun. **77**, 312 (1990)

[54] P. Tayebati, *Effect of shallow traps on electro-hole competition in semi-insulating photorefractive materials,* JOSA B, **9**, 415 (1992)

[55] P. Guenter, J.-P. Huingard, *Photorefractive materials and their applications I,* Topics in Applied Physics, Springer-Verlag, **61**, (1988)

[56] L.G.Sillen, *X-ray studies of bismuth trioxide,* Arkiv för Kemi, Miner.och Geol. **12A**, 1 (1937)

[57] B. Aurivillius and L. G. Sillen, *Polymophy of bismuth trioxide,* Nature **155**, 305 (1945)

[58] E. M. Levin and R. S. Roth, *Polymorphism of bismuth sesquioxide, II. Effect of oxide addition on the polymorphism of Bi_2O_3,* J.Res.Nat.Bur.Stand. **68A**, 197 (1964)

[59] S. C. Abrahams, P. B. Jamieson and J. L. Bernstein, *Crystal structure of piezoelectric bismuth germanium oxide $Bi_{12}GeO_{20}$,* J. Chem. Phys. **47**, 4034 (1967)

[60] D. C. Craig and N. C. Stephenson, *Structural studies of some body-centered cubic phases of mixed oxides involving Bi_2O_3: The structures of $Bi_{25}FeO_{40}$ and $Bi_{38}znO_{60}$,* J. solid State Chem. **15**, 1 (1975)

[61] S. F. Radaev, L. A. Muradyan, V. I. Simonov, *Atomic structure and crystal chemistry of sillenites: $Bi_{12}(Bi^{3+}_{0.50}Fe^{3+}_{0.50})O_{19.50}$ and $Bi_{12}(Bi^{3+}_{0.67}Zn^{3+}_{0.33})O_{19.33}$,* Acta Cryst. **B47,** 1 (1991)

[62] S. C. Abrahams, J. L. Bernstein, C. Svensson, C*rystalstructure ans absolute piezoelectric d_{14} coefficient in laevorotatory $Bi_{12}SiO_{20}$,* J. Chem. Phys. **71**, 788 (1979)

[63] H.-J. Reyher, U. Hellwig and O. Thiemann, *Optically detected magnetic resonance of the bismuth-on-metal-site intrinsic defect in photorefractive sillenite crystals,* Phys. Rev. B, **47**, 5638 (1993)

[64] M. Devalette, G. Meunier, C. Mazeau, A. Morell, P. Hagenmuller, *Determination de la taille du bismuth pentavalent en site tetraedrique dans les phases de type sillenite,* C. R. Acad. Sc., Ser. C, **291** 251 (1980)

[65] M. Devalette, J. Darriet, M. Couzi, C. Mazeau, P. Hagenmuller, *Characterization de l'environnement tetraedrique des cations A et B dans les phases $Bi_{12}(A^{III}_{1/2}B^{V}_{1/2})O_{20}$ de structure sillenite,* J. Solid State Chem. **43**, 45 (1982)

[66] M. Devalette, N. Khachani, G. Meunier, P. Hagenmuller, *Simulated behavior of bismuth oxide in the formation of some $Bi_{12}[A_\alpha{}^{+III}B_\beta{}^{+V}]O_{20}$,* Mater. Lett. **2**, 318 (1984)

[67] S. F. Radaev, L. A. Muradyan, Yu. F. Kargin, V. A. Sarin, E. E. Rider, V. I. Simonov, *Atomic structure of $Bi_{25}GaO_{39}$ and interpretation of the structure of sillenite-type crystal,* Sov. Phys. Dokl. (USA), **34**, 407 (1989)

[68] S. F. Radaev, M. Trömel, Yu. F. Kargin, A. A. Marin, E. E. Rider, V. A. Sarin, $Bi_{12}(Bi_{0.5}^{III}Ti_{0.5}^{III})O_{19.50}$, Acta Cryst. **C50**, 656 (1994)

[69] D. C. .N. Swindells, J. L. Gonzales, *Absolute configuration and optical activity of laevorotatory $Bi_{12}TiO_{20}$*, Acta Cryst. **B44**, 12 (1988)

[70] A. A. Ballman, *The growth and properties of piezoelectric bismuth germanium oxide $Bi_{12}GeO_{20}$,* J. Cryst. Growth, **1**, 37 (1967)

[71] B. C. Grabmaier, *Single crystal growth from γ-bismuth trioxide by the Gzochralski method,* Second National Confer. on Crystal Growth, Freiburg in Bresgau, 21-23 Sept., Book of abstracts, 11(1972)

[72] J. C. Brice, T. M. Bruton, O. F. Hill, P. A. C. Whiffin, *The Czochralski growth of $Bi_{12}SiO_{20}$ crystals,* J. Cryst. Growth, **24/25**, 429 (1974)

[73] A. R. Tanguay, Jr. S. Mroczkowski, R. C. Barker, *The Czochralski growth of optical quality bismuth silicon oxide ($Bi_{12}SiO_{20}$),* J. Cryst. Growth, **42**, 431 (1977)

[74] J. C. Brice, M. J. Hight, O. F. Hill, P. A. C. Whiffin, *Pulling large bismuth-silicon-oxide crystals,* Philips Tech. Rev. **37**, 250 (1977)

[75] W. Piekarczyk, M. Swirkowicz, S. Gazda, *The Czochralski growth of bismuth-germanium oxide single crystals,* Mater. Res. Bull. **13**, 889 (1978)

[76] J. Martinez-Lopez, M. A. Caballero, M. T. Santos, L. Arizmendi, E. Diegues, *Solid-liquid interface in the growth of sillenite-type crystals,* J. Cryst. Growth, **128,** 852 (1993)

[77] M. H. Garrett, *Properties of photorefractive nonstoichiometric bismuth silicon oxide, $Bi_xSiO_{1.5x+2}$,* J. Opt. Soc. Am. **8B**, 78 (1991)

[78] S. L. Hou, R. B. Lauer, R. E. Aldrich, *Transport processes of photoinduced carriers in $Bi_{12}SiO_{20}$,* J. Appl. Phys., **44**, 2652 (1973)

[79] L. Arizmendi, J. M. Cabrera, F. Agullo-Lopez, M*aterial properties and photorefractive behaviour of BSO family crystals,* Inter. J. Optoelectron., **7**, 149 (1992)

[80] R. A. Mullen, *Photorefractive measurements of physical parameters,* Chap.6 in *Photorefractive Materials and Their Applications I,* R. Günter, J. P. Huignard, (Eds.), Springer Verlag, Berlin, 167 (1988)

[81] G. C. Valley, M. B. Klein, *Optimal properties of photorefractive materials for optical data processing,* Opt. Engin. **22**, 704 (1983)

[82] M. Petlier, F. Micheron, *Volume hologram recording and charge transfer process in $Bi_{12}SiO_{20}$ and $Bi_{12}GeO_{20}$*, J. Appl. Phys. **48**, 3683 (1977)

[83] S. I. Stepanov, M. P. Petrov, *Nonstationary holographic recordering for efficient amplification and phase conjugation,* Chap.9 in *Photorefractive Materials and Their Applications I,* R. Günter, J. P. Huignard, (Eds.), Springer Verlag, Berlin, 263 (1988)

[84] V. K. Malinovskij, O. A. Gudaev, V. A. Gusev, S. I. Demenko, *Photoinduced phenomena in sillenite,* Nauka, Novosibirsk, 160 (1990)

[85] Yu. F. Kargin, V. I. Burkov, A. A. Mar'in, A. V. Egorisheva, *Crystals $Bi_{12}M_xO_{20-\delta}$ with sillenite structure. Synthesis, structure, properties,* Institute of the General and Nonorganic Chemistry, Russian Academy of Sciences, 304 (2004)

[86] V. A. Gusev, V. A. Detinenko, A. P. Sokolov, Autometrie, **5**, 34 (1983)

[87] J. J. Martin, I. Foldvari, C. A. Hunt, *The low-temperature photochromic response of bismuth germanium oxide,* J. Appl. Phys., **70**, 7554 (1991)

[88] A. V. Egorisheva, V. V. Volkov, V. M. Skorikov, Inorganic Materials, **30,** 653 (1994)

[89] T. V. Panchenko, *Photo- and thermo- induced optical absorption and photoconductivity of the sillenite crystals,* Solid State Physics, **42**, 641 (2000)

[90] V. I. Burkov, A. V. Egorisheva, Yu. F. Kargin, Crystallography Reports, **46,** 356 (2001)

[91] S. Rieheman, F. Rickermann, V. V. Volkov, A. V. Egorysheva, G. Von Bally, *Optical and Photorefractive Characterization of BTO Crystals Doped with Cd, Ca, Ga, and V,* J. Non. Opt. Phys. And Mater., **6**, 235 (1997)

[92] A. E. Mandel', S. M. Shandarov, A. V. Kazarin, Yu. F. Kargin, A. M. Plesovskih, V. V. Volkov, A. V. Egorisheva, *Dynamic of the photo-induced light absorption in the crystal $Bi_{12}TiO_{20}$,* Proceedings of the Institutes of the Higher Education, Physics **2**, 29 (2002)

[93] A. G. Mart'yanov, E. Yu. Ageev, S. M. Shandarov, A. E. Mandel', N. V. Bochanova, N. V. Ivanova, Yu. F. Kargin, V. V. Volkov, A. V. Egorysheva, V. V. Shepelevich, *Interaction of two counterpropagating waves in a Ca:Ga:$Bi_{12}TiO_{20}$ crystal upon photoinduced absorption of light,* Quantum Electron., **33**, 226 (2003)

[94] G. A. Brost, R. A. Motes, and J. R. Rotge, *Intensity-dependent absorption and photorefractive effects in barium titanate,* J. Opt. Soc. Am. B, **5**, 1879 (1988)

[95] A. Motes, G. Brost, J. Rotge, and J. J. Kim, Temporal behavior of the intensity-dependent absorption in photorefractive $BaTiO_3$, Opt. Lett., **13**, 509 (1988)

[96] A.L. Tolstik. N.G. Borzdov. A.Y. Matusevich. E.A. Melnikova. A.P. Sukhorukov, Multiwave mixing and soliton-like spatial structures in photorefractive crystals, Nonlinear Optics Applications, Proc. of SPIE, v.5949, 334 (2005)

[97] A. E. Mandel', S. M. Shandarov, A. M. Plesovskih, et al, ,Proceedings of the Institutes of the Higher Education, Physics, **12**, 48 (2003)

[98] G. A. Brost, R. A. Motes, and J. R. Rotge, *Intensity-dependent absorption and photorefractive effects in barium titanate,* J. Opt. Soc. Am. B, **5**, 1879 (1988)

[99] S.G. Odoulov, K.V. Shcherbin, A.N. Shumeljuk, *Photorefractive recording in BTO in the near infrared,* J. Opt. Soc. Am. B, **11**, 1780 (1994)

[100] I. Nee, M. Müller, K. Buse, E. Krätzig, *Role of iron in lithium-niobate crystals for the dark-storage time of holograms ,* J. Appl. Phys., **88**, 4282 (2000)

[101] A. Matusevich, A. Tolstik, M. Kisteneva, S. Shandarov, V. Matusevich, A. Kiessling, R. Kowarschik, *Investigation of photo-induced absorption in a $Bi_{12}TiO_{20}$ crystal,* Appl. Phys. B, **92**, 219 (2008)

[102] O. Beyer, D. Maxein, K. Buse, B. Sturman, H. T. Hsieh, D. Psaltis, *Femtosecond time-resolved absorption processes in lithium niobate crystals* , Opt. Lett. **30**, 1366 (2005)

[103] Yu. I. Uhanov, *Optical properties of the semiconductors,* Moscau, Nauka, 366, (1977)

[104] P. V. Dos Santos, J. Frejlich, J. F. Carvalho *Direct near infrared photorefractive recording and pre-exposure controlled hole–electron competition with enhanced recording in undoped $Bi_{12}TiO_{20}$,* Appl. Phys. B, **81**, 651 (2005)

Abbreviations and Variables

$A(x,y)$	Amplitude of the the electric field in the electro-magnetic wave
a^*	coefficient of the two-photon absorption
a_{therm}	thermal conductivity coefficient
b^*	coefficient of one-photon absorption
BGO	$Bi_{12}GeO_{20}$
BSO	$Bi_{12}SiO_{20}$
BTO	$Bi_{12}TiO_{20}$
CB	conducting band
D^-	filed trap
d	sample thickness
D^0	excited trap
D_i	trap of *i* type located in forbidden band
DT	deep trap
e	elementary charge
$\bar{e}_S$	unit vector for spontaneous polarization
$E_a^{\ i}$	energy of the thermal activation of the donor *i*
E_c	energy edge of the conducting band
E_D	donor's energy level
E_{diff}	diffusion field
E_F	equals the distance of the Fermi level to the conducting band
E_G	photovoltaic electrical field
E_I	energy if the ionization
E_j, E_k	components of an electromagnetic light wave
E_o	external electrical field

E_{phv}	bulk photovoltaic field
E_{pyro}	pyroelectric field
E_{sc}	space charge field
E_U	characteristic energy conforming to the Uhrbach rule
E_v	energy edge of the valence band
Λ	grating period
$\hbar$	Planck constant
I	light intensity
I_0	background intensity
IM	intermediate trap
I_p	energy of laser pulse
$\vec{j}_{diff}$	diffusion current
$\vec{j}_{drift}$	drift current
$\vec{j}_{ph}$.	photovoltaic current
k	light absorption coefficient
K	vector magnitude of grating
$K(E)$	"level density"
k_0	coefficient of absorption without the photo-induced effect
k_1, k_2	initial coefficients of absorption for long-lived levels *1* and *2*
k_B	Boltzmann constant
k_{PI}	photo-induced absorption
Lb_i	laser beam *i* at the scheme
L_D	free path
m	intensity modulation depth
n	refractive index
$N(E)$	density of the absorption centers
N_A	number density of acceptors
n_b	background refractive index
N_D	number density of dopants
N_D^+	number density of ionized dopants
N_e	electron concentration
n_e	refractive index of the extraordinary ray

$N_e(x)$	concentration of free carriers
N_h	density of holes within the conduction and valence bands
N_i	concentrations of the charge carriers at the level i (i = 1, 2a, 2b, 3)
n_i	population of the level i
N_i^+	concentrations of the ionized centers at the level i (i = 1, 2a, 2b, 3)
$N_n(E)$	distribution law for the concentration of the n-type traps
n_o	refractive index of the ordinary ray
P_S	spontaneous polarization
q_M	occupancy factor of the M cations
R	Fresnel coefficient for reflection from the crystal edge
R	recombination degree
r_{eff}	effective electro-optic coefficient
$r_{i,j}$	recombination coefficients from the upper level i to the lower j
$R_{i,j}$	relaxation constants from level i to level j
r_{ijk}	electrooptic coefficients
R_{OC}	attenuation factor
$\hat{r}$	tensor matrix of the electro-optic coefficients
s	cross-section for phohotoionization
$S(E)$	cross section of the absorption for centers localized at the depth E
S_i	cross sections of the absorption for level i (i = 1, 2a, 2b, 3)
s_{ijkm}	quadratic electro-optic coefficients
S_{ph}	photorefractive sensitivity
T	temperature
T_{therm}	characteristic time of the thermal grating formation
t_{ex}	exposure time
ΔT	temperature variations in the medium subjected
$U_{\lambda/2}$	half-wave voltage
VB	valence band
x, y, z	coordinate system
α	constant factor characterizing the crystal and doping elements
β	coefficient of the thermal excitation
β_{ijk}	photovoltaic coefficients
$\beta_{i,j}$	constants defining inner transitions coefficients between levels

γ_R	coefficient for electron recombination
Δn	refractive index modulation amplitude
ε	low frequency dielectric constant
μ	charge mobility
μ_e	mobility of electrons
μ_h	mobility of holes
η_{hol}	diffraction efficiency
η_{ij}	the impermeability tensor
λ	wavelength
ρ_0	average value of the positive charge density
σ	photoconductivity
σ_e	electron conductivity
σ_h	hole conductivity
$\theta(t)$	step Heaviside function
θ	angle between laser beams
τ	lifetime
τ_1, τ_2	times of life of long-lived levels *1* and *2*
τ_p	pulse length
τ_{therm}	relaxation (erasure) time for the thermal nonlinearity grating
υ_{sound}	speed of sound propagation in this medium
Φ	quantum efficiency
$\varphi(t)$	time-dependent phase
ϖ	bulk photovoltaic coefficient
$\omega(t)$	time-dependent frequency